UNIVERSITY OF COSTA RICA

MASTER THESIS

Estimation of Primary and Scatter Signal Profiles in Computer Tomography using Geant4

Author:
Daniel ARROYO-PORTILLA

Supervisor:
PhD. Mariela A. PORRAS-CHAVERRI
Readers:
PhD. Bruce WHITING
PhD. Mario CUBERO

A thesis submitted in fulfillment of the requirements
for the degree of Master Degree

in the

Physics Postgraduate Program
Postgraduate Study System

June 11, 2024


UNIVERSIDAD DE COSTA RICA
LUCEM ASPICIO
UNIVERSIDAD DE
COSTA RICA

Acknowledgements

I would like to thank the following people for making this research project possible:

- To my parents, Anay Portilla Acuña and Francisco Arroyo Mora, for always supporting me in every aspect of my life. Without their help, this project wouldn't be possible.
- To my supervisor Mariela Porras Chaverri, who helped me in every step of this project and guided me in the correct steps.
- To Mario Cubero, reader of my thesis and for developing the first guide on the toolkit installation.
- To Bruce Whiting, reader of my thesis and whose wide experience and understanding in CT systems was greatly appreciated.
- To Jeff Williamson, whose advice and extensive knowledge on this topic helped me in the development of the algorithms and data analysis.
- To Joseph O'Sullivan, whose consideration in the research group became a great exchange of ideas and a wonderful experience.

Approval Page

This thesis was accepted by the postgraduate physics commission program from the University of Costa Rica, as a partial requirement to opt for the grade and degree of Academic Master in Medical Physics.

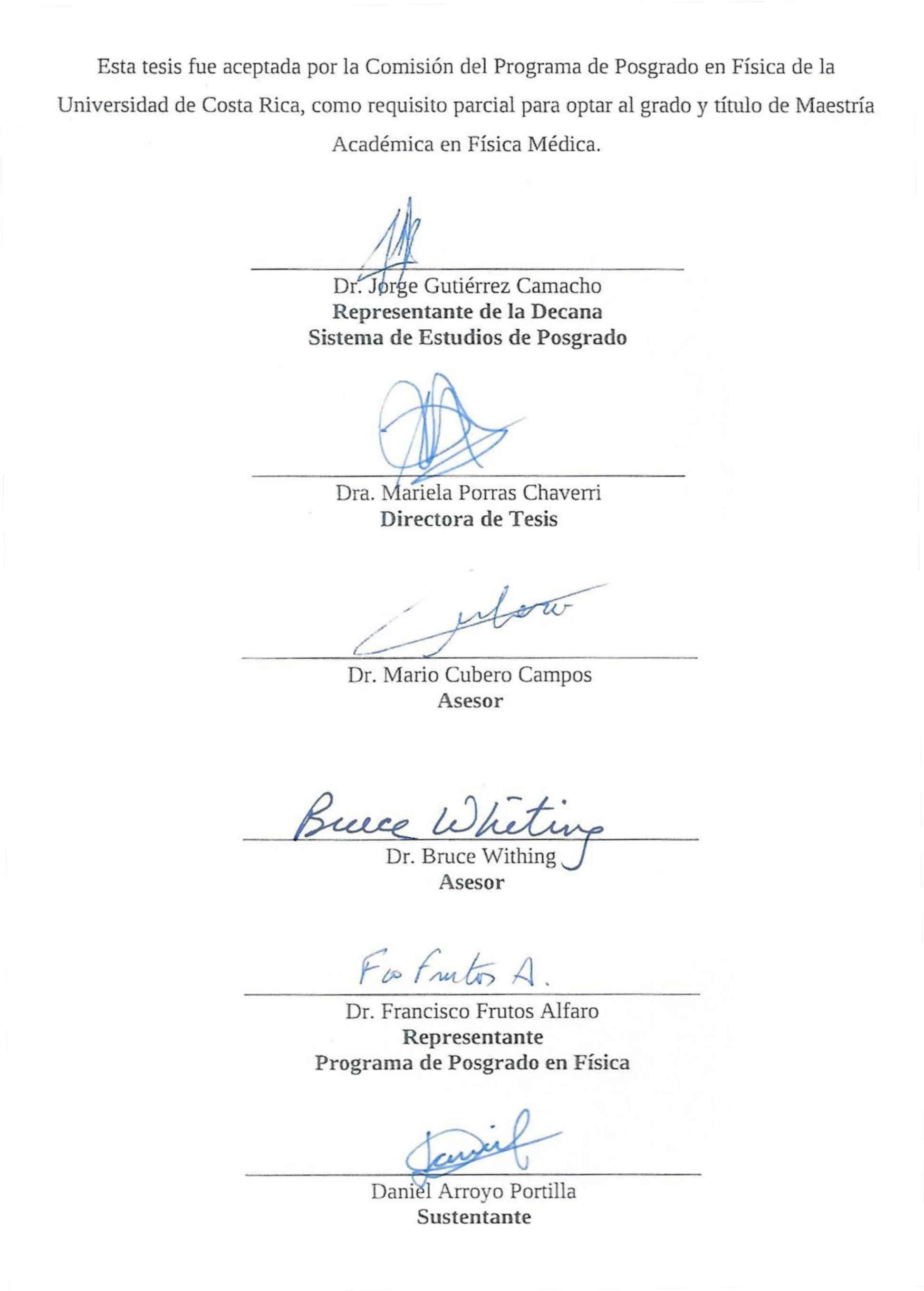

Esta tesis fue aceptada por la Comisión del Programa de Posgrado en Física de la Universidad de Costa Rica, como requisito parcial para optar al grado y título de Maestría Académica en Física Médica.

Dr. Jorge Gutiérrez Camacho
Representante de la Decana
Sistema de Estudios de Posgrado

Dra. Mariela Porras Chaverri
Directora de Tesis

Dr. Mario Cubero Campos
Asesor

Bruce Whiting
Dr. Bruce Withing
Asesor

Fco Frutos A.
Dr. Francisco Frutos Alfaro
Representante
Programa de Posgrado en Física

Daniel
Daniel Arroyo Portilla
Sustentante

Contents

Resumen en Español

ESTIMACIÓN DE LOS PERFILES DE SEÑAL PRIMARIA Y DISPERSA EN UNA TOMOGRAFÍA COMPUTARIZADA UTILIZANDO GEANT4

Se implementó un método para obtener las señales y perfiles de dispersión de una tomografía computarizada de un escáner disponible comercialmente utilizando Geant4, un kit de herramientas Monte Carlo para el lenguaje de programación C++, con el que se creó un código que imita las estructuras más importantes del escáner, como el filtro de corbatín, los elementos detectores y la rejilla de anti-dispersión. El código permite colocar un maniquí de agua uniforme de diferentes diámetros en el isocentro del escáner, para estudiar la dispersión generada por el mismo y la atenuación de la señal en la estructura detectora. El algoritmo de caracterización de señales encuentra la última interacción del fotón antes de llegar a un elemento de detector y asigna en función de los perfiles de dispersión y el volumen de interacción.

Las simulaciones sin maniquí muestran una señal cruzada de entre 1% y 2% de la señal total para todas las energías de la fuente de fotones como para las distintas colimaciones, la señal de dispersión de la rejilla es más baja excepto en los bordes de cada módulo de detección superando la contribución de las señales cruzada y dispersión del aire, la señal cruzada es aproximadamente el 0,1% del escaneo al aire (medida con el corbatín y rejilla pero si el maniquí) en el módulo central y hasta un 2% al alejarse del centro de la estructura de detección.

Las simulaciones con el maniquí presente muestran una atenuación total en la estructura de detección de hasta el 98% para el maniquí más pequeño y hasta el 99.9% para el maniquí más grande. La dispersión maniquí varía con la energía de la fuente y la colimación utilizada, generando hasta un 5% de dispersión con un maniquí de $320mm$ diámetro.

Los perfiles de dispersión normalizados ayudan a interpretar el efecto de la señal dispersa del maniquí en una proyección, las simulaciones con todas las estructuras del escáner presentes y simulaciones donde falta el filtro de corbatín y/o rejilla anti-dispersión muestran la importancia de dichas estructuras al reducir la señal de dispersión. Además, pequeñas contribuciones de señal del las estructuras del escáner y el aire se pueden identificar y evaluar para ver su impacto en la señal total.

El código desarrollado imita con éxito la señal de dispersión de un escáner de tomografía computarizada y separa las diferentes fuentes de dispersión del maniquí, las estructuras del escáner y el aire.

UNIVERSITY OF COSTA RICA

Abstract

Physics School
Postgraduate Study System

Master Degree

Estimation of Primary and Scatter Signal Profiles in Computer Tomography using Geant4

by Daniel ARROYO-PORTILLA

A method to obtain the scatter signal profiles from a commercially available computer tomography scanner, using Geant4 a Monte Carlo toolkit for C++ to create a code that mimics the most important structures of the scanner, like the bowtie filter, detecting elements and septa. A uniform water phantom with different diameters can be placed at the isocenter to study the scatter generated and the attenuation of the signal in the detecting structure. The signal characterization algorithm finds the last photon interaction before reaching a detecting element to assign based on the volume scatter profiles.

Simulations without the phantom show that the crosstalk signal is between 1% and 2% of the total signal for both source energies and collimations, the septa scatter signal is lower but at the edges of each detecting module surpassing the bowtie and air signal contributions, the bowtie signal is about 0.1% of the air scan in the central module and up to 2% when moving away from the center of the detecting structure.

Simulations with the phantom present show a total attenuation in the detecting structure of from 2% for the smaller phantom up to 0.14% for the biggest one. Phantom scatter varies with the source energy and collimation, contributing up to 5% with a 320mm diameter phantom.

Normalized scatter profiles can help to understand the effect of the phantom signal in a projection, simulations with all the scanner structures present and simulations where the bowtie and/or anti-scatter grid is missing can show the impact of the structures when it comes to reducing the scatter signal. Also, small signal contributions from the scanner structures and the air can be identified and assessed to see the impact on the total signal.

The code developed successfully mimics the scatter signal of a CT scanner and separates it into the different scatter sources from the phantom to the scanner structures and air.

List of Tables

List of Figures

List of Abbreviations

AM	**A**lternating **M**inimization
ASG	**A**nti **S**catter **G**rid
CSDA	**C**ontinuous textbfSlow **D**own **A**pproximation
CT	**C**omputed **T**omography
DECT	**D**ual **E**nergy **C**omputed **T**omography
FBP	**F**iltered **B**ack **P**rojection
FOV	**F**ield **O**f **V**iew
GPS	**G**eneral **P**article **S**ource
MC	**M**onte **C**arlo
MI	**M**olecular **I**nterference
NPC	**N**on **P**rimary **C**rosstalk
NSP	**N**ormilized **S**catter **P**rofile
SPR	**S**catter (to) **P**rimary **R**atio

List of Symbols

E	source energy
c	source collimation
n	source photons
d	phantom diameter
i	element number
T	total signal
P	primary signal
P'	bowtie signal
S	phantom signal
A	air signal
B	base signal
C	crosstalk signal from primary events
C'	crosstalk signal from non-primary events
D	septa signal
M	mixed signal
$\phi_{(g)}$	source polar angle
$\theta_{(c)}$	source azimuthal angle

Chapter 1

Introduction

1.1 Introduction

Computed tomography (CT) images are widely used when diagnosing many types of illness in patients and unlike conventional radiography-planar images, they can display several slices or axial images of the patient or studied object.

CT images are reconstructed using an algorithm and several projections or a sinogram (Willemink and Noël, 2019). Many types of CT scanners can perform this task, the design and geometry of each scanner will vary depending on the application of the center, institution, clinic, or hospital.

The proposed methodology is the development of a Monte Carlo code capable of simulating a single projection of a phantom in a computed tomography (CT) scanner, taking into account the amount of primary and scattered signals received in the detectors. The CT scanner simulated is one commercially available with dual-energy capabilities, the simulation is coded in C++ programming language with the aid of the Geant4 Monte Carlo toolkit.

The geometry of interest for this work is defined as a fan-beam X-ray source, with a curved one-dimensional detector array, a bowtie filter, and the anti-scatter grid (ASG), conventionally known as a third-generation CT scanner (Flohr, 2013). Dual-energy CT (DECT) are scanners capable of operating with two different energy sources, exploiting the different attenuation coefficient of matter and achieving a better image quality of the patient (Forghani, Man, and Gupta, 2017).

1.2 Innovation and Impact

The septa in the detector elements remove most of the scatter radiation generated by the phantom and other scanner structures, however, some of these scatter signals still reach the detecting elements. Studying the scatter components for their different scattering points, like the scanner bowtie, septa, base or crosstalk, and the air contributions can help understand better scatter patterns in the detecting structure.

Improving the image quality of CT scanners can be highly beneficial when diagnosing patients, for that, is essential to run Monte Carlo simulations that identify the different types of scatter arriving at the detectors. With several simulations and well categorized signal is possible to improve iterative reconstruction algorithms when processing images.

1.3 Problem Statement

The septa in the detector elements remove most of the scatter radiation, however, some of the scatter signals still reach the detectors. In particular, scatter from the bowtie and the forward-directed coherent scatter component makes it past the septa and reaches the detecting elements, where it is misinterpreted as part of the primary signal.

1.4 Goals

1.4.1 Main Goal

Determine the primary and scatter signal profiles in a commercially available computer tomography (CT) machine using Geant4.

1.4.2 Specific Goals

- Develop a Monte Carlo simulation code to simulate the geometry of a CT scanner, including its detector structure.
- Separate the signal received by the detector elements as primary or scatter, based on the MC transport output.
- Estimate the total and partial scatter radiation that reaches the individual detectors.

1.5 Background

The fact that sensitive volumes or detector elements cannot differentiate between primary or scattered photons, raises the importance of measuring the contribution of the scatter signal via Monte Carlo (MC) simulations (Malusek, Sandborg, and Carlsson, 2008). Simulations performed by Liu et al., 2021 show not only the reduction of the scatter signal when using an ASG but also the impact of bowtie filter, collimation, and phantom size.

Most of the scatter contribution is generated in the phantom and it is highly related to its size, Lazos and Williamson, 2010 showed no significant improvement using ASG in a cone beam CT when imaging a patient's head, however imaging the pelvic area the usage of an ASG show an enhanced improvement in dose and image uniformity leading to better image quality. The non-linear error induced by the scatter signal measured by Joseph and Spital, 1982, by measuring the attenuation values with different size phantoms, the error induced can lead to cupping, streaks, and CT number inaccuracies. The usage of an ASG can greatly mitigate the scatter signal in the detector, although will not reduce it to zero (Kyriakou and Kalender, 2007).

Undoubtedly scatter radiation hurts the image quality and CT images are no exception to this. A common measure of the scatter radiation is given as the scatter-to-primary ratio (SPR), where higher values can lead to cupping artifacts and reduction of image quality (Akbarzadeh et al., 2010). Let's not forget that photons will behave differently depending on the energy.

Many types of reconstruction algorithms can be found and most of them will use two main techniques, known as filtered back projection (FBP) and iterative reconstruction (IR). Due to its simplicity and fast reconstruction, FBP was the option of choice, but with the continuous growth of computational power, it is possible now to apply IR in a short time.

The simulations were performed using a toolkit called Geant4 implemented in the C++ programming language, the toolkit can simulate the passage of different particles through matter and can easily manage complex geometries. For this study, the photons of interest will have an energy range of up to $140 keV$, which is an operational range of the toolkit (Agostinelli et al., 2003). One additional extension used, is the materials developed by Paternò et al., 2018, whose code makes a better approach to molecular interference effects in X-ray Rayleigh or coherent scattering for the energy range of interest.

The expected signal obtained in the simulation should behave as real projections with the correct geometry setup. For example, if a phantom is present during the simulation a reduction of signal is expected in the results, removing the phantom should give the maximum amount of signal in all elements inside the field-of-view (FOV). However, results obtained by removing the ASG, which is not an available or easy option to perform in real life, give insight into the amount of scatter signal blocked and a higher amount of signal per element. Previous MC simulations may give us an insight into the expected results as seen by Wadeson, Morton, and Lionheart, 2010, others using different programming toolkits like Malusek, Sandborg, and Carlsson, 2008 and Darmian et al., 2011.

Artifact reduction and higher accuracy on material composition are some of the goals for reconstruction algorithms in CT images. Techniques such as line integral alternating minimization (AM) algorithm (Chen et al., 2016), energy detector for AM algorithm (O'Sullivan, Snyder, and Whiting, 2002) and removing metal bodies by marking them on the image (Williamson et al., 2002), are effective when improving the image quality.

The scatter characterization implemented in this project can be used in reconstruction algorithms that take into account the scatter contribution. O'Sullivan and Benac, 2007 have developed an AM algorithm able to incorporate the number of scatter photons, coming from several sources including the patient's body.

Normalized scatter profiles (NSP) and scatter-to-primary ratio (SPR) in CT scanners have been studied over the years. From experimental setups measuring fluency with beam blockers under the photon beam (Johns and Yaffe, 1982) or reading the scanner output using specialized lead beam blockers (Akbarzadeh et al., 2010). Many MC simulations have been performed (Leliveld et al., 1994, Chen et al., 2007, Engel et al., 2008, Darmian et al., 2011, Prakash and Boudry, 2017)

Chapter 2

Theoretical Framework

2.1 Interactions of the photons with matter

When it comes to photons interacting with matter in medical physics, there are five main processes to be considered: Compton effect, photoelectric effect, pair production, Rayleigh (coherent) scattering, and photonuclear interactions. The probability for each one to happen is strongly dependent on the energy of the photon and the atomic number (Z) of the interacting object.

X-ray tubes are used in CT scanners as a source of photons (Behling and Grüner, 2018), they work with different kilovoltages between the cathode and anode to accelerate the electrons, the accelerated electrons impact the target material (anode) and produce photons via two mechanisms, bremsstrahlung photons created by the slow deceleration of electron inside the target and characteristic photons, produced by a decaying atomic electron occupying a lower empty edge left by a photon hitting an electron. After filtering low energies we obtain the spectra of the X-ray source.

Considering that some of the interactions require a minimum photon energy and that the maximum voltage of the X-ray tube is $140kVp$, which sets a maximum possible photon energy of $140keV$, photonuclear and pair production interactions cannot be present since their minimum interacting energy is in the range of the MeV, $1.022MeV$ specifically for pair production.

In Figure 2.1 the plot represents the dominance of interactions that the photon will undergo as a function of atomic number (Z) and energy (MeV). The line on the left shows an equal probability of interacting as photoelectric or Compton, similarly, the line at the right is an equal probability between Compton and pair production. Image taken from Mott et al. (Mott and Daniel, 2021). Neither the Z number nor the energy of the photon has a linear dependence on which of the interactions will occur and the

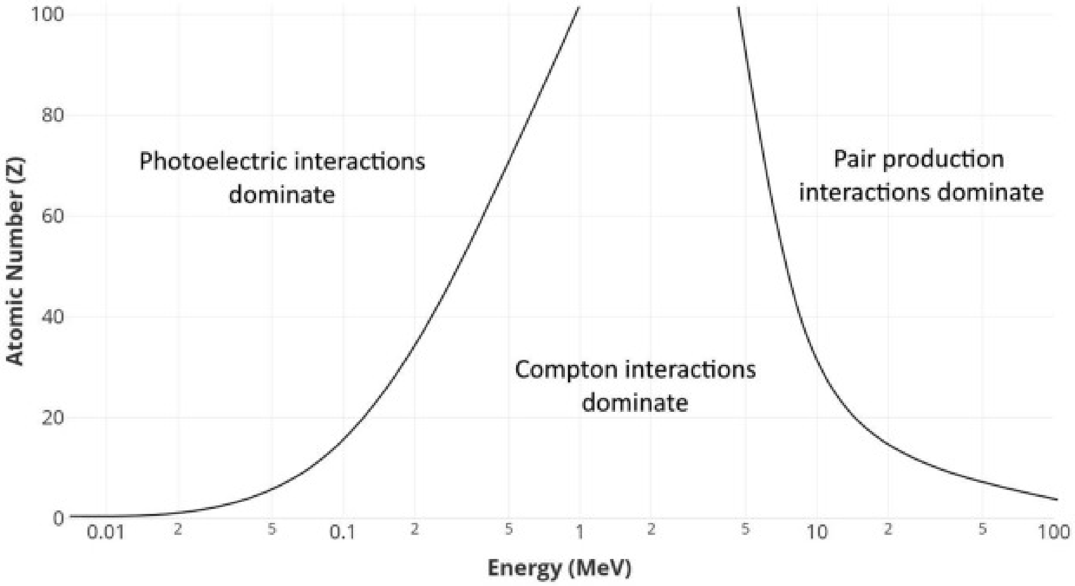

FIGURE 2.1: Photon interaction dominance in function of the energy and atomic number.

dominance can be seen in the plot, note that the coherent scattering is missing.

2.2 Mass attenuation coefficients of photons

Before analyzing the probability of a photon for each interaction, we need to estimate how many mono-energetic photons of a beam will pass through an object of a known thickness, density, and composition. This can be done by employing the exponential attenuation shown in Equation 2.1.

$$\frac{N}{N_0} = e^{-\mu x} \tag{2.1}$$

Where:

- N: Is the number of photons that passed without interacting.
- N_0: Is the number of photons before entering the object.
- μ: This is the linear attenuation coefficient of the phantom composition and the corresponding photon energy.
- x: Is the thickness or distance traveled through the object.

The units of μ are inverse of distance (cm^{-1}), the result of dividing μ over the material density (ρ) is the mass-attenuation coefficient (μ/ρ) which is a density-independent constant, generally the values of attenuation are commonly tabulated using the nomenclature grams per square centimeters (g/cm^2). The relation N/N_0 in Equation 2.1 gives the fraction of photons that did not interact in the object and subtracting it from one results in the fraction of photons that did interact.

Another property is that each one of the interactions has its mass-attenuation coefficient, for photoelectric effect is τ/ρ, incoherent scattering is σ/ρ and for Rayleigh scattering σ_R/ρ, remember that we are not considering pair production or photonuclear interactions, the sum of all the individual mass attenuation coefficients gives μ/ρ as exemplified in Equation 2.2.

$$\frac{\mu}{\rho} = \frac{\tau}{\rho} + \frac{\sigma}{\rho} + \frac{\sigma_R}{\rho} \tag{2.2}$$

Figure 2.2 shows the total mass attenuation coefficient for water which is the sum of Compton, Rayleigh, and photoelectric coefficients. The Compton effect slowly rises over other effects overcoming them near the 20 keV energy.

Values of mass attenuation coefficient were taken from the National Institute of Standards and Technology (NIST) web page using the XCOM interface (Hubbell and Seltzer, 2004), in Figure 2.2 we can see all the mass attenuation coefficients for water as a function of energy in the range from 1keV to 200keV, where both of the axes are in a logarithmic scale.

2.3 Interactions distribution fraction

To determine the type of interaction a photon will undergo, we take each of the individual mass attenuation coefficients in Equation 2.2 and divide them by μ/ρ, this shows the probability expressed as a fraction for every interaction, in Equation 2.3 is expressed in each of the fractions for photoelectric, Compton, and Rayleigh respectively.

$$1 = \frac{\tau}{\mu} + \frac{\sigma}{\mu} + \frac{\sigma_R}{\mu} \tag{2.3}$$

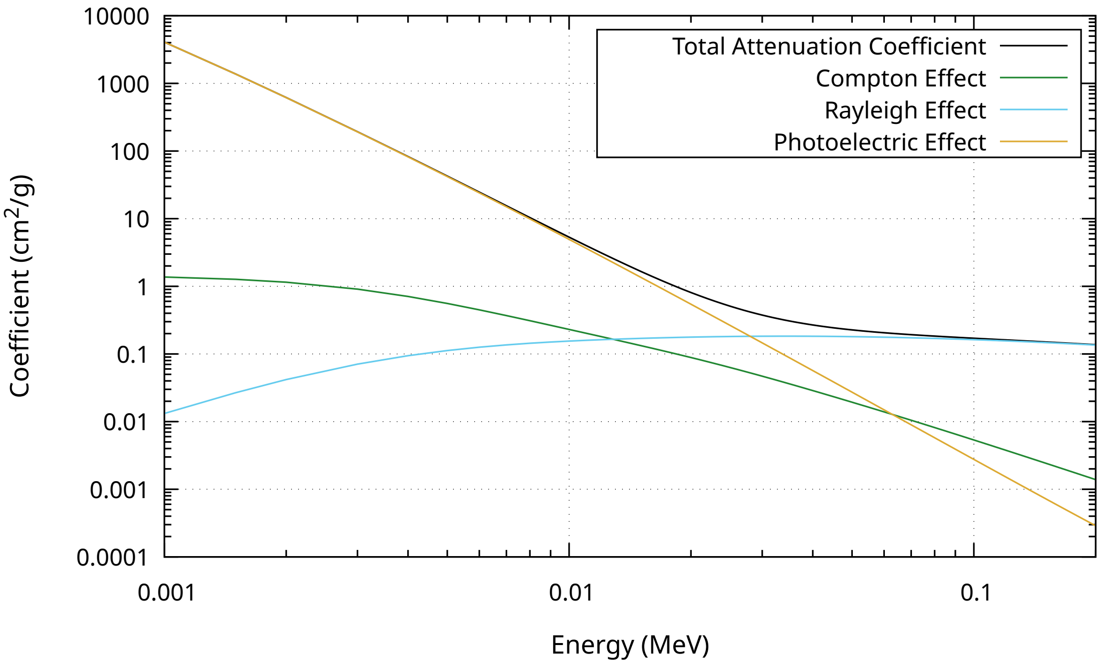

FIGURE 2.2: Mass attenuation coefficients in function the photon energy for water.

Since none of the mass attenuation coefficients depends on the number of photons of the beam, the probabilities remain constant and the path of a single photon can be determined by employing random numbers to see if the photon will interact at a determined distance (Step) and if so, with additional random numbers we can determine the type of interaction. This is the base of what a Monte Carlo simulation does to estimate the passage of a photon through an object.

2.4 Types of interactions

2.4.1 Photoelectric effect

The photoelectron which is bound to an atom is launched out of its orbit with a kinetic energy equal to the energy of the photon minus the energy required to remove him off the bound (E_b) and the kinetic energy is transferred to the atom is negligible. The dispersion angle is relative to the direction of the incoming photon and needs preservation of the momentum, an electron can be emitted between 0° to 180° as shown in Figure 2.3 with the respective angle distributions as a function of the energy.

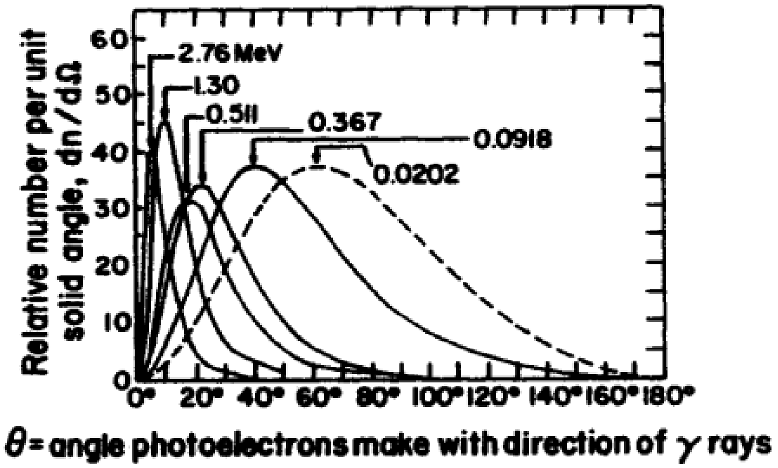

FIGURE 2.3: Relative amount of scattered electrons as a function of the solid angle for specific energies

Figure 2.3 shows the relative amount of scattered electrons as a function of the solid angle for specific energies. The curves are not normalized to each other (Attix, 2004, page 140), looking at the closest curve for the $0.1 MeV$ photon energy we see a peak close to the 40° solid angle.

2.4.2 Compton effect

Scattering interactions can be divided into elastic or coherent and inelastic or incoherent. The Compton effect or incoherent scatter aside from transferring some of the energy to the atomic electron and ejecting it, the incoming photon will also be scattered, the fraction of energy given to the electron is found by comparing the cross-section of the electron (${}_e\sigma$) by the energy transferred cross section (${}_e\sigma_{tr}$) of the electron as expressed in Equation 2.4.

$$\frac{\bar{T}}{hv} = \frac{{}_e\sigma_{tr}}{{}_e\sigma} \tag{2.4}$$

Where:

- $\bar{T}$: is the average kinetic energy of the scattered photon.
- hv: is the energy of the incoming photon.
- ${}_e\sigma_{tr}$: is the energy-transfer cross section per electron.corresponding energy.
- ${}_e\sigma$: is the cross section per electron.

In Figure 2.4, is possible to see the increment of energy transferred to the electron as the energy of the photon decreases, for the energy range of interest which is below

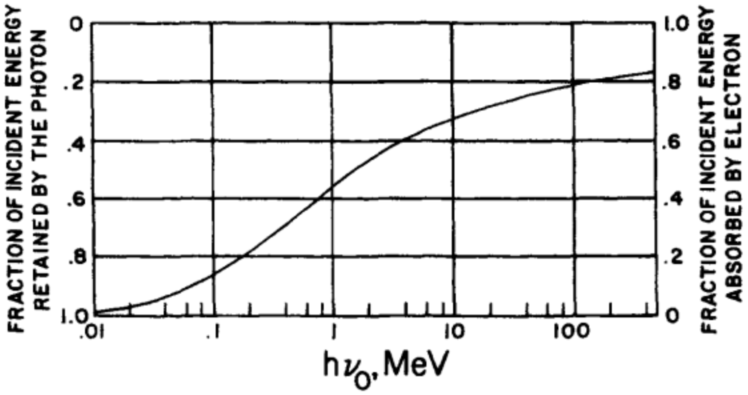

FIGURE 2.4: Compton's photon-electron energy fraction distribution in function of the incident photon energy.

200keV the fraction of energy retained by the photon is about 0.8. On the left axis is the fraction of energy retained by the photon as a function of the energy, and the right axis is the energy gained by the electron. (Attix, 2004, page 135)

The scattered electron and photons product of Compton's effect will have a preferred angle of dispersion that can be appreciated in Figure 2.5b. Figure 2.5a shows different angles for the scattered electrons and energies and Figure 2.5b is the relationship of dispersion angles for the photon and electron for a defined energy. Similarly to the previous interactions, the amount of energy transferred and dispersion angles can be determined with random numbers and that is the way to implement these interactions on a Monte Carlo code.

Figure 2.5a The vertical axis is the differential cross section from Klein-Nishina (K-N) vs the angular distribution per unit solid angle, and the solid line is the preferred angle at different energies (Attix, 2004, page 136). Figure 2.5b Corresponding angles for both, the photon and the electron at a given energy, the dashed line is for the same dispersion angle (Attix, 2004, page 129).

2.4.3 Rayleigh effect

The Rayleigh or coherent scatter is the easiest one to explain since no energy from the incoming photon is transferred to the atom, and the photon is scattered with a slight change in direction, this change depends on the energy of the photon and can be determined by viewing the scatter angle distribution for the specific energy and with random numbers to select the final direction. Several measurements to obtain the photon scattering cross-section in water are taken by Morin, 1982 at different water temperatures.

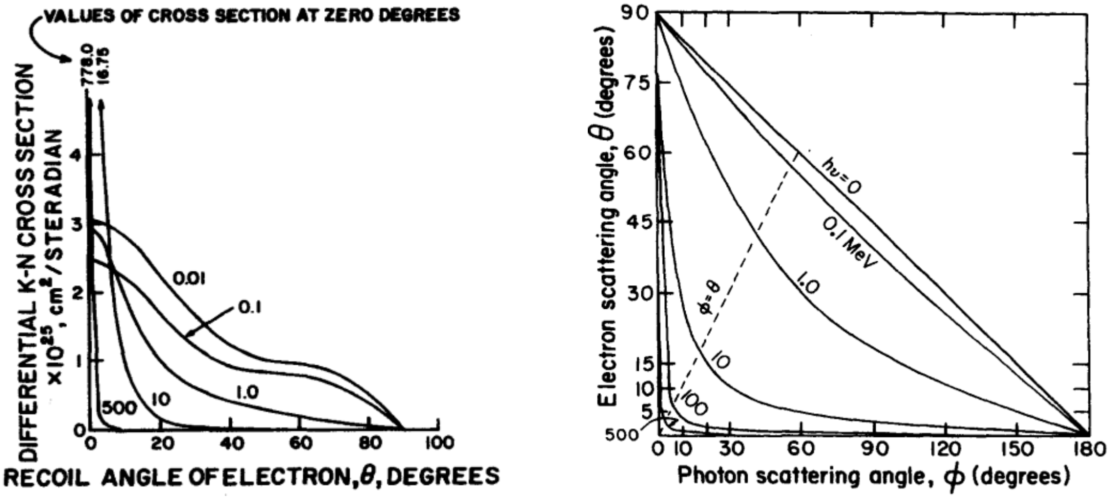

(A)

(B)

FIGURE 2.5: (A) The vertical axis is the differential cross section from Klein-Nishina (K-N). (B) Photon and the electron dispersion angles at a given energy

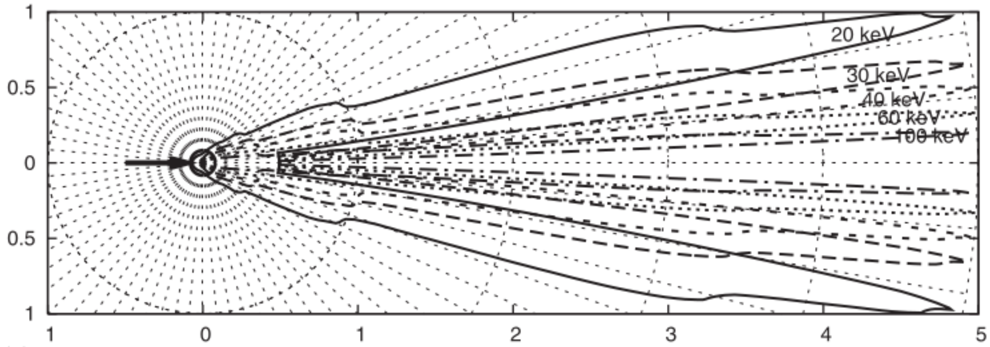

FIGURE 2.6: Polar representation for the scattering cross-section for water.

Figure 2.6 is the polar representation of the coherent scattering cross-section for water shown by Midgley, 2006, where the effect of increasing the photon energy results in the narrowest scattering angle for the interacting photons. Image taken from Midgley, 2006.

2.5 Electrons traveling in matter

A kinetic electron traveling through matter will slowly reduce its energy until it comes to a stop, the total stopping power ($dT/\rho * dx$) is the sum of two constants: the collision stopping power is the rate of energy loss per distance unit and is caused by coulomb interactions that result in ionization and excitation of atoms; and the radiative stopping

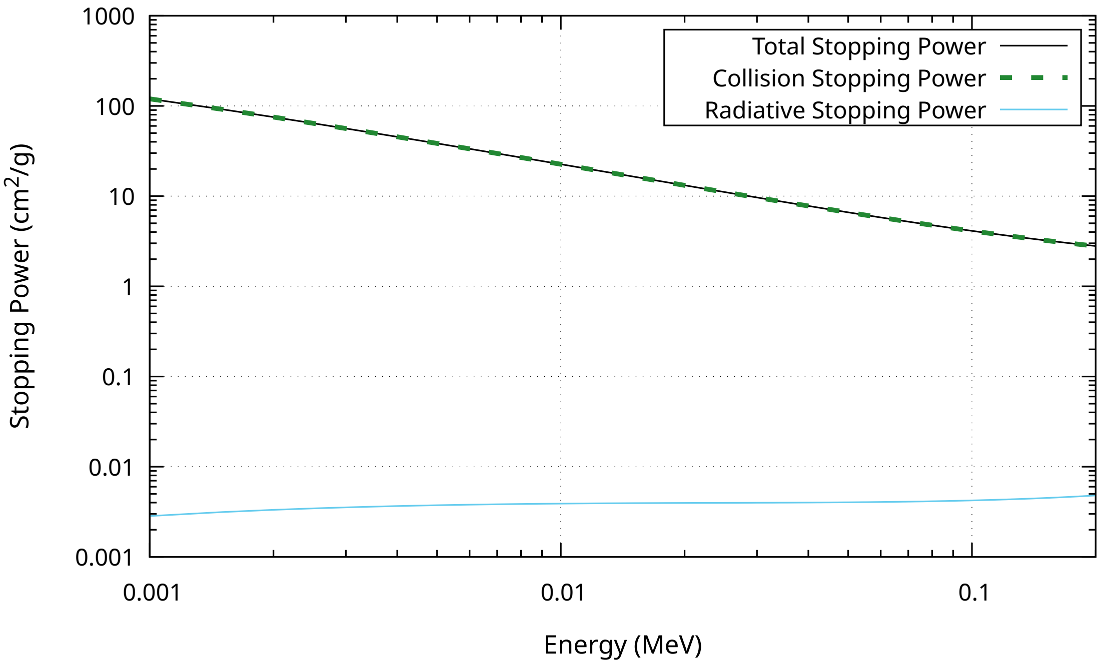

FIGURE 2.7: Stopping power for water at different photon energies.

power that is the rate of energy loss due to atoms and electrons resulting on the emission of bremsstrahlung photons. All the stopping powers are plots in Figure 2.7 for water where is possible to see that the contribution of the radiative stopping power is negligible. Data was obtained using the ESTAR platform on the NIST (Berger et al., 2010).

The lines in Figure 2.7 are the different stopping powers as a function of the energy. The total stopping power is about the same as the collision stopping power. The contribution of the radiative stopping is at least 2 orders of magnitude lower than the collision-stopping power. (Berger et al., 2010)

The projected range is an approximation of the final depth of a charged particle until rest, for low Z material it is comparable with the continuous slow-down approximation (CSDA) range, for example, a $150keV$ electron moving on water with $\rho = 1g/cm^2$, the CSDA range is about $0.3mm$, deposing all its kinetic energy along the path. It is possible to simulate the passage of the electrons if the application requires it, the tortuous path of electrons and its constant change of direction can be determined using random numbers and small steps.

2.6 Monte Carlo approximation and Geant4

The decision-making based on random numbers for photons traveling in the matter, the type of interaction a photon will undergo, dispersion angles, or similar judgments is what we call a Monte Carlo simulation. The general topic of interest in medical physics is the estimation of energy deposed in objects or absorbed dose, the unit of dose is Grey (Gy) which is equal to energy divided by matter. By simulating several photons and following their path through a defined geometry and materials, it is possible to obtain an accurate result of dose. These simulations can be helpful in medical applications, like dose estimation in internal organs, calibration of equipment, improvement in reconstruction algorithms, and more.

The Monte Carlo toolkit used to perform the simulations is Geant4, the product of two independent studies one at CERN and the other at KEK in 1993. With the advances made in modern computing techniques, they improved the original program Geant3, giving birth to the first collaboration of Geant4 in January 1999 as a free and open toolkit (Agostinelli et al., 2003).

The diagram follows a bottom-to-top category usage. The key domains determined in Geant4 for a simulation are geometry and material, particle interaction in matter, tracking, digitization and management, event and track management, visualization and visualization management, and user interface. The top of the category diagram is shown in Figure 2.8, showing the structure and dependencies of each of the processes from top to bottom. Image taken from Agostinelli et al., 2003.

Laying at the bottom of the diagram in Figure 2.8 is found the `Global` category that contains the system of units, constants, and, random numbers. Above `Global` is found the `Graphical Representation`, `Geometry`, `Material`, `Particle` and `Intercoms`, the `Intercom` category act as a communication path for the Geant4 interfaces or between different modules. Next is found the `Track` category that follows the particle through the different steps. Higher up is the `Tracking` category is used to keep a record of the different interactions in the sensitive volumes in `Digits+Hits`, the underneath category `Process` contains the physical interactions models. The `Run` category manages a set of events sharing the same beam and detector, and the Event category manages the tracking. And finally, the `Visualization`, `Readout` and, `Persistency` categories were created to access the toolkit for different interfaces.

The size of the step is a critical variable for the computational time, in Geant4 the step is defined taking into account all the physics processes and defining an optimal

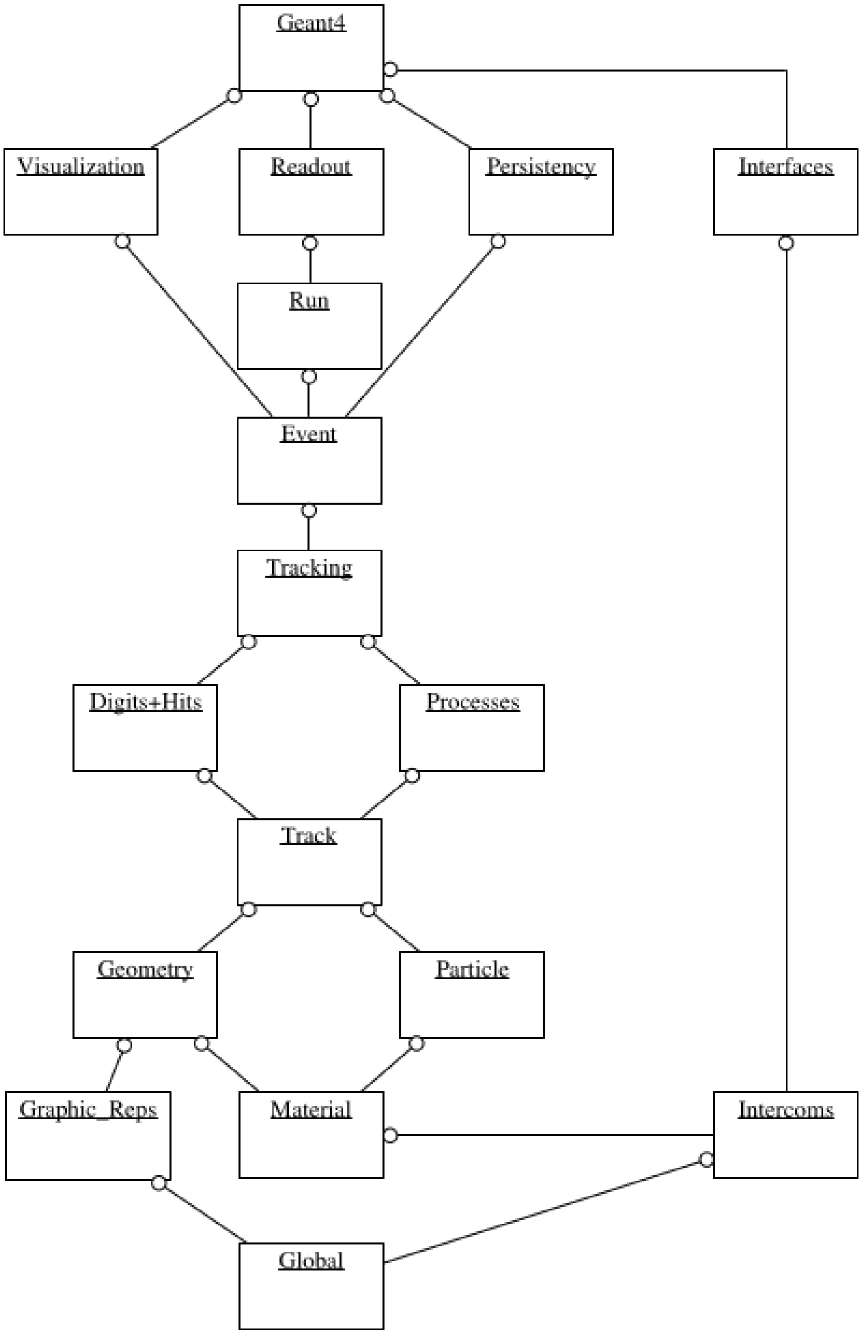

FIGURE 2.8: Geant4 toolkit category hierarchy diagram.

size without compromising the tracking precision.

Chapter 3

Methodology

A good computed tomography (CT) Monte Carlo (MC) simulation relies on several factors, starting from the code, computational cost, realistic geometry, accurate photon source, and so on. This chapter explains each one of the factors and its importance to the simulation.

Using as a starting point the code developed by Arroyo-Portilla et al., 2021, capable of imitating the signal of a CT scanner, several improvements will be made to the code to achieve a more realistic MC simulation. On a general review, this code can run mono-energetic simulations, with the standard electromagnetic physics list provided by Geant4 and the option to place a phantom or the anti-scatter grid (ASG), also known as septa.

3.1 CT scanner geometry

The four main components of a third-generation CT scanner (Flohr, 2013) are the photon source, bowtie filter, phantom, and detector structure as shown in Figure 3.1. In the center of the image is found the isocenter of the CT scanner, where the phantom or studied object is located. At $645mm$ on top of the isocenter is the source point, represented with a green cross. The bowtie filter is $19cm$ below the source and represented with two blue triangles, since the real shape of this object is proprietary no more information will be discussed about the geometry. The detecting structure represented as a grey arc is composed of 51 detecting modules with the ASG or septa, the central module is located $54cm$ below the isocenter.

3.1.1 Photon source

The tungsten spectra energies (E) to be reproduced are the same used by Evans et al., 2013 for $e = 90kVp$ and $e = 140kVp$ voltage X-rays tubes, see Figure 3.2 empty squares and circles spectra curves. To include in the initial code the energy spectra, a Geant4 default utility called general particle source (GPS) is used, it comes in handy when creating

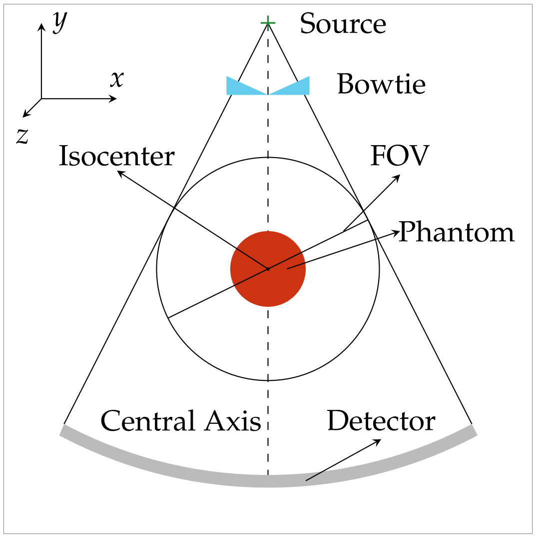

FIGURE 3.1: A non-scale CT scanner geometry configuration of the structures.

different types of sources: choosing between point, planar, or volumetric distributions, the shape of the source, location, particle momentum, and energy distributions.

To match the desired source for the simulations, an isotropic punctual photon source is placed 645mm above the isocenter. The field of view (FOV) is the maximum diameter of a circle placed at the isocenter that fits inside the solid lines in Figure 3.1, using spherical coordinates is defined by the polar angle (ϕ) between the solid lines, Equation 3.1 is the formula for a defined FOV of diameter d (mm).

$$\phi_{(d)} = 2 \cdot Sin^{-1}\left(\frac{d}{2 \cdot 645mm}\right) \tag{3.1}$$

The collimation is the azimuthal angle (θ), which is the z-axis distance covered at the isocenter equally distributed between the negative and positive z-axes, Equation 3.2 is the relation used to obtain the angle for a desired collimation c (mm).

$$\theta_{(c)} = 2 \cdot Tan^{-1}\left(\frac{c}{2 \cdot 645mm}\right) \tag{3.2}$$

To check that the energy of the source photons follows the same energy distribution of the spectra, a small simulation recording every source photon energy is executed, once the simulation is finished we recreated the GPS output energy spectrum. All data, the provided points, and output are normalized to the highest values and displayed in Figure 3.2. The empty circles and squares are the provided spectrum points and the solid lines correspond to the output data from the GPS utility. The circles and squares

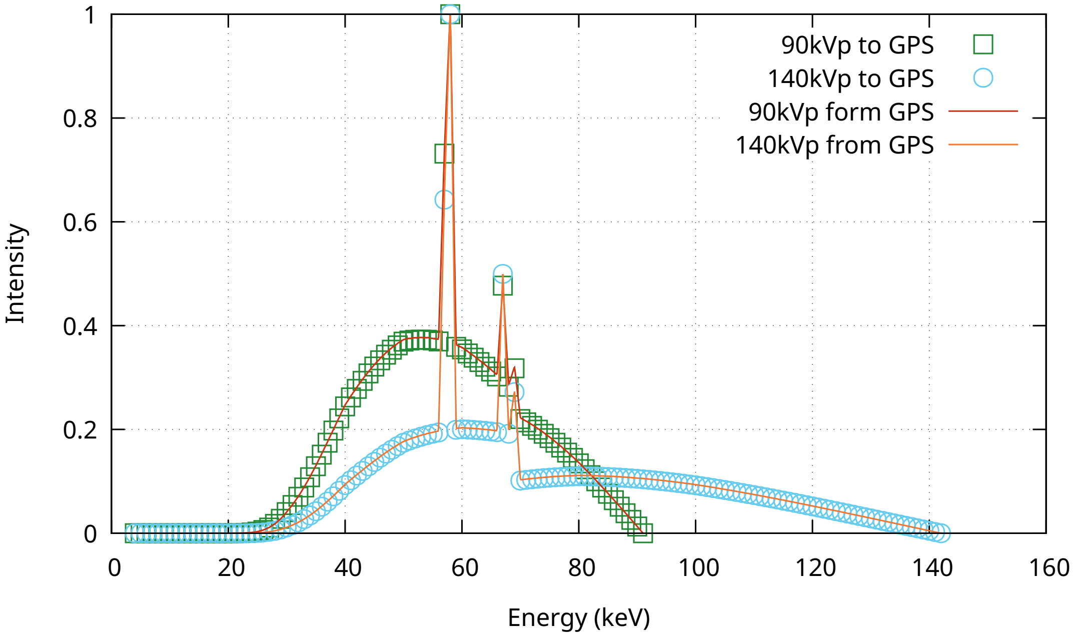

FIGURE 3.2: Tungsten spectra for $90kVp$ and $140kVp$ energies.

are the provided points to the GPS utility normalized to the highest value for each energy. The solid lines are the output spectrum for each corresponding energy.

3.1.2 Bowtie

The bowtie filter is a scanner structure designed to flatten the signal in the detecting elements (Mail et al., 2009), the bowtie is made of Teflon material and is one of the last structures to be added to the code. The computational cost drastically increases due to how close it is to the source and that the FOV is completely submerged in this structure, this means that every source photon will likely pass through this non-air structure. As mentioned earlier, it is not possible to give more details about the geometry shape, or dimensions.

3.1.3 Phantom

Phantoms are reference objects designed to perform tests and quality controls in CT scanners, different phantom geometries, densities, and configurations are scanned to verify the reliance of the machine. The initial code has a cylindrical water phantom of $21cm$ diameter and $4cm$ height without casing, which can limit the scatter generated at high source collimation numbers.

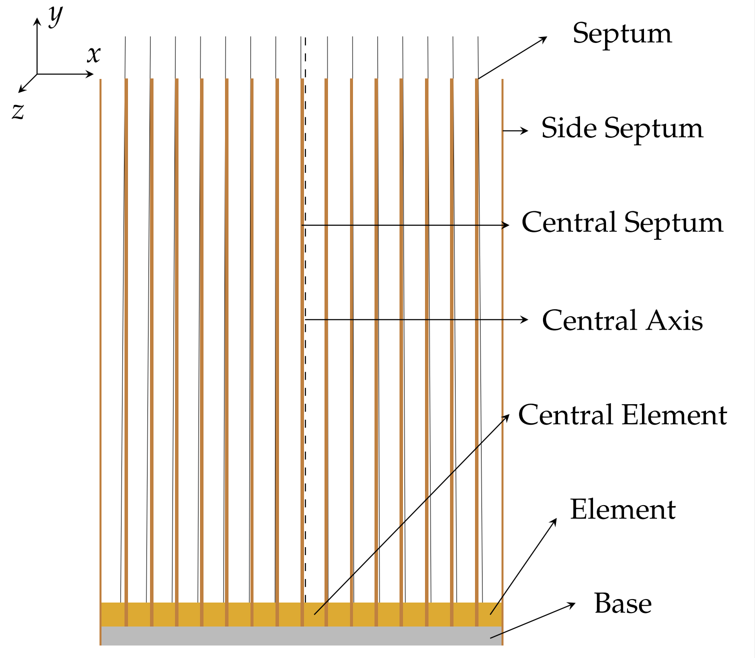

FIGURE 3.3: A non-scale image of the geometry of a module with detecting elements, base and septa.

The new water phantom dimensions will change for the final simulations, including the PMMA casing. The height of the casing is $254mm$ inches long, with three different diameters (d): $215.4mm$, $270mm$, and $320mm$. The walls of the casing are $6.35mm$ thick for the round section and $25.4mm$ thick for the top and bottom lids.

3.1.4 Detector

The central detector module is shown in Figure 3.3, and the detector structure (grey arc) in Figure 3.1 is made of 51 of these modules each one placed along $1185mm$ radius arc and equally distributed on a 57° angle, the radius is measured from the center of the arc to the top surface of the central element, and all the septum are parallel within the same module and the central blades are the only ones radially parallel to the center of the arc. Note that the central axis in Figure 3.3 is not aligned to the central septum, but it falls slightly to the right, on top of the central element, this offset will be implemented later in the code.

The 16 detecting elements placed on top of the base and between two septa in Figure 3.3 are the scoring volumes in the code. The 15 middle blades are also placed on top of the base and the two blades septa are the starting and finishing volumes of the module across the x-axis. The photo-diode base is the starting volume of the photocathode tube

TABLE 3.1: Detecting module components, dimensions and materials.

Volume	**Dimensions (mm)**			**Material**
	x	y	z	
Element	1.25	1.25	1.4	Gadolinium oxysulfide
Septum	0.08	29	54	Molybdenum
Side Septum	0.04	30	54	Molybdenum
Base	21.2	0.75	1.4	Silicon

(Shefer et al., 2013).

All the materials and dimensions are listed in Table 3.1, the slice thickness or z-distance of the module in Arroyo-Portilla et al., 2021 code is $1.4mm$, but in the new code, the septa structure will have a $54mm$ thickness while the rest of the structures remains the same. The total height of the module is defined by the side blade encapsulating all the volumes. The elements are counted continuously from the first module on the left to the last module on the right, thus, the central module element range is from 401 to 416.

The dimensions and material are displayed in Table 3.1, for every geometric structure inside a module. See Figure 3.3 to see the details of the module.

Considering on the central module that the septa are at least 23 times taller than the element height and that only the central septum is radially parallel to the source, an increasing reduction of the signal should be observed in simulations with septa as we move to elements farthest from the central axis.

The shadow generated at the top surface of each element can be obtained by projecting lines from the source that passes through the farthest top edge from the central axis of each septum, Table 3.2 shows the percentage of surface blocked by each septum on top of the elements. These projections are the black solid lines in Figure 3.3, all the lines intersect at the source along with the central axis. Septa transmission at different source angles has been studied by Bernstein et al., 1983.

TABLE 3.2: Percentage area blocked on top detecting elements by septum.

Element	**Shadow area (%)**	**Element**	**Shadow area (%)**
401	18.3	409	0
402	15.7	410	2.3
403	13.2	411	4.8
404	10.6	412	7.4
405	8.1	413	10.0
406	5.5	414	12.5
407	3.0	415	15.1
408	0.4	416	17.6

3.2 Geant4 details

3.2.1 Geant4 physics lists

The physics list in Geant4 plays one of the most important roles in the simulation, this mandatory class is in charge of the physics models that will rule every particle during the MC transport, the particle type and energy are fundamental when choosing the physics list, let us remember that photons up to $140keV$ can come out of the source. In this section two of the physics lists provided by Geant4 will be studied: the standard ($G4EmStandardPhysics$) and the Penelope with molecular interference (MI) implementation ($G4EmPenelopePhysicsMI$).

Consulting the Geant4 physics list guide we can obtain the particle interacting models for photons. For the standard physics list, the Compton scattering follows the Klein-Nishina model while photoelectric and Rayleigh effects the Livermore model. On the other hand, the Penelope physics list in Compton scattering, for energies bellow $20MeV$, uses the Monash University model, photoelectric and Rayleigh effect is the same as the standard physics list, but with the molecular interference implementation used by Paternò et al., 2018.

A simple simulation set-up, consisting of a mono-energetic punctual pencil beam aiming in a small $4mm$ radius water orb, where we can save the first interaction type and the azimuthal scattering angle of the photons, will let us obtain the scattering photon distribution for the Compton and Rayleigh effects combined. In Figure 3.4 are the results of this simulation for $30keV$, $50keV$, $70keV$, and $100keV$ pencil beams, the MI implementation mostly affects the scattering angles from 0-20 degrees where the Rayleigh scattering is dominant.

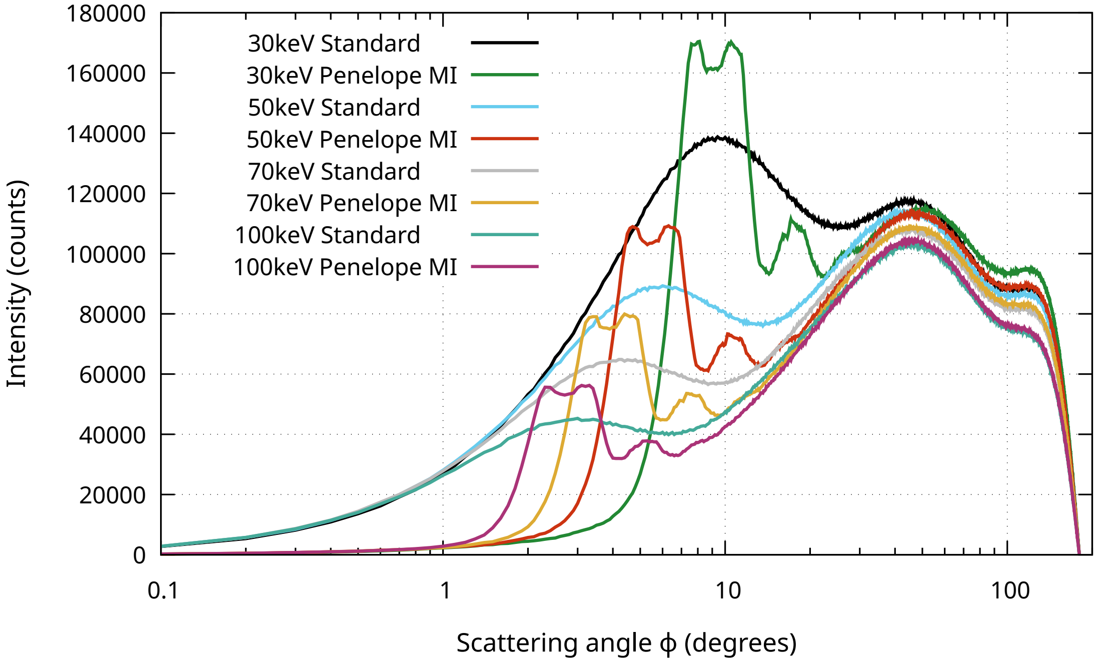

FIGURE 3.4: Geant4 physics standard physics list comparison against molecular interference model.

Figure 3.4 is a comparison between the standard physics list and the Penelope with MI incorporated physics list using $1e^9$ mono-energetic photons. We can observe the scattering distribution for different photon energies ($30keV$,$50keV$, $70keV$, and $100keV$) that for angles smaller than 30 degrees the shape of the curves drastically changes for each physics list.

A separate set of mono-energetic simulations will be done to observe the difference when changing from the standard physics list to the Penelope with MI physics list, in Chapter 4 an increase of signal is observed after using the new physics list.

3.3 Signal characterization

An MC transport simulation outputs lots of information, our analog simulation in Geant4 will track a source photon from start to end, using several steps between the different volumes and interactions, once this photon ceases to exist the toolkit will start transporting every secondary particle from start to end. This is known as a history, and several of these histories are needed to perform a useful simulation.

An algorithm that filters and saves the useful information from the MC transport, and that organizes the energy deposed in the detecting element by primary signal, primary crosstalk, non-primary-crosstalk (NPC), and other scatter signals profiles organized by corresponding volume, are shown as a flow chart in Figure 3.5, this algorithm will be implemented in the code.

This section will explain everything in the flow chart in Figure 3.5, as mentioned earlier the tracking of a particle is based on several steps, these steps carry information like the particle type, location, direction, energy, energy transferred to the volume, type of interaction, tracking number and others. The next list explains every decision node of the flow chart:

1. Traveling photon?
   A photon passing through matter will not depose energy on the volume and can be safely ignored.

2. Particle on main track?
   The main track is the first track and only source photons can be in this track. The tracking number changes when the source photon dies through photoelectric absorption or escaping the simulation boundaries, Compton or Rayleigh effects do not change the tracking number.

3. Particle inside element?
   Secondary particles in non-main tracks can be either spawned photons or electrons. Photons can depose energy via Compton or photoelectric effects and electrons by traveling through matter. Only the contribution inside detecting element volumes is of interest.

4. Photon inside element?
   This is an interacting source photon, this photon can interact with one or different volumes before reaching a detecting element. Every interaction, that can be Compton, Rayleigh, or photoelectric effect, is saved on memory along with the volume of occurrence, only the last interaction before reaching the element is saved. This is later used to assign the deposed energy to the corresponding signal profile.

5. Interacted outside?
   The source photon is interacting inside a detecting element, if there is no saved information of previous interactions, this means that the signal can be primary or crosstalk from primary photons, otherwise, is signal from other structures of the scanner or crosstalk from non-primary photons.

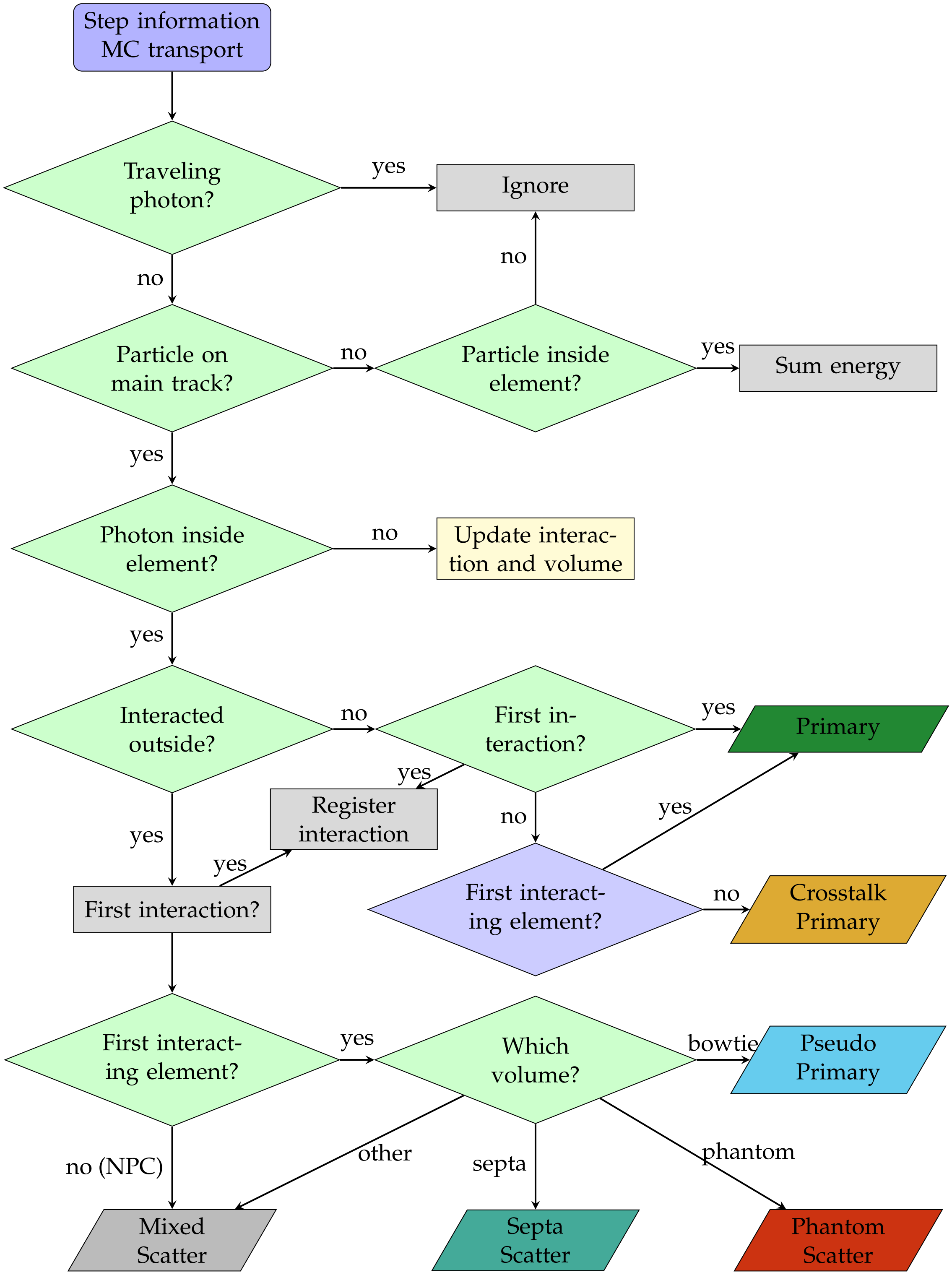

FIGURE 3.5: Used algorithm to sort useful information from every step while tracking particles on an MC transport simulation.

6. First interaction?
   Source photons can interact more than once inside the detecting elements, in this case, only the first interaction and element number are saved. This question occurs twice in the flow chart, the green diamond decision node is used to check if the signal is primary and to save the information. The gray rectangle process is just to save the values.

7. First interacting element?
   Similar to the last item, this question is used two times along the flowchart and serves to check if the signal is crosstalk between the detecting elements or not. In the blue diamond decision node, the primary signal is if the photon did not escape the initial detecting element, otherwise, we have a crosstalk signal from primary events. On the green diamond decision node, if the photon escaped the first interacting element, the signal is crosstalk from non-primary photons.

8. Update volume?
   If this non-primary source photon stays within the first interacting element, the signal will be assigned using the saved information in the yellow rectangle process node, resulting in possible signals from the phantom, bowtie, septa, photo-diode base, or air. Due to a large number of signals, the mixed scatter signal will be the contribution of non-primary crosstalk, air, base, and septa signals.

The final results store the energy deposed for the total or partial contributions in every detecting element. The signal can be displayed by volumes, like the phantom, bowtie filter, or other structures, and also by the type of interaction, Compton, Rayleigh, or photoelectric. For example, it is possible to display the phantom scatter profile as a total contribution of the different interactions, as well as display only the Rayleigh effect coming from it.

3.4 Standard deviation and percentage error

The standard deviation formula used in Arroyo-Portilla et al., 2021 code is the "Textbook Algorithm" explained by Chan and Lewis, 1979 as expressed in Equation 3.3, where is found not to be the best algorithm for precise arithmetic problems.

$$\sigma = \sqrt{\frac{\sum_{i=1}^{m}(x_i^2) - \frac{\left(\sum_{i=1}^{m} x_i\right)^2}{m}}{m-1}} \tag{3.3}$$

The new standard deviation formula is the "Two-Pass Algorithm" also studied by Chan and Lewis, 1979, this algorithm will be computed after finishing the simulation with two steps, the first one is computing the mean energy in each detecting element using Equation 3.4.

$$\mu_i = \frac{\sum\limits_{j=1}^{n} (e_{ij})}{n} \tag{3.4}$$

Where:

- μ_i: Is the mean energy in each detecting element i.
- e_{ij}: Is the energy contribution for each history j, in detecting element i.
- n: Is the total number of source photons simulated.

Once with the mean energy for each detecting element, the second step of the algorithm is to compute the standard deviation using the formula in Equation 3.5.

$$\sigma_i = \sqrt{\frac{1}{n-1}\sum_{j=1}^{n}(e_{ij} - \mu_i)^2} \tag{3.5}$$

Where:

- σ_i: Is the standard deviation in the detecting element i.
- n: Is the total number of source photons simulated.
- e_{ij}: Is the individual energy deposited from each history j, in detecting element i.
- μ_i: Is the mean energy in a detecting element i.

As expected not all the photons will interact with one detecting element, let's say n' is the number of histories that deposed energy in an element i, resulting in a range from 1 to n' histories. The sum inside Equation 3.5 can be expressed in two energy contributions, the non-zero histories that interacted with the element i and the rest that did not contribute. In Equation 3.6, both contributions.

$$\sum_{j=1}^{n}(e_{ij} - \mu_i)^2 = \sum_{j=1}^{n'}(e_{ij} - \mu_i)^2 + \sum_{j=n'+1}^{n}(0 - \mu_i)^2 \tag{3.6}$$

To obtain this sum is necessary to save the contribution of each one of the histories from all the elements and save them in memory. With the mean value already computed and all the histories available is possible to fulfill this task.

The percentage error is calculated using the formula in Equation 3.7.

$$\%error = \frac{100 \cdot \sigma_i}{\sqrt{n} \cdot \mu_i} \tag{3.7}$$

Chapter 4

Implementation of Monte Carlo code

In this chapter are explained the steps to develop the Geant4 Monte Carlo (MC) code from the initial version to the last implementation, all the changes are explained in Chapter 3. The first code starts with a mono-energetic source, a cylindrical water phantom, and the detector structure, the physics list used is (`G4EmStandardPhysics()`) standard library provided by Geant4. The idea in making small changes to the code and testing is to easily find and fix bugs, with the benefit of tracking the results with the different simulations.

The initial version of the code is a modified version of one of the examples in Geant4's example, specifically the `exampleB3b` designed to simulate a positron emission array, the base code and the modularization of the detector structure made a good starting point to develop the first version of the code (Arroyo-Portilla et al., 2021).

The final version of the code has a bowtie placed just under the source, phantom materials that include molecular interference effects, a full energy spectrum for $90kVp$ and $140kVp$ X-ray tubes, and the capability to characterize the scatter radiation by saving the last non-element photon interaction and storing the volume and type of process and crosstalk signals. All these changes to the code are performed in the next sections.

4.1 Change source photon generator

Swapping the source generator of the MC code should not represent a significant change in the results, but it can be used as a starting point for the next simulations. The general particle source (GPS) utility included in Geant4 is more practical because the source is defined after compiling the code while running the simulation. For the set of simulations in this section, the source is defined as a punctual mono-energetic gamma source placed $645mm$ above the isocenter, with an isotropic distribution limited by the field of view (FOV) and collimation explained in Chapter 3.

TABLE 4.1: Simulations using Geant4 GPS implementation with mono-energetic sources. Figure 4.1 shows the results.

Simulation	**Energy (keV)**	**Phantom (mm)**	**Septa**
$A1$	45	no	no
$A2$			yes
$A3$		210	no
$A4$			yes
$A5$	80	no	no
$A6$			yes
$A7$		210	no
$A8$			yes

To replicate the energy deposed in the detecting elements from Arroyo-Portilla et al., 2021, eight simulations were run for two different source energies and different geometry configurations, Table 4.1 shows the different source energies and geometry set-ups used in the simulations for 10^9 source photons each. These are $45keV$ and $80keV$ mono-energetic source simulations, using $c = 12mm$ collimation and $g = 284.6mm$, a cylindrical $210mm$ diameter phantom $40mm$ height placed at the isocenter of the scanner.

In Figure 4.1 are the results of the simulations shown from modules 14 to 36 that are completely inside the FOV. Air simulations (phantom-less) can be easily identified in simulations $A1$, $A2$, $A5$, and $A6$ from Table 4.1, because no significant attenuation of the signal is observed across the modules, contrary to simulations A3, A4, A7, and A8 with the highest attenuation located on the central module matching the largest phantom distance to be traveled by photons. Also, the energy deposed in simulations using a $80keV$ is higher than the analogous simulations with the $45keV$ energy.

Normalized values of the elements in the central module are tabulated in Tables 4.2 and 4.3 for $45keV$ and $80keV$ respectively. Two separate normalizations were done to show different effects: Central-axis (CAX) normalization divides the energy deposed in each element by the energy deposed in the 409 element of the $A1$, $A2$, $A5$, and $A6$ simulations for the corresponding photon energy and septa configuration. Air normalization is obtained by dividing the energy deposed in each element on a simulation with a phantom present by the corresponding air simulation with the same photon energy and septa configuration.

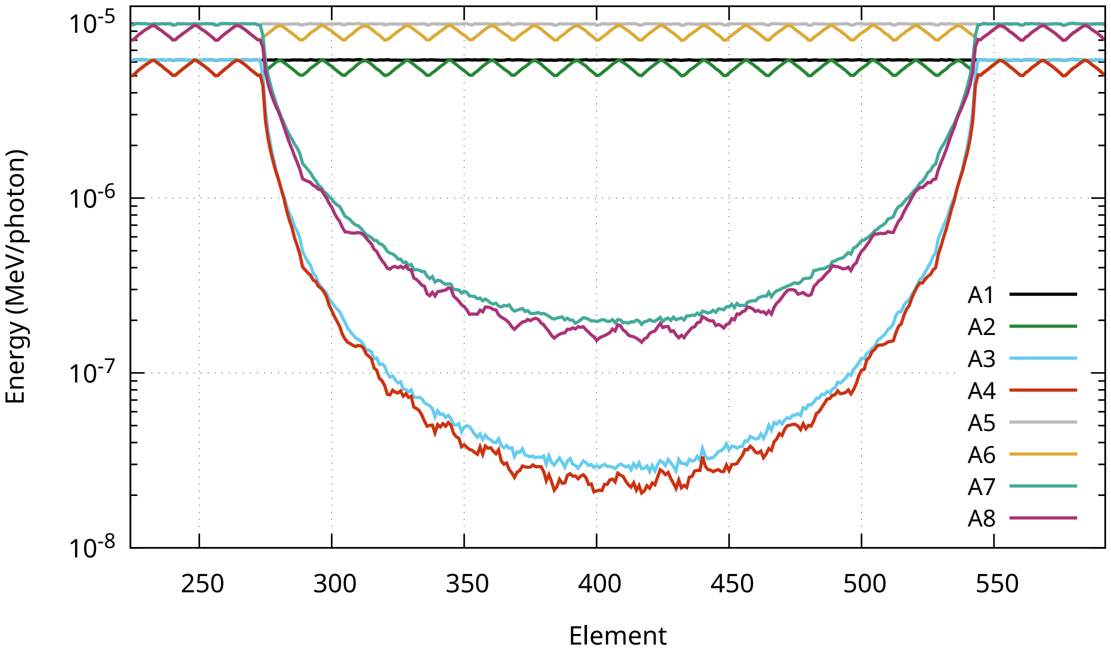

FIGURE 4.1: Raw data using Geant4 GPS implementation with mono-energetic sources. The key represents the number of the simulation in Table 4.1.

Continuing with tables 4.2 and 4.3, results for $A1_{Cax}$ and $A5_{Cax}$ shows and uniform distribution of full signal across the central module, as expected for simulation without septa, contrary to simulations $A2_{Cax}$ and $A6_{Cax}$, where a decrease between 16% to 18% is observed on the sides of the module, this reduction in signal is explained in Chapter 3, although results in Table 3.2 are with the small central axis offset the attenuation in signal is similar. A similar effect can be observed in results $A3_{Cax}$, $A4_{Cax}$, $A7_{Cax}$ and $A8_{Cax}$ with a phantom present.

To remove the inconvenient signal reduction effect at the sides of the modules caused by the septa, the data will be displayed using air normalizations in further charts. Now, in the Arroyo-Portilla et al., 2021 results, the signal attenuation due to the presence of the phantom, for the 45keV and 80keV energies simulations in the central module, is similar to the results obtained in tables 4.2 and 4.3 in air normalizations, giving a starting point for the next implementations of the code in the next sections.

TABLE 4.2: Normalized values for elements in the central module at $45keV$ source photon energy.

Element	**Normalization (%)**					
	Air		**CAX**			
	$A3_{Air}$	$A4_{Air}$	$A1_{Cax}$	$A2_{Cax}$	$A3_{Cax}$	$A4_{Cax}$
401	0.467	0.423	100.2	82.62	0.468	0.350
402	0.478	0.410	100.5	84.88	0.481	0.348
403	0.486	0.431	100.6	87.58	0.489	0.377
404	0.475	0.420	100.3	89.92	0.476	0.377
405	0.474	0.433	100.1	92.48	0.475	0.401
406	0.469	0.423	100.6	95.48	0.471	0.404
407	0.460	0.399	100.3	97.68	0.461	0.390
408	0.478	0.436	100.4	100.4	0.480	0.437
409	0.490	0.426	100.0	100.0	0.490	0.426
410	0.482	0.430	100.1	97.59	0.482	0.419
411	0.469	0.412	100.6	95.33	0.472	0.394
412	0.476	0.404	100.6	92.89	0.479	0.375
413	0.452	0.403	100.6	90.30	0.455	0.364
414	0.490	0.439	100.6	87.75	0.493	0.385
415	0.467	0.412	100.4	84.83	0.469	0.349
416	0.497	0.451	100.2	82.53	0.498	0.372

4.2 Molecular interference (MI) materials

The physics list importance is explained in Chapter 3, the idea is to change the standard library to one with better models for low-energy photons. For this, two separate simulations are executed: the first one matches the scatter rings in a scoring screen done by Paternò et al., 2018; once verified that the physics library works properly we simulate the CT model.

Images in Figure 4.2 are displayed using 0 to $100keV$ energy window. Image 4.2a are the scattering patterns using the standard library, while in image 4.2b the scattering rings at 8° and 12.5° are present when the MI is turned on. This experiment is meant to observe the two scattering rings performed by Paternò et al., 2018.

The MC code can easily modify the geometry configuration, such as the number of slices, modules, and elements, the experiment setup consists of a detecting screen with $400x400$ elements era placed under a $1mm$ thick hydroxyapatite insert, covered by a $5cm$ cylindrical breast phantom, a $2mm$ photon pencil beam above the phantom shots directly to the small insert. Figure 4.2a is the result using the standard physics library and in Figure 4.2b the Penelope model with MI activated.

TABLE 4.3: Normalized values for elements in the central module at 80keV source photon energy.

Element	**Normalization (%)**					
	Air		**CAX**			
	$A7_{Air}$	$A8_{Air}$	$A5_{Cax}$	$A6_{Cax}$	$A7_{Cax}$	$A8_{Cax}$
401	2.036	1.969	98.81	83.16	2.011	1.638
402	2.030	1.948	100.6	85.65	2.042	1.668
403	2.022	1.917	100.6	88.22	2.033	1.691
404	1.997	1.908	99.24	90.36	1.996	1.724
405	1.993	1.900	100.2	93.08	1.998	1.759
406	2.030	1.921	100.6	95.97	2.043	1.844
407	1.954	1.837	100.3	97.92	1.960	1.799
408	2.035	1.942	100.5	100.4	2.045	1.950
409	2.032	1.928	100.0	100.0	2.032	1.928
410	1.953	1.861	100.3	98.01	1.958	1.824
411	1.965	1.861	100.3	95.53	1.971	1.778
412	1.936	1.823	100.6	93.40	1.947	1.703
413	1.978	1.850	100.4	90.70	1.986	1.678
414	1.968	1.884	100.6	88.43	1.981	1.666
415	2.021	1.912	100.4	85.57	2.029	1.636
416	2.031	1.924	98.83	83.11	2.007	1.599

Once verified that the change to the Penelope physics lists with MI incorporated is working properly, we can go back to and use the CT geometry. Another set of eight simulations was run to check the effect of the new physics library on the CT scanner, Table 4.4 shows the configuration used on each simulation. These simulations change the physics list from the standard library to the Penelope model with MI implementation. The energy used on the source is mono-energetic with a 12mm collimation, a single phantom diameter size without casing, and the septa structure.

Figure 4.3 is a comparison between the standard physics library against the Penelope with MI. An increase in signal is observed when using the Penelope with MI model. Detailed values for the central element are shown in Table 4.5

The results from simulations listed in Table 4.4 are shown in Figure 4.3, an increase in signal is observed for both energies, in Figure 3.4 for small scattering angles a reduction of intensity is observed when using the MI model, causing the less interaction occurs inside the phantom and increasing other signals.

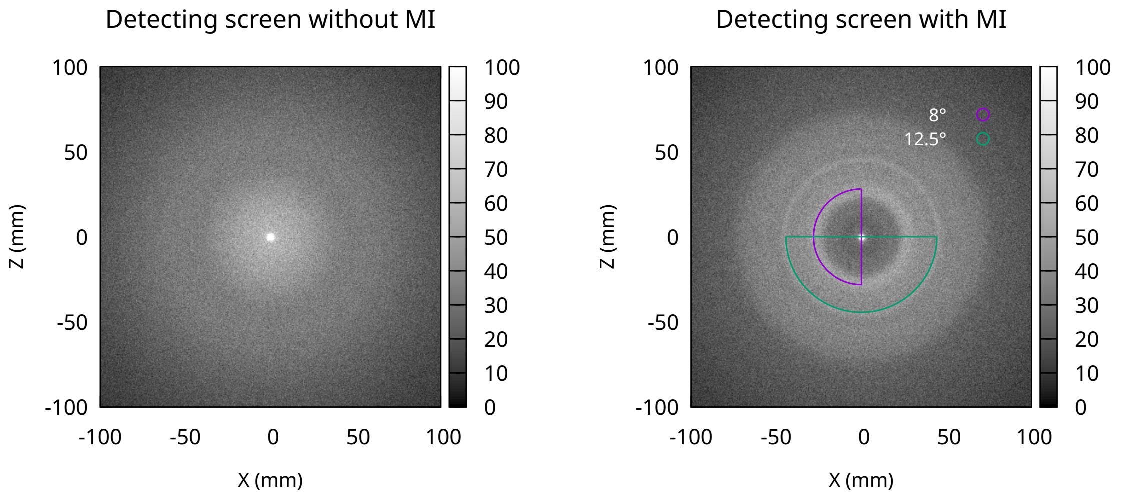

(A) Energy deposed (keV) on a detecting screen using Geant4's standard physics list.

(B) Energy deposed on a detecting screen using Penelope's physics list with MI.

FIGURE 4.2: Geant4 physics lists comparisons between the standard's library and Penelope with the MI model using a detecting screen.

TABLE 4.4: Simulations using the Penelope physics list with the MI model.

Simulation	**Energy (keV)**	**Phantom (mm)**	**Septa**
$B1$	45	no	no
$B2$			yes
$B3$		210	no
$B4$			yes
$B5$	80	no	no
$B6$			yes
$B7$		210	no
$B8$			yes

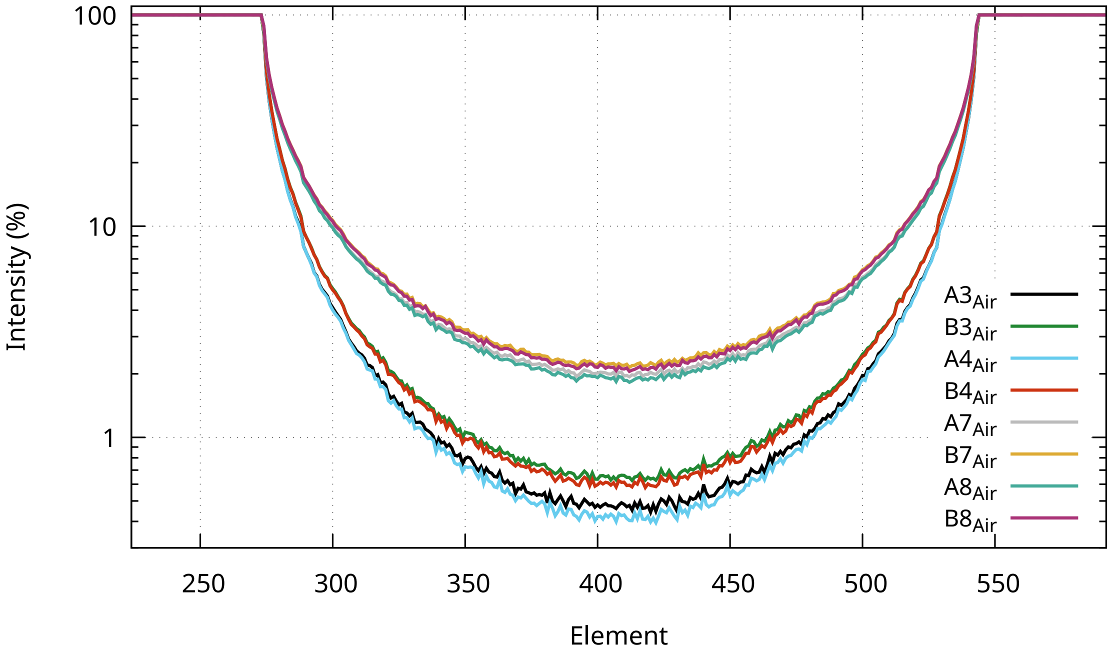

FIGURE 4.3: Comparison between the standard physics library (Ax_{Air}) vs the Penelope with MI (Bx_{Air}).

TABLE 4.5: Intensity comparison in the central element from results in Figure 4.3.

Element	**Signal intensity (%)**							
	$A3_{Air}$	$B3_{Air}$	$A4_{Air}$	$B4_{Air}$	$A7_{Air}$	$B7_{Air}$	$A8_{Air}$	$B8_{Air}$
409	0.490	0.662	0.426	0.612	2.032	2.196	1.928	2.115

The increased signal is more prominent near the central axis just below the phantom, to observe this with more detail Table 4.5 shows the results for the central element (409) from Figure 4.3.

4.3 X-ray spectrum

The next step is to replace the mono-energetic source with a tungsten energy spectrum, the energies to be used are $90kVp$ and $140kVp$ as shown in Figure 3.2. The photon energy will be slowly changed from one energy into three different ones with the same weight.

TABLE 4.6: Implementation results of tungsten spectra using Geant4's GPS utility in the central module. Simulations plot found in Figure 4.4

Simulation	**Energy**	**Phantom (mm)**	**Septa**
C1	35 - 45 - 55 keV	210	yes
C2	25 - 45 - 55 keV		
C3	35 - 45 - 65 keV		
C4	90 kVp		
C5	70 - 80 - 90 keV		
C6	50 - 80 - 90 keV		
C7	70 - 80 - 110 keV		
C8	140 kVp		

In Table 4.6 are found the source and geometry configurations of the eight simulations for the tungsten energy spectra using a 12mm collimation. The source changes from a mono-energetic photon beam to the full tungsten spectra at 90kVp and 140kVp. The simulations are made using the Penelope physics lists with the MI implementation.

Table 4.5 contains eight simulations for the implementation of the tungsten energetic spectrum, the idea is to slowly change the mono-energetic sources to the tungsten spectra while checking that the MC simulation is working correctly. The first step is to simulate three energies having the same intensity, with the mean energy being 40keV and 80keV respectively to the simulations. Next, we will reduce the low-energy photons or increase the high-energy photons to verify that the simulation reacts to this small change and finally simulate with the full tungsten spectra.

In the transition from a mono-energetic source to tungsten spectra, dashed lines are used for the high energies (80keV and 140kVp) and solid lines for the low energies (45keV and 90kVp). Simulations B4 and B8 are the mono-energetic ones (black lines) found in Table 4.4, the rest of the simulations are in Table 4.6, with simulations C4 and C8 using the complete tungsten spectrum (red lines).

In Figure 4.4 we can see the effect of changing the photon energy of the source, simulation B4 is 45keV mono-energetic, and simulation C1 is the same energy with two more energies close to this one, as a result, these simulations are almost identical. Simulation C2 picks the 35keV energy and reduces it to 25keV while simulation C3 increases the high energy from 55keV to 65keV, as expected, simulation C2 has less signal than B4 and C1, while simulation C3 has more signal. Overall when using the full 90kVp tungsten spectrum we obtain the highest signal.

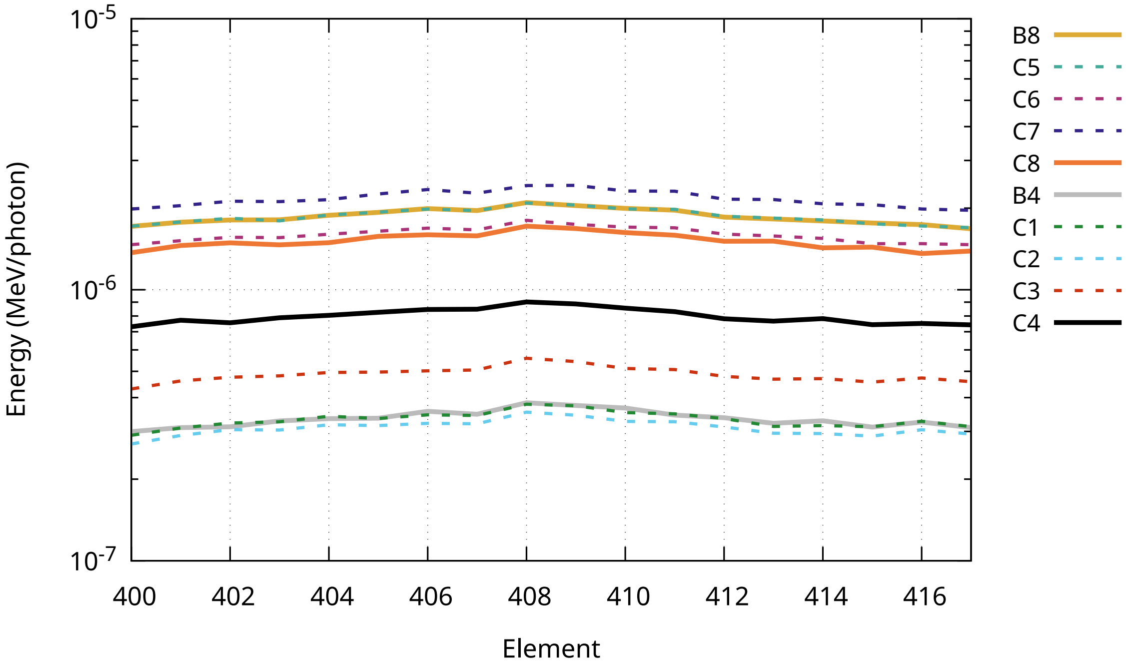

FIGURE 4.4: Implementation of tungsten spectra using Geant4's GPS utility. Simulations plot found in Table 4.6

We obtained a similar result for simulations B8, C5, C6 and C7, again, B8 and C5 are almost the same signals, C5 has less signal and C7 has the highest. The difference when using the 140kVp tungsten spectra over the 90kVp is that simulation C8 got less signal between the simulation group. This difference can be explained by looking at Figure 3.2 and observing that the area under the curve for the 90kVp is bigger after 45keV and smaller in the 140kVp before 80keV.

4.4 Scatter Signal Profiles

The last code implementation is to add the scatter signal algorithm shown in Figure 3.5 and compute the standard deviation and percentage error mentioned in Chapter 3. And, the phantom geometry changes to one with PMMA casing filled with water along with the 54mm with septa. After the implementations are done, 128 simulations will be run doing every possible combination shown in Tables 4.7, 4.8, 4.9 and 4.10.

In Figure 4.5 we are looking at the raw data of a $90kVp$ simulation, using a FOV of $600mm$, $24mm$ collimation, with the bowtie and septa present and a phantom diameter of $320mm$. As shown in Figure 3.5, the crosstalk signal from non-primary events, the septa signal, the base signal, and the air signal will be added up and shown as one result.

Signal profiles in Figure 4.5 are made using a $90kVp$ spectra, $600mm$ FOV, $24mm$ collimation, $320mm$ phantom diameter with bowtie and septa present. The total signal is the sum of all the profiles, Cross P. and Cross O. stand for the crosstalk signals the P. from primary events and O. from non-primary events.

$$T = P + P' + S + A + B + C + C' + D \tag{4.1}$$

Where:

- P: Is the primary signal.
- P': Is the scatter from the bowtie filter.
- S: Is the scatter from the phantom.
- A: Is the scatter from the air.
- B: Is the scatter from the photodiode base.
- C: Is the crosstalk signal from primary events.
- C': Is the crosstalk signal from non-primary events.
- D: Is the scatter from the septa structure.

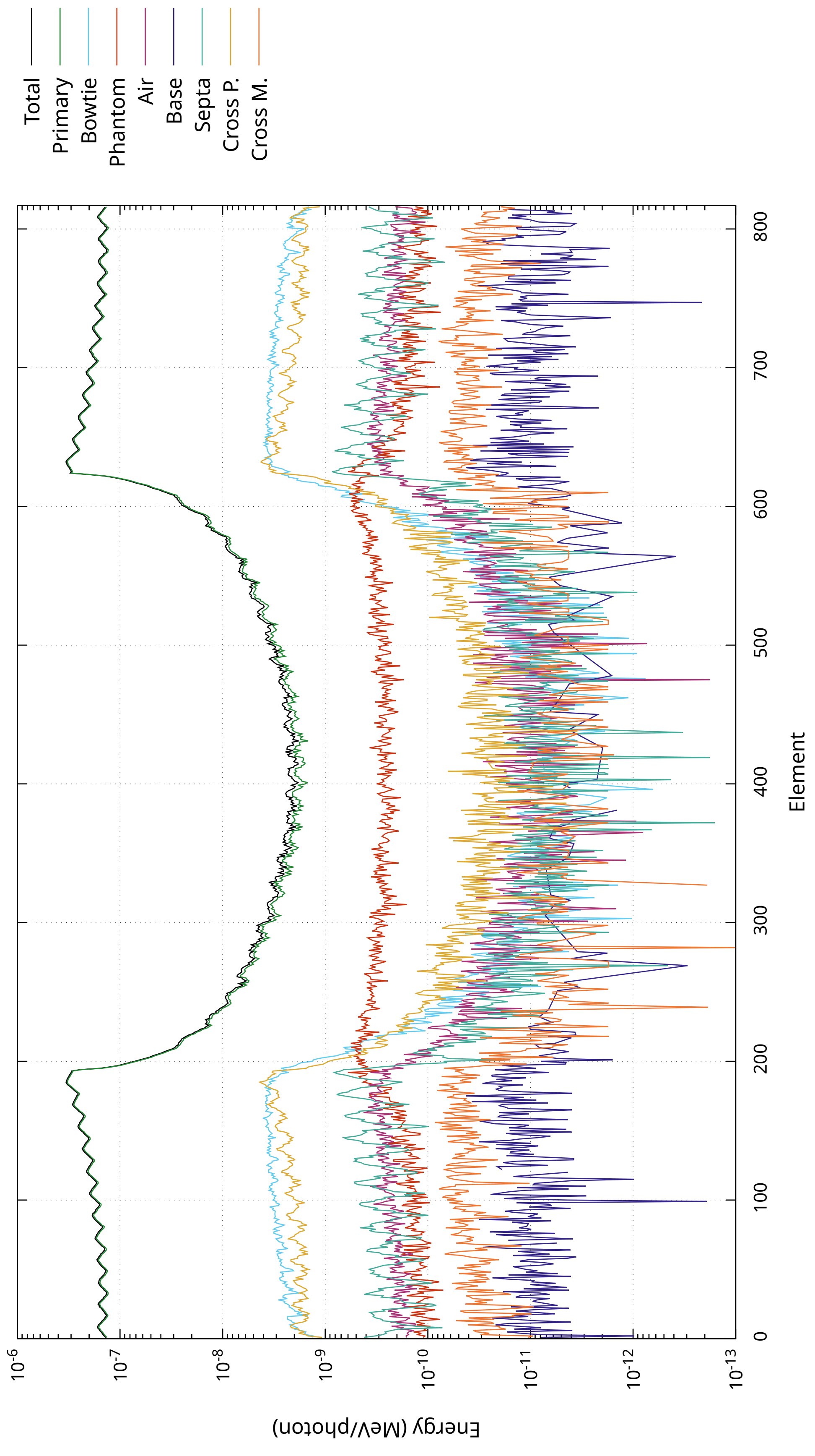

FIGURE 4.5: Raw data sample to visualize every signal profile in a simulation with all the scanner structures present, lowest source energy, highest collimation and biggest phantom.

To finalize this chapter, we show the mean energy, standard deviation, and percentage errors in the central element (409) for all the 128 simulations done in this project. Tables 4.7 and 4.8 contains these values for the $90kVp$ spectra energy and tables 4.9 and 4.10 for the $140kVp$ energy.

Looking at the mean energy deposed in Tables 4.7 to 4.10, a clear reduction in signal is observed when more structures of the scanner appear for each source energy, also with the presence of the phantom and the increase of their diameter and for higher collimation values. This reduction is caused due to the scanner structures that block or attenuate the photons, but in the case of the collimation, since all the simulations are made using $n = 10^{10}$ source particles, the signal is reduced because the same number of source photons are distributed in a higher surface.

A similar effect can be observed with the standard deviation, this increase can be caused by several effects, some of them thanks to the beam hardening, reducing the spectra energy of the photons that can reach the central element and also the septa structure, that blocks scattered photons coming from the scanner structure of the phantom.

For the percentage error we found the opposite effect, this one increases as the scanner structures of the phantom appear in the simulations. For the $90kVp$ energy we found an increase from 0.065% to 5.166% and for the $140kVp$ energy we found an increase from 0.067% to 3.972%. If we consider that a percentage error of less than 1% is acceptable, we can increase the number of photons for collimation $6, 12, 24mm$ with a phantom present, while some $3mm$ collimation simulation may not require such a large number of source photons.

TABLE 4.7: Standard deviation and percentage error for 90kVp (1/2).

Phantom (*mm*)	**Collimation** (*mm*)	**Bowtie**	**Septa**	**Energy** (*MeV / photon*)	**Standard Dev.** (*MeV / photon*)	**Error** (%)
no	3	no	no	1.308e-05	8.528e-04	0.065
			yes	1.284e-05	8.466e-04	0.066
		yes	no	1.200e-05	8.180e-04	0.068
			yes	1.178e-05	8.120e-04	0.069
	6	no	no	6.545e-06	6.033e-04	0.092
			yes	6.428e-06	5.989e-04	0.093
		yes	no	6.009e-06	5.789e-04	0.096
			yes	5.898e-06	5.746e-04	0.097
	12	no	no	3.274e-06	4.267e-04	0.130
			yes	3.214e-06	4.235e-04	0.132
		yes	no	3.008e-06	4.096e-04	0.136
			yes	2.950e-06	4.064e-04	0.138
	24	no	no	1.643e-06	3.023e-04	0.184
			yes	1.612e-06	2.999e-04	0.186
		yes	no	1.511e-06	2.903e-04	0.192
			yes	1.480e-06	2.878e-04	0.195
215.4	3	no	no	1.495e-07	9.492e-05	0.635
			yes	1.433e-07	9.333e-05	0.651
		yes	no	1.376e-07	9.116e-05	0.663
			yes	1.324e-07	8.976e-05	0.678
	6	no	no	7.628e-08	6.773e-05	0.888
			yes	7.180e-08	6.604e-05	0.920
		yes	no	7.028e-08	6.508e-05	0.926
			yes	6.627e-08	6.350e-05	0.958
	12	no	no	3.973e-08	4.876e-05	1.227
			yes	3.572e-08	4.659e-05	1.304
		yes	no	3.634e-08	4.669e-05	1.285
			yes	3.306e-08	4.483e-05	1.356
	24	no	no	2.164e-08	3.594e-05	1.661
			yes	1.798e-08	3.320e-05	1.847
		yes	no	1.960e-08	3.435e-05	1.752
			yes	1.659e-08	3.188e-05	1.922

TABLE 4.8: Standard deviation and percentage error for 90kVp (2/2).

Phantom (*mm*)	**Collimation** (*mm*)	**Bowtie**	**Septa**	**Energy** (*MeV / photon*)	**Standard Dev.** (*MeV / photon*)	**Error** (%)
270	3	no	no	5.078e-08	5.567e-05	1.096
			yes	4.760e-08	5.421e-05	1.139
		yes	no	4.664e-08	5.342e-05	1.145
			yes	4.414e-08	5.225e-05	1.184
	6	no	no	2.635e-08	3.998e-05	1.517
			yes	2.388e-08	3.836e-05	1.607
		yes	no	2.386e-08	3.810e-05	1.597
			yes	2.197e-08	3.683e-05	1.676
	12	no	no	1.434e-08	2.923e-05	2.039
			yes	1.195e-08	2.707e-05	2.265
		yes	no	1.266e-08	2.758e-05	2.178
			yes	1.095e-08	2.592e-05	2.366
	24	no	no	8.260e-09	2.219e-05	2.686
			yes	6.139e-09	1.952e-05	3.179
		yes	no	7.214e-09	2.081e-05	2.885
			yes	5.637e-09	1.873e-05	3.322
320	3	no	no	1.941e-08	3.459e-05	1.782
			yes	1.759e-08	3.322e-05	1.888
		yes	no	1.735e-08	3.281e-05	1.891
			yes	1.618e-08	3.189e-05	1.971
	6	no	no	1.004e-08	2.476e-05	2.465
			yes	8.538e-09	2.312e-05	2.708
		yes	no	8.740e-09	2.320e-05	2.654
			yes	7.791e-09	2.213e-05	2.841
	12	no	no	5.711e-09	1.849e-05	3.238
			yes	4.341e-09	1.643e-05	3.785
		yes	no	4.804e-09	1.705e-05	3.549
			yes	3.882e-09	1.556e-05	4.007
	24	no	no	3.605e-09	1.456e-05	4.038
			yes	2.345e-09	1.216e-05	5.184
		yes	no	2.842e-09	1.309e-05	4.604
			yes	2.113e-09	1.154e-05	5.460

TABLE 4.9: Standard deviation and percentage error for 140kVp (1/2).

Phantom (*mm*)	**Collimation** (*mm*)	**Bowtie**	**Septa**	**Energy** (*MeV / photon*)	**Standard Dev.** (*MeV / photon*)	**Error** (%)
no	3	no	no	1.582e-05	1.071e-03	0.068
			yes	1.554e-05	1.065e-03	0.069
		yes	no	1.467e-05	1.033e-03	0.070
			yes	1.441e-05	1.028e-03	0.071
	6	no	no	7.919e-06	7.574e-04	0.096
			yes	7.783e-06	7.539e-04	0.097
		yes	no	7.349e-06	7.310e-04	0.099
			yes	7.219e-06	7.275e-04	0.101
	12	no	no	3.958e-06	5.355e-04	0.135
			yes	3.892e-06	5.332e-04	0.137
		yes	no	3.676e-06	5.171e-04	0.141
			yes	3.610e-06	5.146e-04	0.143
	24	no	no	1.985e-06	3.793e-04	0.191
			yes	1.952e-06	3.776e-04	0.193
		yes	no	1.846e-06	3.664e-04	0.198
			yes	1.812e-06	3.646e-04	0.201
215.4	3	no	no	2.829e-07	1.527e-04	0.540
			yes	2.733e-07	1.511e-04	0.553
		yes	no	2.627e-07	1.475e-04	0.561
			yes	2.546e-07	1.460e-04	0.574
	6	no	no	1.447e-07	1.091e-04	0.754
			yes	1.379e-07	1.073e-04	0.778
		yes	no	1.340e-07	1.052e-04	0.785
			yes	1.286e-07	1.037e-04	0.807
	12	no	no	7.458e-08	7.811e-05	1.047
			yes	6.903e-08	7.603e-05	1.101
		yes	no	6.894e-08	7.526e-05	1.092
			yes	6.421e-08	7.340e-05	1.143
	24	no	no	4.011e-08	5.699e-05	1.421
			yes	3.485e-08	5.402e-05	1.550
		yes	no	3.688e-08	5.480e-05	1.486
			yes	3.227e-08	5.205e-05	1.613

TABLE 4.10: Standard deviation and percentage error for 140kVp (2/2).

Phantom (*mm*)	**Collimation** (*mm*)	**Bowtie**	**Septa**	**Energy** (*MeV / photon*)	**Standard Dev.** (*MeV / photon*)	**Error** (%)
270	3	no	no	1.071e-07	9.504e-05	0.887
			yes	1.020e-07	9.351e-05	0.917
		yes	no	9.940e-08	9.171e-05	0.923
			yes	9.546e-08	9.053e-05	0.948
	6	no	no	5.531e-08	6.807e-05	1.231
			yes	5.128e-08	6.633e-05	1.293
		yes	no	5.117e-08	6.563e-05	1.283
			yes	4.806e-08	6.424e-05	1.337
	12	no	no	2.921e-08	4.930e-05	1.688
			yes	2.586e-08	4.719e-05	1.825
		yes	no	2.734e-08	4.784e-05	1.750
			yes	2.429e-08	4.571e-05	1.882
	24	no	no	1.689e-08	3.715e-05	2.199
			yes	1.357e-08	3.429e-05	2.526
		yes	no	1.537e-08	3.569e-05	2.323
			yes	1.275e-08	3.324e-05	2.608
320	3	no	no	4.469e-08	6.191e-05	1.385
			yes	4.174e-08	6.048e-05	1.449
		yes	no	4.103e-08	5.946e-05	1.449
			yes	3.875e-08	5.836e-05	1.506
	6	no	no	2.362e-08	4.479e-05	1.896
			yes	2.108e-08	4.299e-05	2.039
		yes	no	2.124e-08	4.267e-05	2.009
			yes	1.952e-08	4.148e-05	2.125
	12	no	no	1.314e-08	3.304e-05	2.514
			yes	1.071e-08	3.073e-05	2.868
		yes	no	1.155e-08	3.128e-05	2.708
			yes	9.957e-09	2.970e-05	2.983
	24	no	no	8.166e-09	2.601e-05	3.186
			yes	5.965e-09	2.312e-05	3.876
		yes	no	7.061e-09	2.452e-05	3.473
			yes	5.547e-09	2.231e-05	4.021

Chapter 5

Results

This chapter presents all the results from the simulations shown in Tables 4.7, 4.8, 4.9 and 4.10 using different normalizations to observe different effects and details in the data. The normalization technique will be explained in each section and subsections of the chapter. The chapter is divided into two main sections, the first one is called signal profiles and the idea is to show the small change in signal when removing scanner structures or placing different phantom sizes at the isocenter, and the second part shows how the scatter from the phantom is affected by the bowtie and septa structures.

5.1 Signal profiles

This section contains several plots showing the different signal contributions for all phantom diameter sizes (d), source energies (E) and, source collimations (c). In the plots, there will be small signal contributions difficult to appreciate when looking in conjunction with the total or primary signals, sometimes not even a logarithmic scale can help differentiate these small details, to overcome this issue in Figure 3.5 there is a flow chart where the air, base, and non-primary-crosstalk (NPC) are combined conforming the mixed signal, following Equation 5.1, this because they are some of the smallest contributions generated in the simulations.

$$M = A + B + C' \tag{5.1}$$

Where:

- M: Is the sum of air, base and NPC signals.
- A: Is the scatter from the air.
- B: Is the scatter from the base.
- C': Is the crosstalk signal from non-primary events.

The total signal received in the detecting elements is the sum of the primary signal, the scatter from the phantom and all the scatter volumes present in the simulation, Equation 5.2 shows each one of these contributions.

$$T = P + P' + S + C + D + M \tag{5.2}$$

Where:

- T: Is the total signal.
- P: Is the primary signal.
- P′: Is the scatter from the bowtie filter.
- S: Is the scatter from the phantom.
- C: Is the crosstalk signal from primary events.
- D: Is the scatter from the septa.
- M: is the mixed contribution defined in Equation 5.1

The normalization of the data in this section is known as an air scan, which is a scan of the air volume in between the X-ray source and the detecting elements with the bowtie filter and the septa structures in place, a total of eight simulations are used for the data normalization show in Table 5.1. Equation 5.4 shows how the normalization is done for any simulation.

The scatter-to-primary ratio (SPR) is calculated using Equation 5.3 where the contribution of the bowtie filter is considered part of the primary signal. This value is given only at the central element (409) in which case is the same as a normalized scatter profile (NSP). Complete plots of NSP are found in Appendix A and for SPR in Appendix B.

$$SPR_{409} = 100 * \frac{S_{409}}{P_{409} + P'_{409}} \tag{5.3}$$

Where:

- SPR: Is the scatter-to-primary ratio in element 409.
- P: Is the primary signal in element 409.
- P′: Is the scatter from the bowtie filter in element 409.
- S: Is the scatter from the phantom in element 409.

TABLE 5.1: Set of simulations used for data normalization in the Signal Profiles chapter section.

Simulation	**Phantom**	**Bowtie**	**Septa**	**Energy (kVp)**	**Collimation (mm)**
$F1$	no	yes	yes	$E = 90$	$c = 3$
$F2$					$c = 6$
$F3$					$c = 12$
$F4$					$c = 24$
$F5$				$E = 140$	$c = 3$
$F6$					$c = 6$
$F7$					$c = 12$
$F8$					$c = 24$

$$R_i^{ec} = 100 * \frac{X_i^{ec}}{F_i^{ec}} \tag{5.4}$$

Where:

- R_i^{ec}: Is the resulting intensity in an element i for a simulation with a specific source energy E and collimation c.
- X_i^{ec}: Is the signal in element i of the simulation of interest with the same specific source energy E and collimation c.
- F_i^{ec}: Is the normalization signal data from table 5.1, in an element i matching the same source energy E and collimation c.

The air-scan normalization is done with the bowtie filter and the septa structures in place, this type of normalization is useful from a more clinical perspective since the air scan will have 100% of the intensity in every element re-scaling the bowtie and septa attenuation over the detecting elements.

5.1.1 Signal profiles without phantom

Phantom-less signal profiles allow us to identify the small contribution of the air and scanner structures, such as back-scatter from the photodiode base, the bowtie filter, or the crosstalk signals, by taking advantage of the high-intensity signal profiles in the whole detector structure with less than 1% error as shown in Tables 4.7 and 4.9 in the central element.

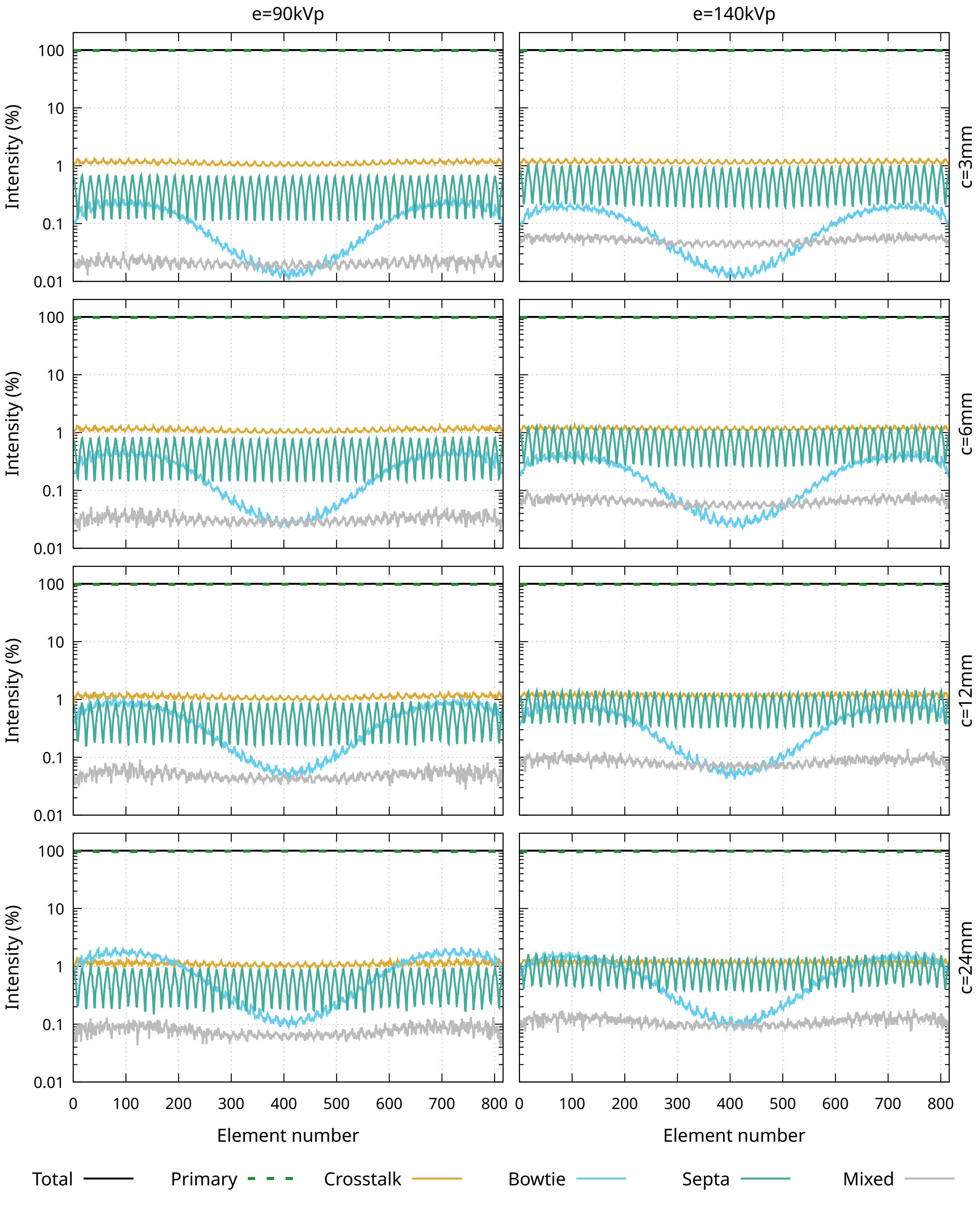

FIGURE 5.1: Signal profiles with bowtie, no phantom, with septa. Central module signal detail in Figure 5.2.

The first simulation to show has all the CT scanner structures present and represents the most realistic representation of an air scan, the data used for the air scan is the same hence all the values of the total signal are equal to 100% for all the source energies and collimations, as we can see in Figure 5.1.

Signal profiles in Figure 5.1 are made using both $90kVp$ and $140kVp$ tungsten spectra energies (E) arranged by columns, $3mm$, $6mm$, $12mm$ and $24mm$ collimations c (see Equation 3.2) displayed by row, and a $g = 600mm$ FOV (see Equation 3.1), with the bowtie and septa structures present. The total signal is the sum of all the profiles, the crosstalk signal is only from primary events, the bowtie is the scatter coming from the filter, the septa signal is the scatter from the grid and, the mixed signal is the base, air and NPC signals as expressed in Equation 5.1. The primary signal is flat and close to the total signal.

The crosstalk signal shape in Figure 5.1 is flat across the detecting structure with about the same intensity for all the source energies and collimations staying between 1% and 2% of intensity when looking at the sides of the detecting structure, far from the center, the signal at collimations higher than $c = 6mm$ starts to look noisy. On a more local observation, the shape of the crosstalk signal is a small mountain at the center of each module of the detecting structure.

The septa signal in Figure 5.1 is flat along the detecting structure, this signal is affected by the source energy, where at $E = 90kVp$ the size of the spikes are taller and less intense than for the $E = 140kVp$ when looking at the same c source collimation value, also, when increasing the source collimation it is possible to observe an increase in signal intensity. This increase in signal is caused by more septa volume being under the source fan beam at the different source collimation values. The large spikes generated at the edge of each module in the signal are due to the un-focused septum cutting more source photons and generating more scatter.

The only signal that is not flat in Figure 5.1 across the detecting structure is the bowtie signal. This signal in the middle of the detecting structure is the same between source energies when looking at the same collimation number c, at the sides of the structure, close to elements 100 and 700 the intensity increases at a point where at $c = 24mm$ value it surpasses the crosstalk signal, also for the $E = 90kVp$ the intensity is higher.

The mixed signal is also mainly flat across the detecting structure in Figure 5.1, with a slight increase of intensity at the sides near elements 100 and 700, where the signal becomes noisy. The noise and intensity vary with the source energy and collimation

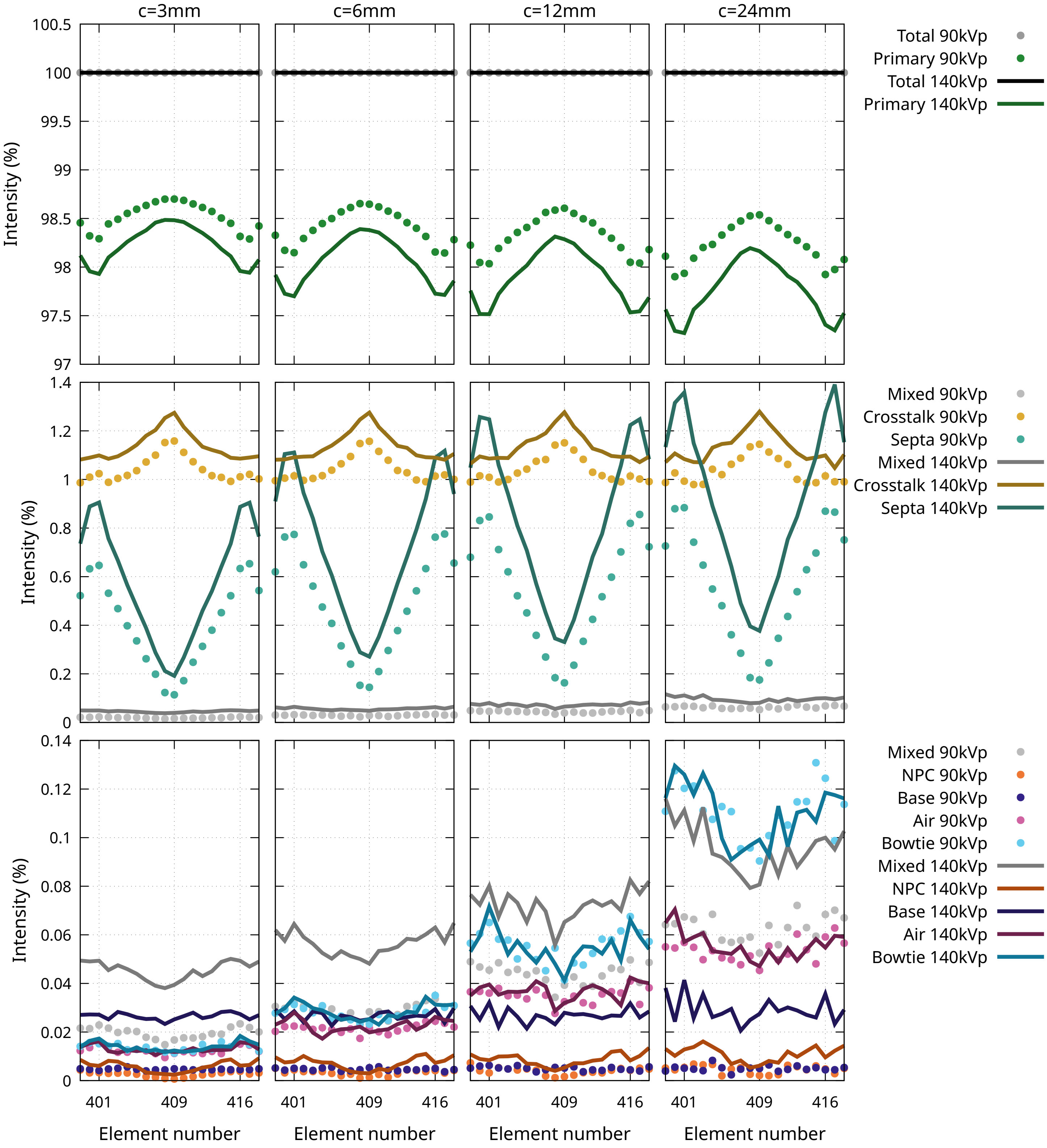

FIGURE 5.2: Signal profiles with bowtie, no phantom, with septa, in the central module.

number, at $c = 3mm$ collimation and $E = 140kVp$ the shape of the mixed signal is recognizable in the center of the structure, where we can see small valleys being created at the center of the modules when changing to $E = 90kVp$ energy the signal has a lower intensity. The change in intensity at $E = 140kVp$ source energy is slower than for the $E = 90kVp$ energy when increasing the collimation c at the point that when $c = 24mm$ the mixed signal difference between energies is lower.

Signal profiles in Figure 5.2 are in the central module for both $90kVp$ and $140kVp$ tungsten spectra energies E, $3mm$, $6mm$, $12mm$ and $24mm$ collimations c (see Equation 3.2) displayed by columns and a $g = 600mm$ FOV (see Equation 3.1), with the bowtie and septa present. The total signal is the sum of all the profiles, the crosstalk signal is only from primary events, the bowtie is the scatter coming from the filter, the septa signal is the scatter coming from the grid and, the mixed signal is the base, air, and NPC signals.

As mentioned earlier, it is hard to observe small details in the signal profiles when looking at the whole detecting structure while using a logarithmic scale, Figure 5.2 solves this issue by displaying three different energy ranges and using a liner scale. The total signal for both energies E and collimations c is always 100% since in Equation 5.4 we are dividing by the same number.

The primary signal in Figure 5.2 is more intense when $E = 90kVp$ than $E = 140kVp$ across all the collimations c, but with the collimation number this signal decreases about 0.2% at $E = 90kVp$ and 0.3% at $E = 140kVp$ in element 409, element 401 decreases more with 0.4% and 0.6% respectively.

The crosstalk signal has the shape of a small peak mountain and seems to be constant across the different collimations c, the intensity at element 409 using $E = 90kVp$ is 1.16% and at $E = 140kVp$ is 1.27% while at element 401 we have 1.02% and 1.10% respectively. As already may be seen, the crosstalk signal at $E = 140kVp$ is higher than at $E = 90kVp$.

The scatter from the septa structure in Figure 5.2 appears to be higher at the side of the module and more intense when $E = 140kVp$ in every collimation c, both signals increase c where at $E = 90kVp$ and $c = 3mm$ to $c = 24mm$ the signal goes from 0.12% to 0.18%, at $E = 140kVp$ the signals are 0.19% to 0.37% in element 409, element 401 will have 0.65% 0.88% at $90kVp$ and 0.91% 1.36% at $E = 140kVp$. It is important to observe that the septa signal at the sides of a module has an important contribution, especially when the collimation is higher than $3mm$ for $E = 140kVp$ where the septa signal surpasses the crosstalk.

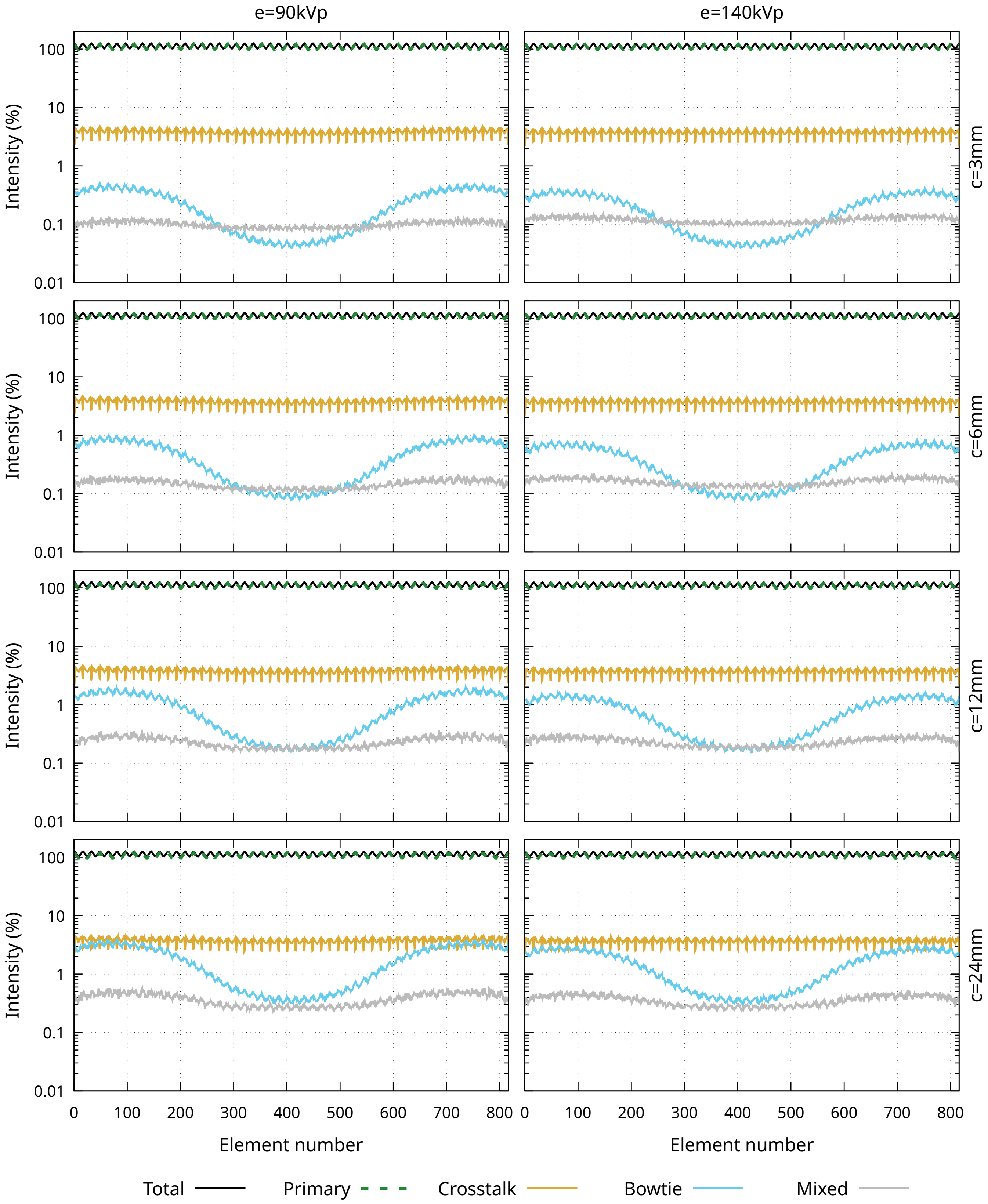

FIGURE 5.3: Signal profiles with bowtie, no phantom, no septa. Central module signal detail in Figure 5.4.

The bowtie signal contribution is low in the central module, as seen in Figure 5.2, the intensity is about the same for both energies E, but it increases with the collimation number for $c = 3mm$ and $c = 6mm$ the shape of the signal is mostly flat, at $c = 12mm$ and $c = 24mm$ the shapes resemble a small valley, the intensity value at element 409 are 0.012%, 0.023%, 0.041% and 0.090% respectively, which seems to duplicate the signal with ever c increase.

The mixed signal is flat across the module in Figure 5.2, let's remember that this signal is the sum of the NPC, base and air signals as expressed in Equation 5.1, it is important to note that this signal accounts for up to 0.01% of the total signal at $E = 140kVp$ and $c = 24mm$. The air signal is the biggest contributor to the mixed signal and the one responsible for the intensity increase with the collimation number. The base signal, which is the back-scatter from the photodiode base is more than double at $E = 140kVp$ when compared to $E = 90kVp$.

Signal profiles in Figure 5.3 are made using both $90kVp$ and $140kVp$ tungsten spectra energies (E) arranged by columns, $3mm$, $6mm$, $12mm$ and $24mm$ collimations c (see Equation 3.2) displayed by row, and a $g = 600mm$ FOV (see Equation 3.1), with the bowtie filter and without the septa structure. The total signal is the sum of all the profiles, the crosstalk signal is only from primary events, the bowtie is the scatter coming from the filter, the septa signal is missing and, the mixed signal is the base, air and NPC signals as expressed in Equation 5.1.

This will have the bowtie filter in place but not the septa structure, when removing a scanner structure that affects directly the primary signal in the detecting elements, the expected result will be an increase in signal, this increase above the 100% intensity can be somehow interpreted as the attenuation intensity of the removed structure. In Figure 5.3 we can see that the total signal now has the form of mountain shapes in between modules for all spectra energies E and collimations c when comparing to Figure 5.1. The primary signal is dominant in the total signal and behaves similarly to it.

The crosstalk signal shape in Figure 5.3 forms an up-directed arrow in between the modules when looking at Figure 5.3, the intensity across the detecting structure is flat along with the primary signal, since the crosstalk is generated from primary photons the intensity of the signal does not seem to change for the different collimations c and, the signal when changing the source energy E seems to equalize the signal.

Figure 5.3 also shows the bowtie signal across the whole elements in the detecting

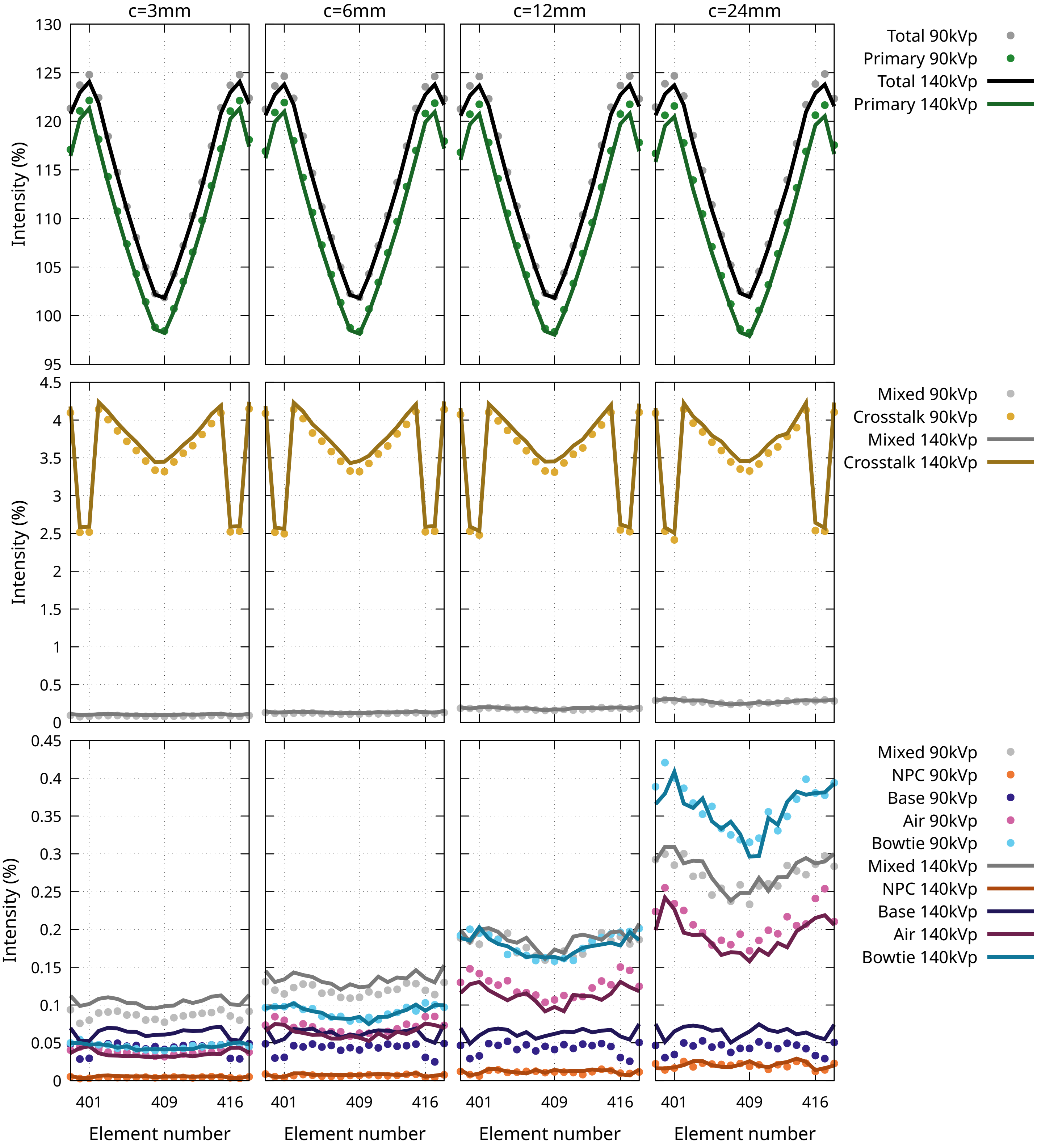

FIGURE 5.4: Signal profiles with bowtie, no phantom, no septa, in the central module.

structure, the shape of this signal resembles two mountains with a valley in the middle of the structure similar to Figure 5.1 but with less intensity, and the bowtie signal increases with the collimation number for the two source energies E, at $c = 24mm$ collimation the bowtie filter reaches the crosstalk curve. At $E = 90kvP$ energy the filter generates more intensity at the sides of the detecting structure while in the middle the intensity appears to be the same as with $140kVp$. This difference in intensity is caused by the photon source passing through thicker parts of the bowtie filter generating more scatter while in the middle of the filter, the crossed bowtie material is thin enough to observe the difference by source energy.

The shape of the mixed signal in Figure 5.3 is almost flat across the detecting structure, with small elevations at the side elements mimicking the shape of the bowtie signal, the signal increases with the source collimation c as seen previously at both source energies E, being the highest contribution at $c = 24mm$ collimation also, the intensity at the center of the detecting structure appears to be the same. Meanwhile, at a $c = 3mm$ collimation, the intensity is higher at $E = 140kVp$ than $E = 90kVp$.

Signal profiles in Figure 5.4 are in the central module for both $90kVp$ and $140kVp$ tungsten spectra energies E, $3mm$, $6mm$, $12mm$ and $24mm$ collimations c (see Equation 3.2) displayed by columns and a $g = 600mm$ FOV (see Equation 3.1), with the bowtie in place and without the septa structure. The total signal is the sum of all the profiles, the crosstalk signal is only from primary events, the bowtie is the scatter coming from the filter, the septa signal is missing and, the mixed signal is the base, air, and NPC signals.

Following the same format as the previous figures, Figure 5.4 shows the deposed signals in the central module using a linear scale, the total signal using both source energies E and collimations c is about the same but for the first and last element in the module, where at the $E = 90kVp$ the intensity is higher. There is a small increase in the intensity of the total signal with the collimation number, at $c = 3mm$ we have 101.86% and 101.82% at $E = 90kVp$ and $E = 140kVp$ respectively, and at $c = 24mm$ 102.15% and $101, 91\%$. The primary signal follows the shape of the total signal as expected in this case with a primary-to-total ratio of 0.9663 at $E = 90kVp$ energy and 0.9647 at the $E = 140kVp$ at $c = 3mm$ source collimation.

The difference in primary signal between elements 401 and 409 is about 23% which is highly related to septa attenuation by the unfocused grid at the external detecting elements of a module, this percentage is close to one expressed in Table 3.2 where up to an 18% of the top area of an element is blocked by the septum. The total signal in element 409 is close to 1.9% above the 100% intensity that is close to the crosstalk reduction when

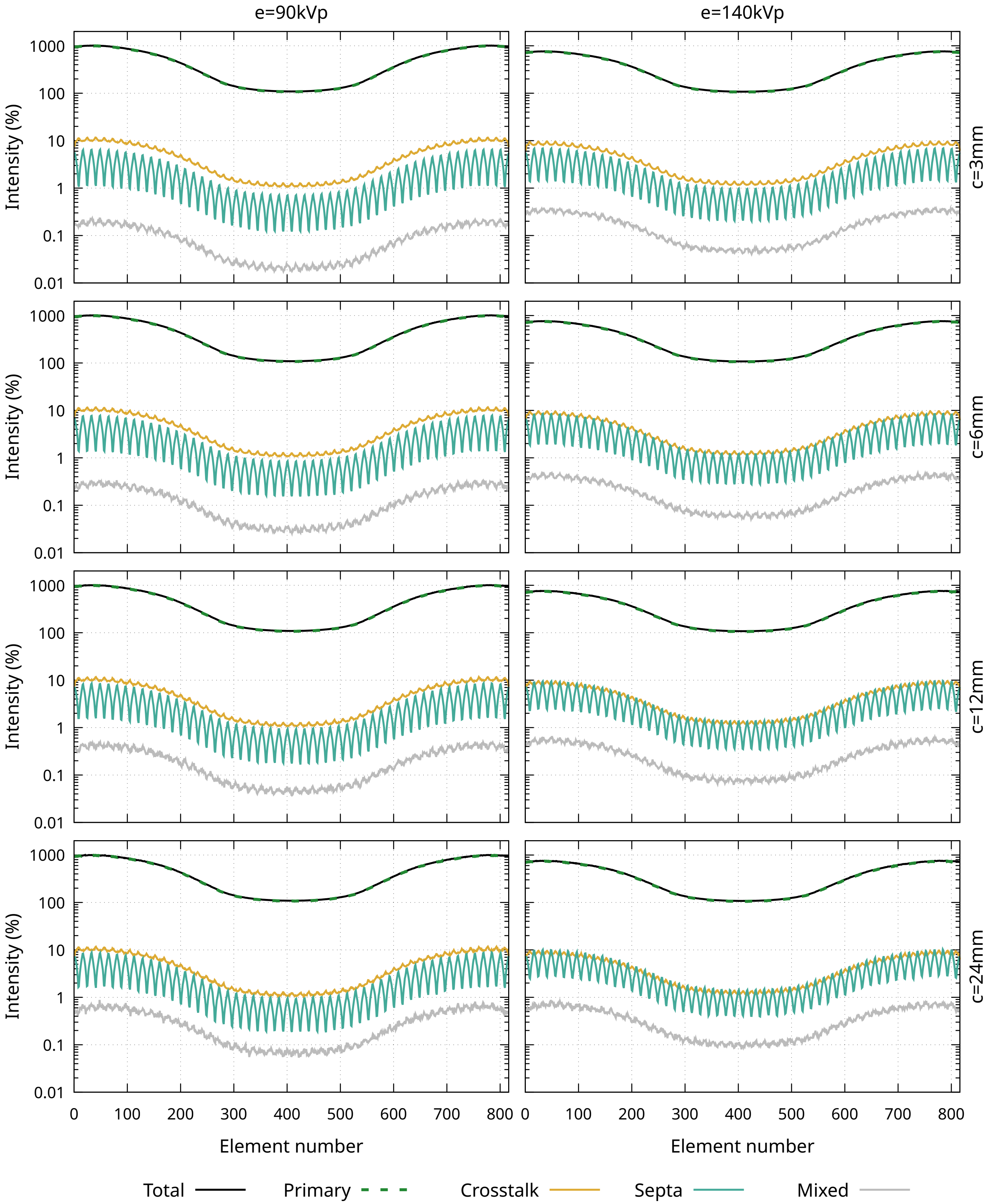

FIGURE 5.5: Signal profiles with no bowtie, no phantom, with septa. Central module signal detail in Figure 5.6.

the septa are present.

The crosstalk signal in Figure 5.4 has a different curve shape than in Figure 5.2 taking the form of a capital "m" and much more intensity, the signal does not seem to be affected by the collimation c and is a bit lower at $E = 90kVp$. The crosstalk-to-total ratio at $E = 90kVp$ and $c = 3mm$ collimation is 0.033 and at $E = 140kVp$ is 0.034 in element 409.

The bowtie signal in the central module is low compared to the total signal in Figure 5.4 the signal increases with the collimation number where at $c = 3mm$ and $c = 6mm$ source collimations the bowtie-to-total ratios are 0.0004 and 0.0008 respectively with a difference of more than three orders of magnitude, at $12mm$ collimation the ratio is 0.0016 matching the mixed component and finally for the $24mm$ collimation the ratio is 0.003 which still has a very low contribution in the total signal. Also, this signal seems to be unaffected by the source energy E mainly because high-energy photons will not likely interact with the Teflon material.

The mixed signal in Figure 5.4 as in is about the same in shape as in Figure 5.2 but with more intensity, the mixed-to-primary ratios for the $c = 3mm$, $c = 6mm$, $c = 12mm$ and $c = 24mm$ at $E = 90kVp$ source collimations and energy in the central element are 0.0008, 0.0011, 0.0016 and 0.0023 respectively and, for the $E = 140kVp$ 0.0010, 0.0012, 0.0017 and 0.0024. The small difference may be explained by the base scatter generating more signal at $E = 140kVp$ source energy and more air scatter at $E = 90kVp$.

The bowtie filter's purpose is to equalize the signal received in the detecting structure when a phantom is present, one of the most important properties of its signal is that the scatter generated can be considered part of the primary signal since it is placed far away from the detecting elements near the photon source. When looking at the raw data in Figure 4.5 we can see that before element 200 and after element 600 the signal is highly attenuated by this structure.

Signal profiles in Figure 5.5 are made using both $90kVp$ and $140kVp$ tungsten spectra energies (E) arranged by columns, $3mm$, $6mm$, $12mm$ and $24mm$ collimations c (see Equation 3.2) displayed by row, and a $g = 600mm$ FOV (see Equation 3.1), without the bowtie filter and with the septa structure. The total signal is the sum of all the profiles, the crosstalk signal is only from primary events, the bowtie signal is missing, the septa signal is the scatter coming from the grid and, the mixed signal is the base, air and NPC signals as expressed in Equation 5.1.

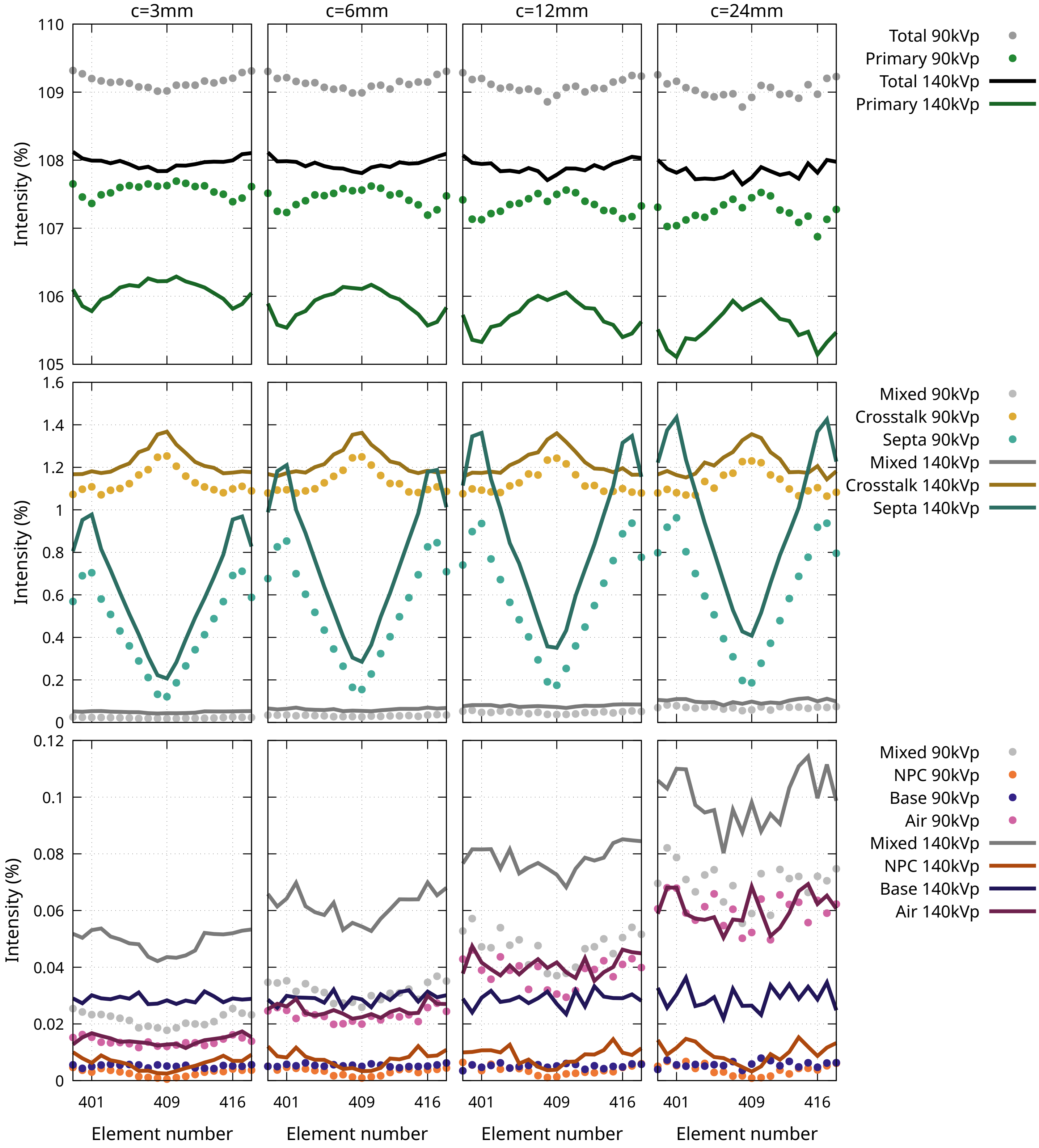

FIGURE 5.6: Signal profiles with no bowtie, no phantom, with septa, in the central module.

In Figure 5.5 the total signal across the whole detecting structure widely changes from close to the 100% intensity at the center of the detecting structure and up to 1000% at the sides, at $E = 90kVp$ the intensity is higher than at $E = 140kVp$. The local valleys created by the septa structure attenuating the fan-beam are now missing resulting in a smoother signal. This change in signal can be interpreted as the attenuation of the bowtie filter.

The crosstalk signal shape across the detecting structure changes and goes along with the shape of the primary signal since is generated from primary events in Figure 5.5, the local shape on each module reverts to the previously seen small mountain at the center of the modules and the intensity is also close to the one seen in Figure 5.1 since the septs is blocking most of the crosstalk and the bowtie filter is not thick at the center. The overall intensity of the crosstalk is the same at any energy E and collimation c.

The septa signal is back in Figure 5.5 and just like the crosstalk signal it follows the shape of the primary signal across the detecting structure, the intensity of the signal does increase with the source collimation c, for example, when at $E = 90kVp$ energy the septa signal increases from $c = 3mm$ to $c = 24mm$ collimations where the curve starts touching the crosstalk signal, at $140kVp$ energy the septa signal is already touching the crosstalk signal at $c = 6mm$.

The mixed signal in Figure 5.5 as seen previously is the contribution of the air, base, and NPC signal, its shape changes to one similar to the crosstalk or primary signals, now that more fluence is present in the air by removing the bowtie filter, the scatter coming from the air, which was the highest contributor in this signal, is now higher than in Figure 5.5. The same behavior is observed, the signal increases with the collimation and at $E = 140kVp$ in $c = 3mm$, at $c = 24mm$ they are about the same.

Signal profiles in Figure 5.6 are in the central module for both $90kVp$ and $140kVp$ tungsten spectra energies E, $3mm$, $6mm$, $12mm$ and $24mm$ collimations c (see Equation 3.2) displayed by columns and a $g = 600mm$ FOV (see Equation 3.1), without the bowtie filter in place and with the septa structure. The total signal is the sum of all the profiles, the crosstalk signal is only from primary events, the bowtie signal is missing, the septa signal is the scatter from the grid and, the mixed signal is the base, air, and NPC signals. Now that the effects of the septa structure are normalized we can see that the attenuation of the bowtie filter in the central element is close to 9% for the $90kVp$ energy and by about 8% for the $140kVp$.

The primary signal in Figure 5.6 flattens with the use of the septa structure for both

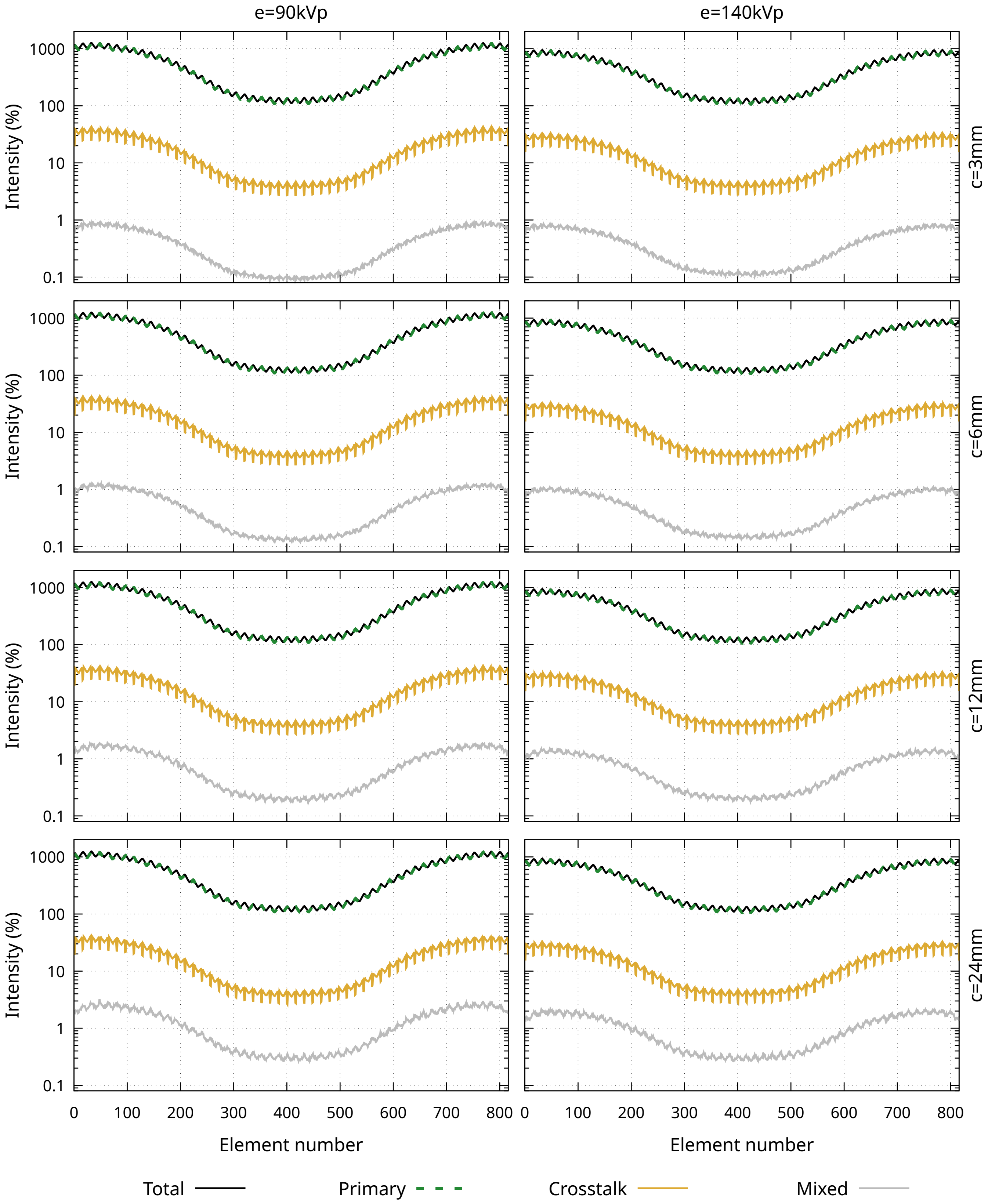

FIGURE 5.7: Signal profiles with no bowtie, no phantom and no septa. Central module signal detail in Figure 5.8.

of the source energies, taking the shape of a dome and breaking the similarity link with the total signal observed in previous figures, also a decrease in the primary signal is observed with the source collimation value, at $E = 90kVp$ source energy and $c = 3mm$ collimation the total to primary ratio is 0.9872 and for the $c = 24mm$ collimation is 0.9865, at $E = 140kVp$ the same values are 0.9850 and 0.9827.

The crosstalk signal shape also changes with the presence of the septa in Figure 5.6, from the shape of a capital "m" to a small hill in the middle of the module, here part of the primary signal is blocked by the septa as we move away from the center to the side of a module, hence less crosstalk will be generated. The septums in between the detecting elements block most of the signal reducing its intensity, the crosstalk-to-total signal ratio in the central element at $E = 90kVp$ and $c = 3mm$ source energy and collimation is 0.01150 and at $c = 24mm$ collimation is 0.01129 showing a small decrease proportional to the primary signal, at $140kVp$ the same corresponding values for $c = 3mm$ and $c = 24mm$ collimations are 0.01268 and 0.01258.

The septa signal generates a depth valley in the middle of the module in Figure 5.6, as discussed previously, the farther from the center of a module the more source photons are blocked by the septum and more scatter is generated from the septa. The septa-to-total signal ratio at $E = 90kVp$ source energy using the $c = 3mm$ collimation in the central element is 0.001110 and in element 401 is 0.006448, at $c = 24mm$ collimation the ratios are 0.001711 and 0.008818 respectively. When using $E = 140kVp$ energy the values are 0.001916 and 0.009055 for the $c = 3mm$ collimation and 0.003784 and 0.01331 at $c = 24mm$. It is important to notice that the septa signal has an important contribution at the side of the modules and that from $E = 140kVp$ energy at $c = 6mm$ collimation, it surpasses the crosstalk signal.

The mixed signal whose higher contribution is the scatter coming from the air in Figure 5.6 has a mixed-to-total ratio at $E = 140kVp$ source energy with and collimation $c = 24mm$ of 0.000910 with more than three orders of magnitude.

Signal profiles in Figure 5.7 are made using both $90kVp$ and $140kVp$ tungsten spectra energies (E) arranged by columns, $3mm$, $6mm$, $12mm$ and $24mm$ collimations c (see Equation 3.2) displayed by row, and a $g = 600mm$ FOV (see Equation 3.1), without the bowtie filter and the septa structure. The total signal is the sum of all the profiles, the crosstalk signal is only from primary events, the bowtie signal is missing, the septa signal is the scatter coming from the grid and, the mixed signal is the base, air and NPC signals as expressed in Equation 5.1.

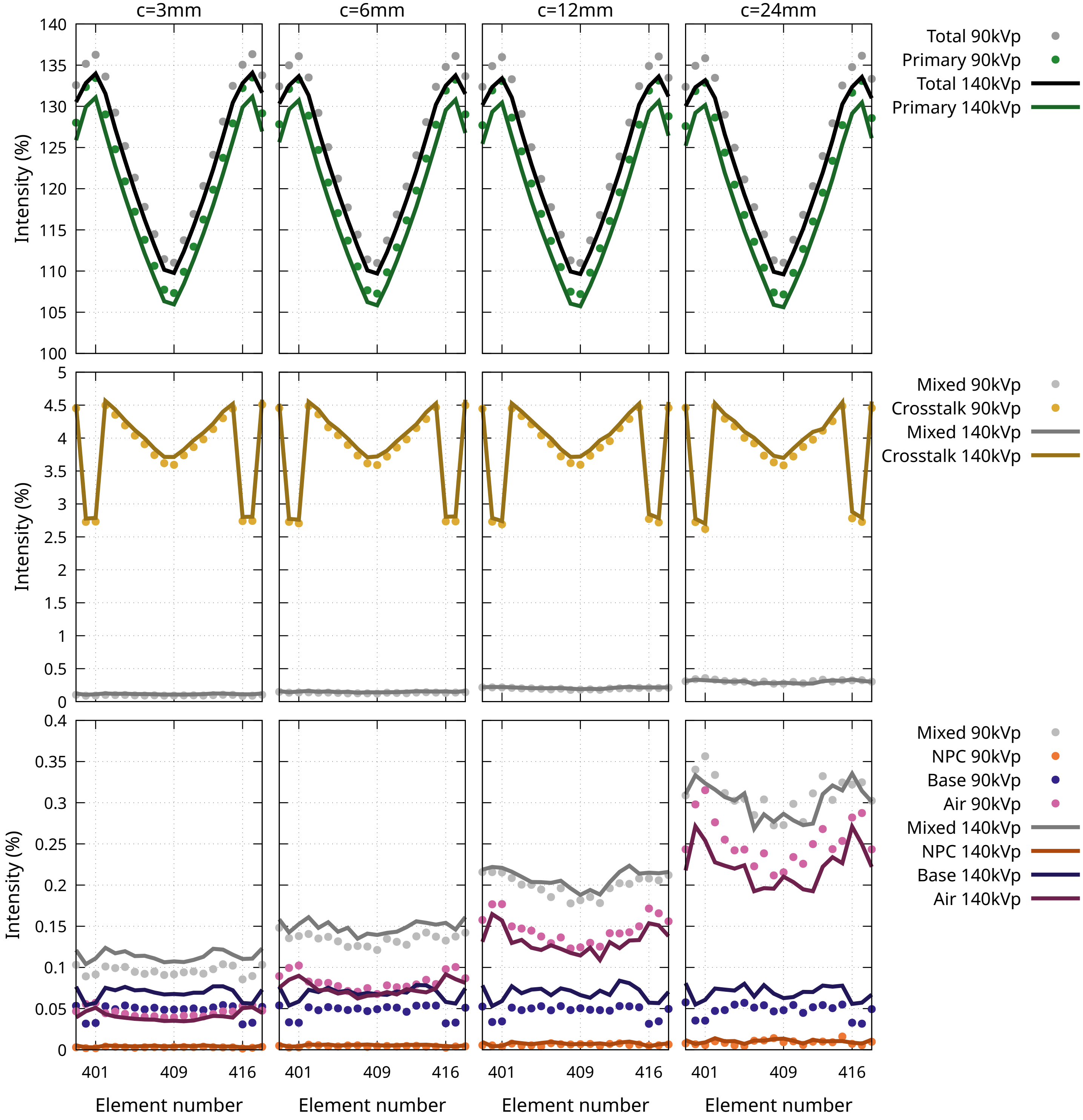

FIGURE 5.8: Signal profiles with no bowtie, no phantom, no septa, in the central module.

In Figure 5.7 for the $90kVp$ and $140kVp$ photon source energies E we found simulations without a bowtie, phantom, or septa present, it is possible to appreciate the different effects when increasing the source collimation. Here we can see the effect of both, the bowtie and septa, structures combined.

The wide change in total signal intensity across the detecting structure in Figure 5.7 of nearly ten times above the 100% intensity is caused by the bowtie filter as seen earlier in Figure 5.5 but, in addition to this effect it is possible to observe valley left in the middle of the modules like in Figure 5.3. A higher signal can be seen at $E = 90kVp$ energy meaning that the attenuation is higher for this energy source.

The primary signal in Figure 5.7 is the highest component of the total signal and behaves very similarly to it, the second one is the crosstalk signal, which is generated from primary events, hence the higher intensity of the primary signal the more crosstalk will be created. The crosstalk signal intensity at $E = 90kVp$ far from the center of the detecting structure appears to be higher in comparison to $E = 140kVp$.

The signal that changes the most when increasing the collimation in Figure 5.7 is the mixed component, this signal increases with the source collimation c for both energies E starting with a very similar intensity value at $c = 3mm$ collimation up to the $c = 24mm$ where for $E = 90kVp$ the intensity is higher.

Signal profiles in Figure 5.8 are in the central module for both $90kVp$ and $140kVp$ tungsten spectra energies E, $3mm$, $6mm$, $12mm$ and $24mm$ collimations c (see Equation 3.2) displayed by columns and a $g = 600mm$ FOV (see Equation 3.1), without the bowtie and septa structures. The total signal is the sum of all the profiles, the crosstalk signal is only from primary events, the bowtie and septa signals are missing and, the mixed signal is the base, air, and NPC signals.

Figure 5.8 shows using a linear scale the small signal changes in the central module separating the total and primary signals from the crosstalk and mixed signals, the bottom row shows each one of the components of the mixed signal.

In Figure 5.8 we see again that the total signal is higher than 110% all over the different collimations and energies, the shape of the curve creates a valley in the central element (409) starting at 111% to 136% for $E = 90kVp$ energy and 110% to 134% for $E = 140kVp$ energy. Since both structures, the bowtie filter and the septa, are missing during the simulation is difficult to observe the attenuation effects of each structure independently.

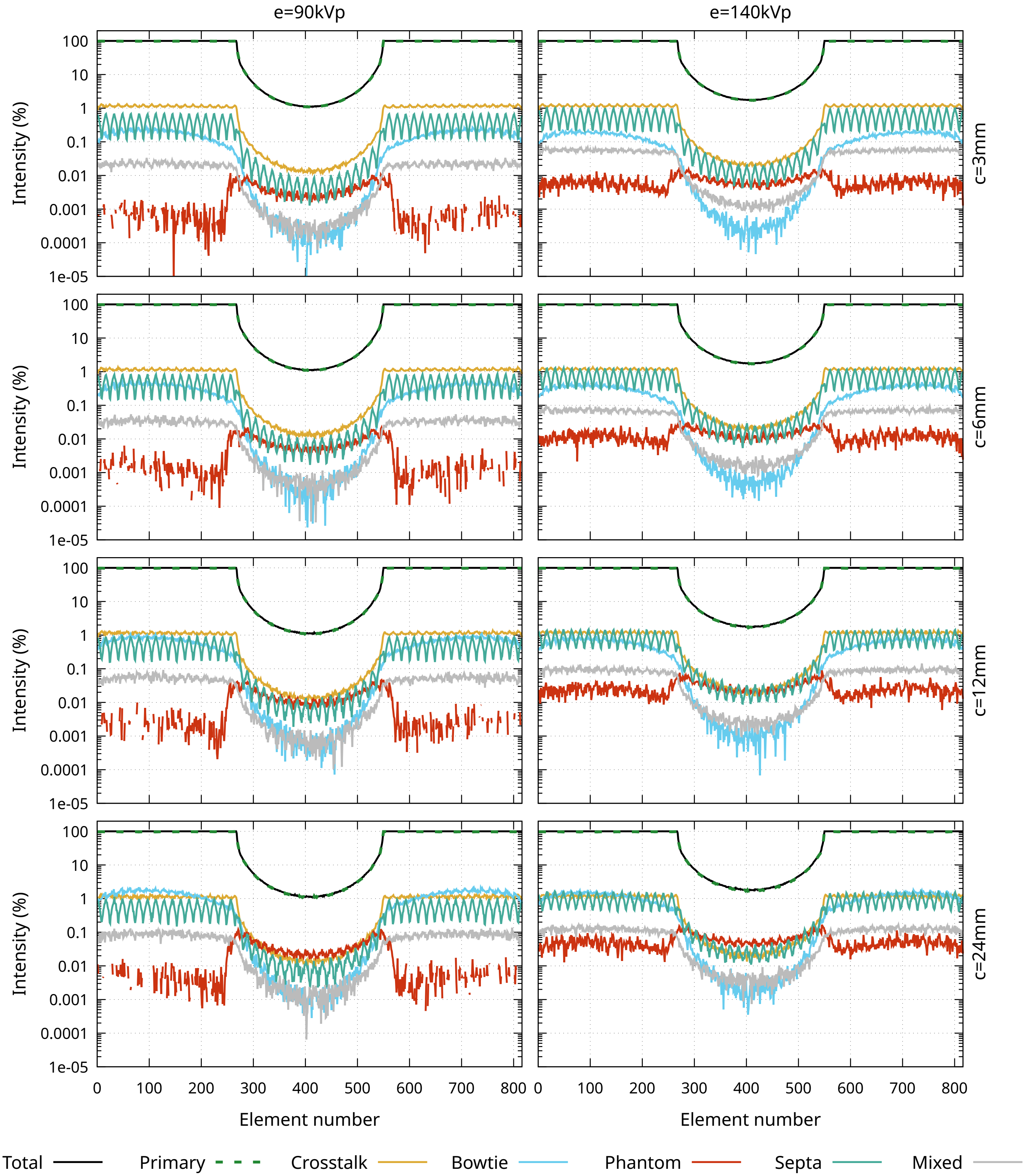

FIGURE 5.9: Signal profiles with bowtie, 215.4*mm* phantom and septa. Central module signal detail in Figure 5.10.

When considering the other signals in Figure 5.8 the intensity represents the attenuation value above the 100% mark and helps to observe the effects when the bowtie filter and septa are missing. The primary signal is about the same in shape and intensity as the total signal because is the biggest contributing signal, the signal range goes from 107% to 133% at $E = 90kVp$ energy and 106% to 131% using $E = 140kVp$ energy. The ratio between the primary and total signal in element (409) is close to 0.96 for both source energies and in element 401 the ratio is 0.98.

The crosstalk signal in Figure 5.8 has almost the same intensity values and curve shape for both energies E. The capital "m" shape returns since the septa structure is missing. The signal intensity in element 409 at $E = 90kVp$ is 0.032 and for $E = 140kVp$ energy.

The mixed signal in Figure 5.8 grows with the source collimation c when looking at each one of the contributions, the one responsible for this increase is the scatter coming from the air since more volume is affected by the source at higher c collimations, the NPC signal also contributes but is an even more negligible value and the base signal is constant across the different collimations c. The ratio between the total and mixed signals at $c = 24mm$ collimation in the central element is 0.00083 for $E = 90kVp$ source energy and 0.00098 for the $E = 40kVp$ energy creating a difference of more than three degrees of magnitude.

5.1.2 Signal profiles with phantom

All the simulations of the previous section did not have a phantom at the isocenter, although we know what are the effects of the scanner structures. For this section three different-sized phantoms will be used, the height of the phantom is always 10 inches but the diameter d varies from $215.4mm$, $270mm$ and $320mm$. For these simulations the same $90kVp$ and $140kVp$ energies E will be used and, the $3mm$, $6mm$, $12mm$, and, $24mm$ collimation c. With a phantom present, the amount of signal is significantly reduced and for the larger phantoms, most of the small signal contributions near the central axis are not appreciable.

Signal profiles in Figure 5.9 are made using both $90kVp$ and $140kVp$ tungsten spectra energies (E) arranged by columns, $3mm$, $6mm$, $12mm$ and $24mm$ collimations c (see Equation 3.2) displayed by row, and a $g = 600mm$ FOV (see Equation 3.1), with the bowtie filter, the septa structure and a $d = 215.4mm$ phantom at the isocenter. The total

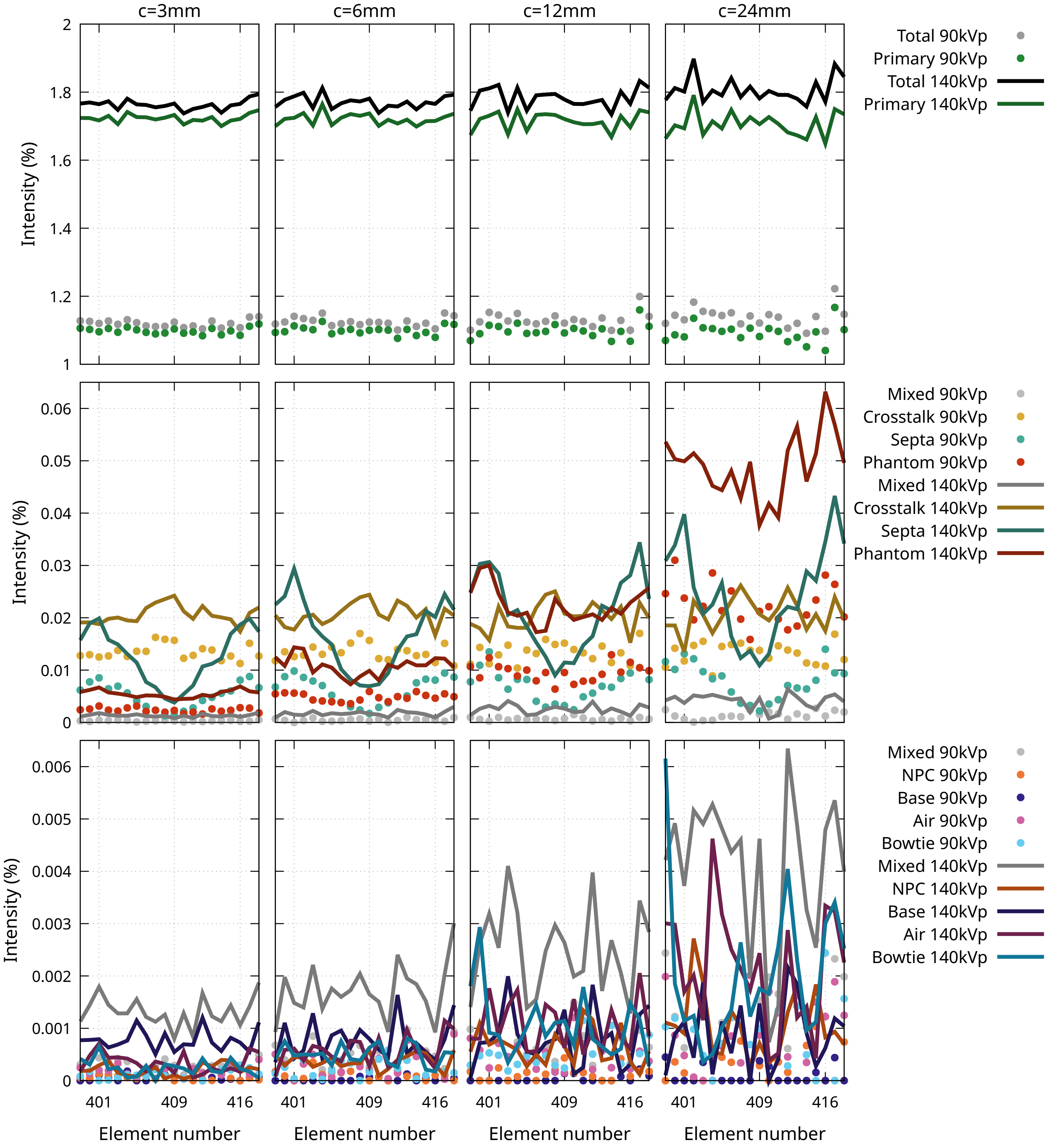

FIGURE 5.10: Signal profiles with bowtie, 215.4mm phantom and septa in the central module.

signal is the sum of all the profiles, the crosstalk signal is only from primary events, the bowtie signal is the scatter coming from the filter, the septa signal is the scatter coming from the grid, the phantom signal is the scatter from the studied object and, the mixed signal is the base, air and NPC signals as expressed in Equation 5.1.

From the total signal in Figure 5.9, it is evident that the attenuation caused by the phantom using $E = 90kVp$ energy is higher with about 1% of signal intensity and for $E = 140kVp$ with a 2% for every source collimation c, also the rest of the non-phantom-signals reduced in the same manner. The primary signal is still the dominant signal and is attenuated accordingly with the passing width of the phantom across the detecting structure.

The phantom's signal in Figure 5.9 resembles a large crater in the center of the detecting structure with wings at the side. The crater is taller and more profound at $E = 90kVp$ source energy, in comparison when using $E = 140kVp$. The wings at $E = 140kVp$ are noisy but the curve is continuous for $E = 90kVp$ there are some elements without phantom signal. Both signals at different energies E increase with the collimation c where at $c = 24mm$ it surpasses the crosstalk signal. Overall when using e=140kVp more scatter that is generated in the phantom reaches the detecting elements.

The crosstalk signal, the septa and the mixed signals have the same module pattern shape as in the air scan in Figure 5.3 but instead of being flat over the detecting structure now they follow the attenuation of the primary signal curve with less intensity.

Signal profiles in Figure 5.10 are in the central module for both $90kVp$ and $140kVp$ tungsten spectra energies E, $3mm$, $6mm$, $12mm$ and $24mm$ collimations c (see Equation 3.2) displayed by columns and a $g = 600mm$ FOV (see Equation 3.1), with the bowtie filter, the septa structure and a $d = 215.4mm$ phantom at the isocenter. The total signal is the sum of all the profiles, the crosstalk signal is only from primary events, the bowtie signal is the scatter coming from the filter, the septa signal is the scatter coming from the grid, the phantom signal is the scatter from the studied object and, the mixed signal is the base, air and NPC signals as expressed in Equation 5.1.

The almost flat total signals in Figure 5.10 are greatly reduced by the phantom attenuation, at $E = 90kVp$ and $c = 3mm$ the intensity is 1.112% and for e=140kp is 1.177%, but at $c = 24mm$ we have 1.112% and 1.178% respectively, inferring that the intensity at $E = 90kVp$ is almost constant at every collimation c, but not for $E = 140kVp$ where a small increase in signal is appreciated.

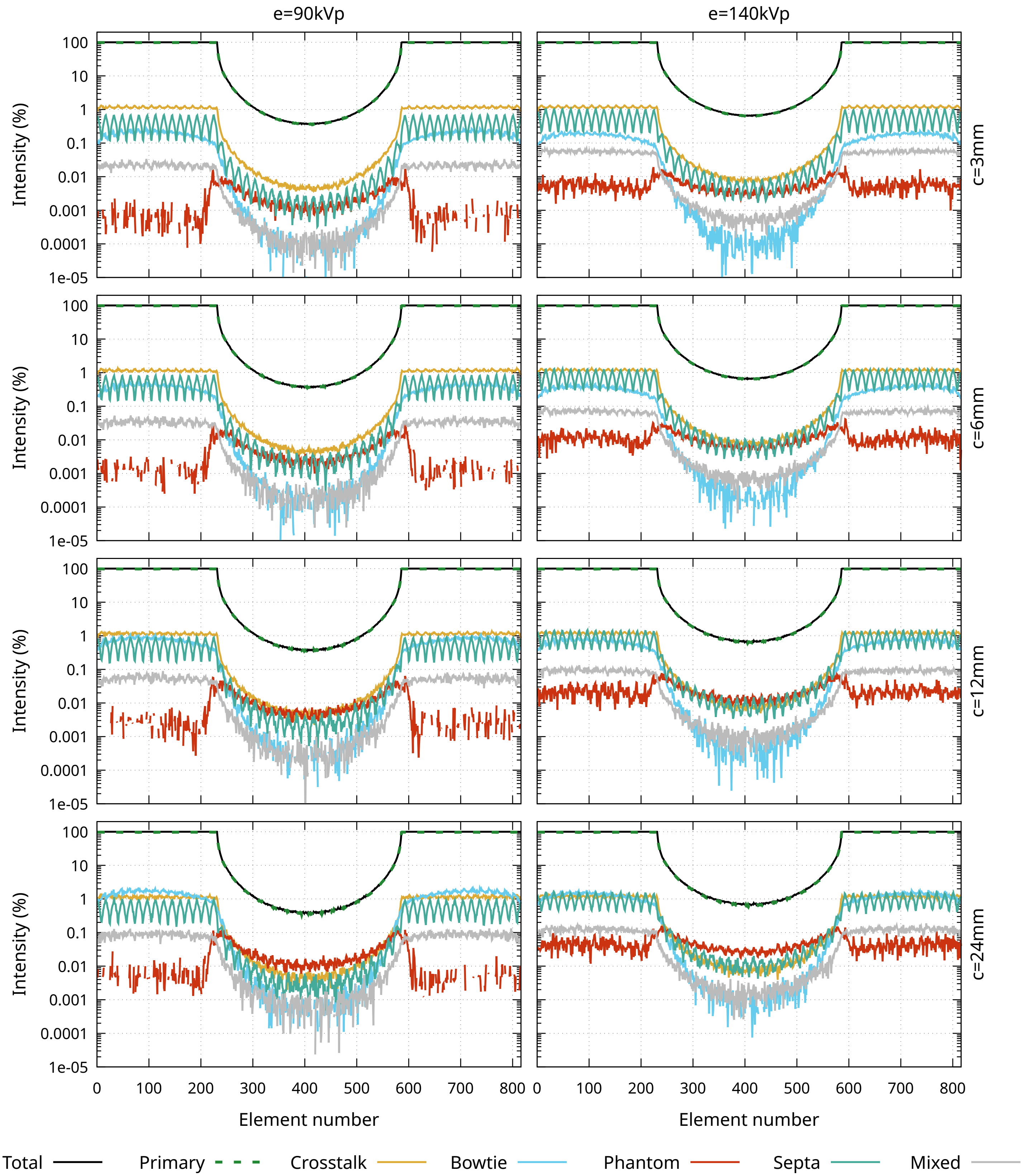

FIGURE 5.11: Signal profiles with bowtie, 270*mm* phantom and septa. Central module signal detail in Figure 5.12.

All the primary signals decrease with the collimation c in Figure 5.10 and as expected for $E = 90kVp$ the photon beam is more attenuated by the phantom, to observe the primary contribution in the total signal, the primary-to-total ratio at $E = 90kVp$ and $c = 3mm$ is 0.982 and at $c = 24mm$ is 0.965, losing close to 1.7% in signal contribution, for $E = 140kVp$ we have 0.981 and 0.958 with a 2.3% lose.

The new signal of interest in Figure 5.10 is the phantom which seems to double the intensity with each increment of the source collimation, at $E = 90kVp$ energy and $c = 3mm$, $c = 6mm$, $c = 12mm$, $c = 24mm$ collimations the phantom-to-total ratios at element 409 are 0.0021, 0.0053, 0.0085 to 0.0189, the same effect happens at $E = 140kVp$ going from 0.0025, 0.0055, 0.0120 to 0.0212. It seems that at $E = 90kVp$ energy less scatter is generated from the phantom.

The scatter-to-primary ratios (see Equation 5.3) in Figure 5.10 using element 409 at $E = 90kVp$ in collimations $c = 3mm$, $c = 6mm$. $c = 12mm$ and $c = 24mm$ are 0.21%, 0.54%, 0.87% and 1.96% respectively and at $E = 140kVp$ we have 0.25%, 0.57%, 1.24% and 2.21%.

The bowtie signal contribution in the central module is already three orders of magnitude below the total signal in Figure 5.2, the same happens with a $d = 215.4mm$ phantom in Figure 5.10 the total-to-bowtie ratios in element 409 at $90kVp$ and $c = 24mm$ is 0.00089 and at $140kVp$ is 0.00099. The bowtie signal is often used as part of the primary signal, but when compared to the primary signal contribution it may seem negligible, to look deeper into the bowtie signal contribution a bowtie-to-phantom ratio in element 409 is calculated, at $E = 90kVp$ and collimations $c = 3mm$, $c = 6mm$, $c = 12mm$ and $c = 24mm$ we have 0.068, 0.028, 0.025, 0.047 respectively, and at $E = 140kVp$ the ratios are 0.063, 0.064, 0.053 and 0.047, we can say that the bowtie signal accounts in between

$$2\%$$

to 6% percent of the phantom signal.

The crosstalk signal remains the same across collimations c in Figure 5.10 with a change in intensity by the energy. The crosstalk-to-total ratio at e=90kVp and e=140kVp is between 1% and 2% which is very close to the signal obtained in Figure 5.2 since the crosstalk signal is only generated by primary photons and the total signal is mainly primary signal, the crosstalk contribution should remain the same.

The septa signal shape in Figure 5.10 is similar to the one observed in Figure 5.2.

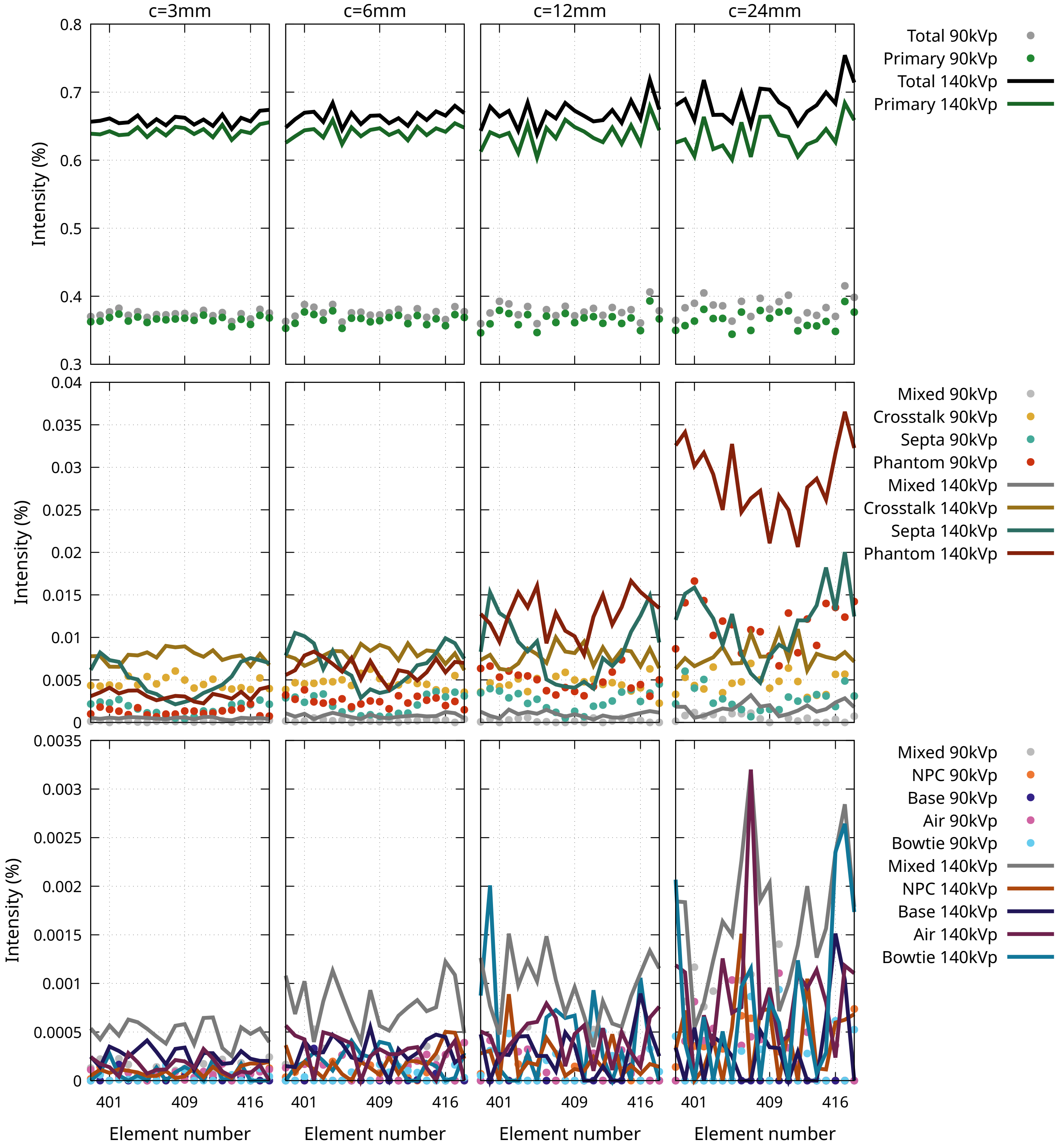

FIGURE 5.12: Signal profiles with bowtie, 270mm phantom and septa in the central module.

The signal at $E = 90kVp$ remains under the crosstalk signal at collimations $c = 3mm$ and $c = 6mm$ for the other collimation it surpasses the crosstalk signal at the side of the module, for $E = 140kVp$ the signal is always on top of the crosstalk.

The mixed signal whose highest scatter contributor was the air now has some of its volume replaced by the phantom, the mixed-to-total ratio in the element is 409 at $E = 90kVp$ for collimations $c = 3mm$, $c = 6mm$, $c = 12mm$ and $c = 24mm$ are 0.0003, 0.0002, 0.0006 and 0.0014, at 140kVp we have 0.0005, 0.0009, 0.0015 and 0.0026, we see that at high collimation numbers, especially at 140kVp the mixed signal is not longer with three orders of magnitude difference, which is unexpected due to the loss in air contribution.

Signal profiles in Figure 5.11 are made using both $90kVp$ and $140kVp$ tungsten spectra energies (E) arranged by columns, $3mm$, $6mm$, $12mm$ and $24mm$ collimations c (see Equation 3.2) displayed by row, and a $g = 600mm$ FOV (see Equation 3.1), with the bowtie filter, the septa structure and a $d = 270mm$ phantom at the isocenter. The total signal is the sum of all the profiles, the crosstalk signal is only from primary events, the bowtie signal is the scatter coming from the filter, the septa signal is the scatter coming from the grid, the phantom signal is the scatter from the studied object and, the mixed signal is the base, air and NPC signals as expressed in Equation 5.1.

In Figure 5.11 we can see that the attenuation is higher when using a bigger phantom, now for both energies, the total signal falls below 1%, also the attenuation of the signal starts at earlier elements on the left side of the detecting structure and later at the right side. The primary signal is still dominant, following closely the same shape as the total signal.

For the phantom signal in Figure 5.11, we have a greater crater naturally by using a larger phantom, the same lack of signal is found at the wings when using $E = 90kVp$ and for $E = 140kVp$ the signal is noisy. The crater is still taller at e=90kVp than at e=140kVp and for both energies E, the intensity increases with the collimation c, where at c=12mm the signal is already higher than the crosstalk signal at the central module.

The crosstalk, bowtie, septa and mixed signals in Figure 5.11 behave the same as with the previous smaller phantom, but with more elements blocked in the detecting structure and a higher attenuation at the central module. The evolving problem is that with a thicker phantom, the data below becomes noisier and is more challenging to analyze the data. For example, we can see that some elements in the bowtie filter signal are not receiving signal at all.

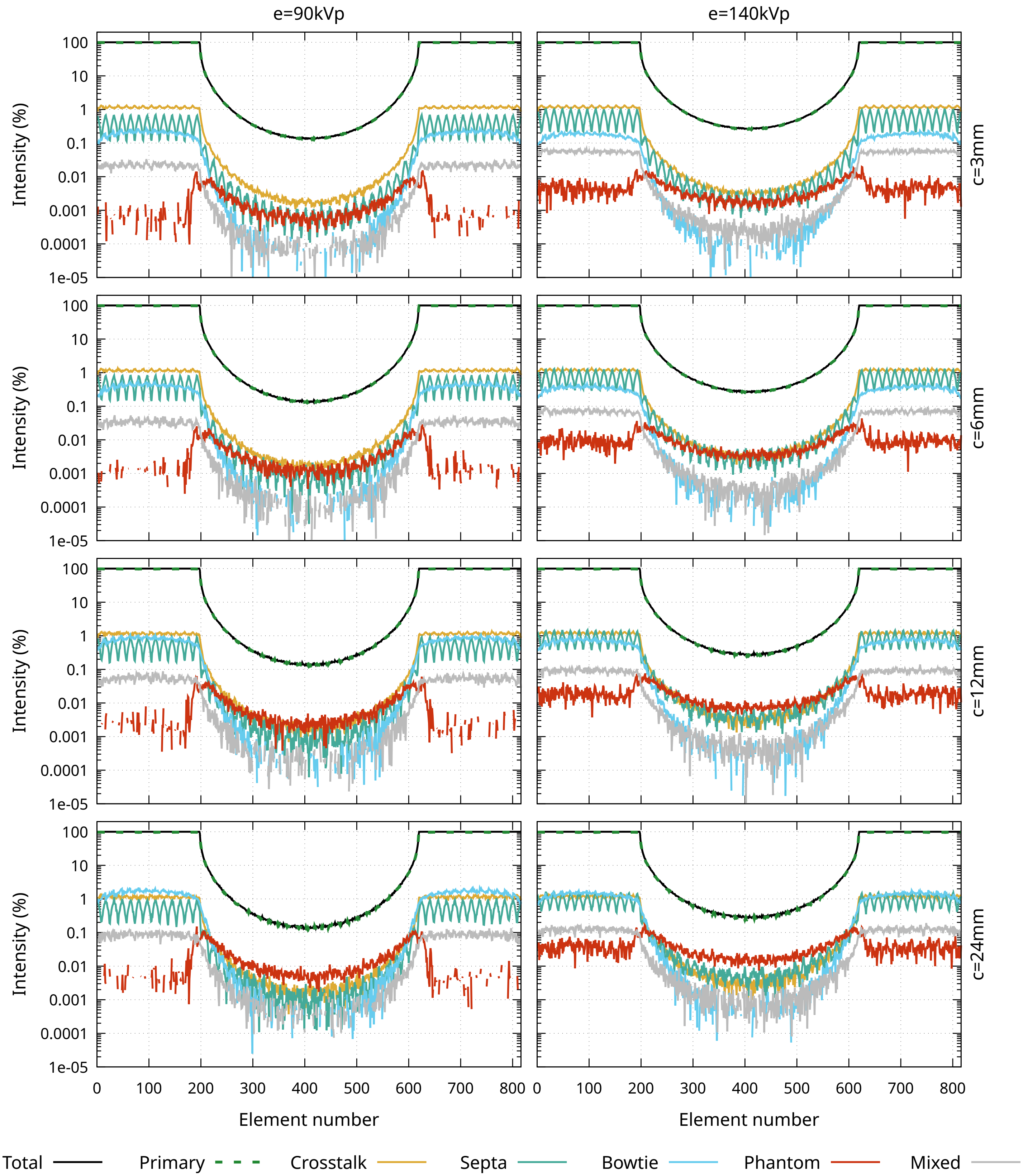

FIGURE 5.13: Signal profiles with bowtie, 320mm phantom and septa. Central module signal detail in Figure 5.14.

Signal profiles in Figure 5.12 are in the central module for both $90kVp$ and $140kVp$ tungsten spectra energies E, $3mm$, $6mm$, $12mm$ and $24mm$ collimations c (see Equation 3.2) displayed by columns and a $g = 600mm$ FOV (see Equation 3.1), with the bowtie filter, the septa structure and a $d = 270mm$ phantom at the isocenter. The total signal is the sum of all the profiles, the crosstalk signal is only from primary events, the bowtie signal is the scatter coming from the filter, the septa signal is the scatter coming from the grid, the phantom signal is the scatter from the studied object and, the mixed signal is the base, air and NPC signals as expressed in Equation 5.1.

The total signal in Figure 5.12 is about 0.38% for $E = 90kVp$ at all collimations c but for $E = 140kVp$ the intensity changes from 0.66% to 0.70% for $c = 3mm$, $c = 24mm$ respectively. The primary-to-total ratio for $E = 90kVp$ is 0.981 at $c = 3mm$ down to 0.965 at $c = 24mm$, for $E = 140kVp$ we have 0.977 and 0.944 respectively.

The phantom signal has the same increasing pattern with the collimation c at both energies E and the intensity at $E = 140kVp$ is higher in Figure 5.12. The phantom-to-total ratio at $E = 90kVp$ and collimations $c = 3mm$, $c = 6mm$, $c = 12mm$ and $c = 24mm$ are 0.0036, 0.0066, 0.0098 and 0.0205, where the same doubling effect is observed but the data noise blurs the effect, and for $E = 140kVp$ we have 0.0046, 0.0081, 0.0151 and 0.0299 respectively.

The scatter-to-primary ratios (see Equation 5.3) in Figure 5.12 using element 409 at $E = 90kVp$ in collimations $c = 3mm$, $c = 6mm.$ $c = 12mm$ and $c = 24mm$ are 0.37%, 0.67%, 1.01% and 2.13% respectively and at $E = 140kVp$ we have 0.47%, 0.83%, 1.56% and 3.17%, which are higher than the $d = 215.4mm$ phantom.

The bowtie and mixed signal data is very noisy in Figure 5.12, but either way, the bowtie-to-total and mixed-to-total ratios will be given. The bowtie-to-total ratio at $E = 90kVp$ for $c = 3mm$ and $c = 6mm$ are 0.0003 and 0.0005 the rest of the collimations c did not receive any energy from the filter, at $E = 140kVp$ we have 0.0002, 0.0006, 0.0010 and 0.0012 for $c = 3mm$, $c = 6mm$, $c = 12mm$ and $c = 24mm$. For the mixed signal at $E = 90kVp$, the ratios are 0.0003, 0.0002, 0.0004 and 0.000 and for $E = 140kVp$ we have 0.0009, 0.0009, 0.0014 and 0.0029.

Signal profiles in Figure 5.13 are made using both $90kVp$ and $140kVp$ tungsten spectra energies (E) arranged by columns, $3mm$, $6mm$, $12mm$ and $24mm$ collimations c (see Equation 3.2) displayed by row, and a $g = 600mm$ FOV (see Equation 3.1), with the bowtie filter, the septa structure and a $d = 320mm$ phantom at the isocenter. The total

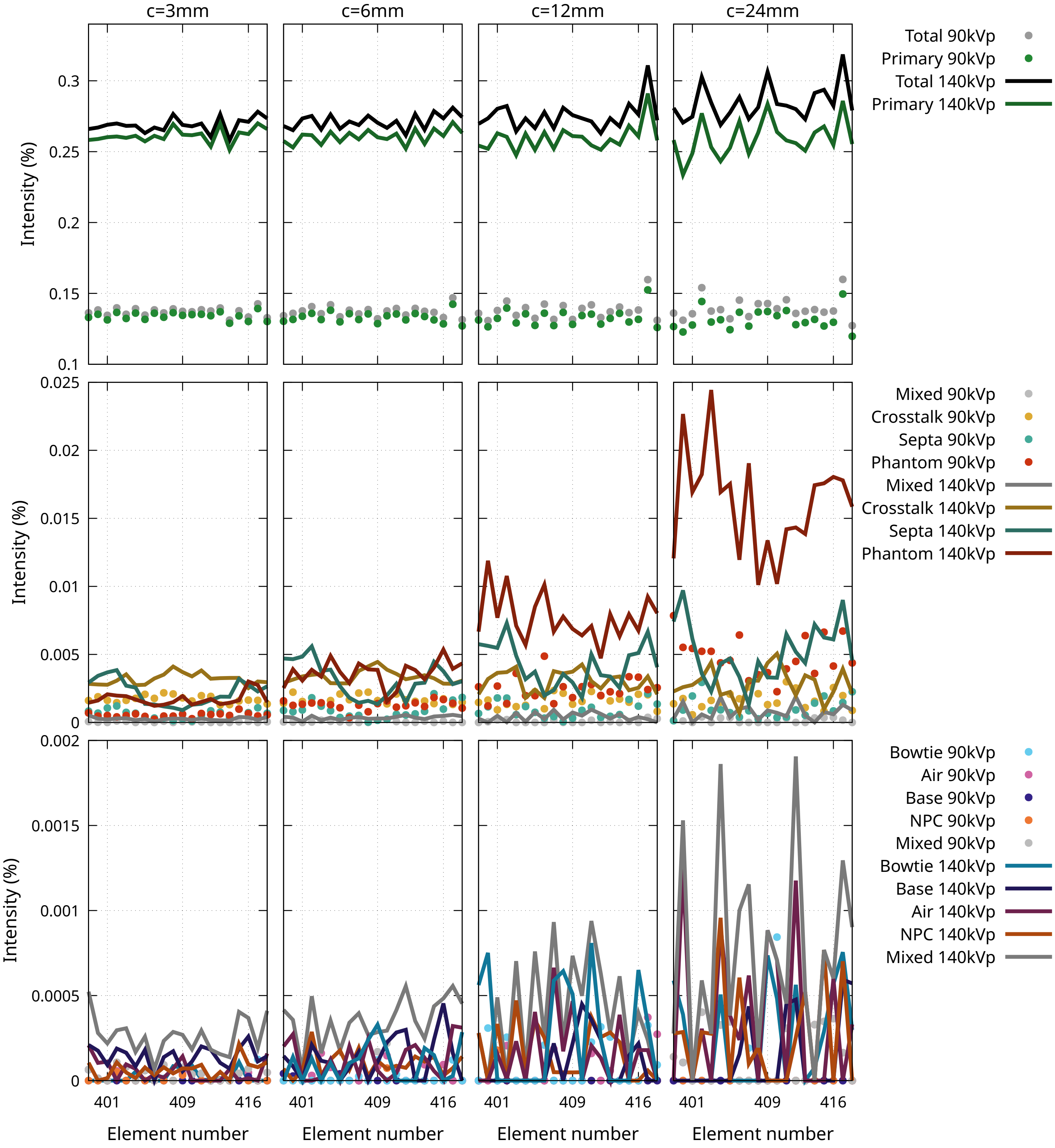

FIGURE 5.14: Signal profiles with bowtie, 320*mm* phantom and septa in the central module.

signal is the sum of all the profiles, the crosstalk signal is only from primary events, the bowtie signal is the scatter coming from the filter, the septa signal is the scatter coming from the grid, the phantom signal is the scatter from the studied object and, the mixed signal is the base, air and NPC signals as expressed in Equation 5.1.

The total signal when $d = 320mm$ can be seen in Figure 5.13, as expected, the shadow of the phantom is bigger in the detecting structure and the attenuation on the central module is even higher than for the previous two phantoms. The signal is close to 0.1% at $E = 90kVp$ and close to 0.5% for $E = 140kVp$. The primary signal is the dominant contributor and behaves just like the total signal also, it is possible to see that the total and primary signals are getting noisier at collimations $c = 12mm$ and $c = 24mm$.

The phantom signal has the same shape as in previous Figures, in Figure 5.13 the crater is wider than for any other phantom and less signal is generated at the wings of the signal. At $E = 90kVp$ we can see that several spots outside the crater did not receive a signal from the phantom and at $E = 140kVp$ the signal is noisier than before. The crater is still taller when $E = 90kVp$ and the intensity increases with the collimation c as discussed previously for other phantom diameters.

The crosstalk and septa signals in Figure 5.13 behave similarly as in Figure 5.11 but with a higher attenuation below the phantom. Meanwhile, the bowtie and mixed signals are heavily affected by the phantom's effect and some spots in the phantom shadow have not recorded any interaction.

Signal profiles in Figure 5.14 are in the central module for both $90kVp$ and $140kVp$ tungsten spectra energies E, $3mm$, $6mm$, $12mm$ and $24mm$ collimations c (see Equation 3.2) displayed by columns and a $g = 600mm$ FOV (see Equation 3.1), with the bowtie filter, the septa structure and a $d = 320mm$ phantom at the isocenter. The total signal is the sum of all the profiles, the crosstalk signal is only from primary events, the bowtie signal is the scatter coming from the filter, the septa signal is the scatter coming from the grid, the phantom signal is the scatter from the studied object and, the mixed signal is the base, air and NPC signals as expressed in Equation 5.1.

Looking at the total signal in the central module in Figure 5.14, the intensity with e=90kVp is close to 0.14% and at $E = 140kVp$ lightly increasing with the collimation c where at $c = 3mm, c = 6mm, c = 12mm$ and $c = 24mm$ we have 0.27%, 0.27%, 0.28% and 0.31% respectively. The primary-to-total ratios at $E = 90kVp$ are 0.98, 0.97, 0.97 and 0.96 respectively and at $E = 140kVp$ we have 0.97, 0.96, 0.95 and 0.93 respectively, which is a decrease in primary signal with the collimation number.

The phantom signal in Figure 5.14 has the same intensity-increasing effect with the collimation c as observed earlier, with higher values for $E = 140kVp$, the phantom-to-total ratio at $E = 90kVp$ for c=3mm, c=6mm, c=12mm and c=24mm are 0.0044, 0.0105, 0.0139 and 0.0256 and at $E = 140kVp$ we have 0.0072, 0.0143, 0.0249 and 0.0437.

The scatter-to-primary ratios (see Equation 5.3) in Figure 5.14 using element 409 at $E = 90kVp$ in collimations $c = 3mm$, $c = 6mm$. $c = 12mm$ and $c = 24mm$ are 0.45%, 1.08%, 1.43% and 2.67% respectively and at $E = 140kVp$ we have 0.74%, 1.48%, 2.63% and 4.71%, which are higher than the $d = 215.4mm$ and $d = 270mm$ phantoms.

Much of the behavior about the crosstalk and septa signals has already been discussed, it is expected to observe less intensity with a bigger phantom, hence the more important information to relate is the crosstalk-to-total ratios that at $E = 90kVp$ and $c = 3mm$, $c = 6mm$, $c = 12mm$ and $c = 24mm$ are 0.013, 0.012, 0.010 and 0.009 respectively, for $E = 140kVp$ we have 0.014, 0.017, 0.014, 0.014 which in all cases account to about 1% of the total signal. For the mixed-to-total ratios at $E = 90kVp$, we have 0.0020, 0.0012, 0.0024 and 0.0047 and at e=140kVp they are 0.0034, 0.0050, 0.0106 and 0.0108.

One of the implementations related to the flowchart in Figure 3.5, is the ability of the code to store the type of photon interaction, whether it is Compton, Rayleigh, or photoelectric, and separate them into different signal contributions. Since normalized scatter profiles (NSP) and scatter-to-primary ratios (SPR) are out of the scope of this project the plot for these profiles is part of the appendices in the document. The NSP are in Appendix A and the SPR in Appendix B.

Chapter 6

Conclusions and future directions

6.1 Conclusions

The implementations made in the code successfully emulate the scanner structures such as the bowtie filter and the septa successfully attenuating the X-ray beam and modifying the signal profiles accordingly.

The total signal is separated using the algorithm stated in Figure 3.5 where the different signal profiles are stored according to the volume where the photon last interacted before reaching a detecting element. The signal characterization includes the scatter from the phantom, each scanner structure, air, and crosstalk signals.

The total and partial contribution of every signal profile has been taken into account in the simulations done to help understand the impact that each signal profile has in a static projection, and additional SPR and NSP to measure the scatter generated by the phantom and how the other signal profile, especially the primary signal, is being affected by it.

Overall we successfully developed a Monte Carlo code using Geant4, capable of mimicking a third-generetion commercially available CT scanner and categorizing the different signals into primary and scatter signals.

6.2 Future Directions

In simulations where a phantom is placed a the isocenter, especially for large phantoms, the data obtained is noisy or even absent and may require more simulated photons to smooth it out, also, percentage error can be improved, and a new set of simulations, or extending the current ones may help to solve this issues. A good balance must be found between computation time and acceptable data.

In future simulations a complete array in two dimensions can be simulated, to observe the signal profiles in the z-axis of the scanner and not only in the $X - Y$ plane, see Figure 3.1, where changes in the crosstalk signal are expected since the septumes are parallel to the Z coordinate.

The scatter profiles can be used to improve quantitative properties of the image in reconstruction algorithms, by finding linear errors caused by the scatter signals.

Appendix A

Normalized Scatter Profiles

A.1 Normalized scatter profiles (NSP)

The normalization used for the NSP is explained in Equation A.1.

$$NSP_i = 100 * \frac{S_i}{P_{409} + P'_{409}} \tag{A.1}$$

Where:

- NSP_i: Is the NSP in element i.
- S_i: Is the phantom signal in an element i.
- P_{409}: Is the primary signal in element 409.
- P'_{409}: Is the bowtie signal in element 409.

Normalized scatter profiles in Figure A.1 for a 215.4mm phantom with both 90kVp and 140kVp tungsten spectra energies e arranged by columns, 3mm, 6mm, 12mm and 24mm collimations c (see Equation 3.2) displayed on each octant, and a $g = 600mm$ FOV (see Equation 3.1). The phantom signal is the sum of the Compton and Rayleigh contributions.

Normalized scatter profiles in Figure A.2 for a 215.4mm phantom using both 90kVp and 140kVp tungsten spectra energies e arranged by columns, 3mm, 6mm, 12mm and 24mm collimations c (see Equation 3.2) displayed on each octant, and a $g = 600mm$ FOV (see Equation 3.1). The phantom signal is the sum of the Compton and Rayleigh contributions.

Normalized scatter profiles in Figure A.3 for a 270mm phantom using both 90kVp and 140kVp tungsten spectra energies e arranged by columns, 3mm, 6mm, 12mm and 24mm collimations c (see Equation 3.2) displayed on each octant, and a $g = 600mm$ FOV (see Equation 3.1). The phantom signal is the sum of the Compton and Rayleigh contributions.

Normalized scatter profiles in Figure A.4 for a 270mm phantom using both 90kVp and

$140kVp$ tungsten spectra energies e arranged by columns, $3mm$, $6mm$, $12mm$ and $24mm$ collimations c (see Equation 3.2) displayed on each octant, and a $g = 600mm$ FOV (see Equation 3.1). The phantom signal is the sum of the Compton and Rayleigh contributions.

Normalized scatter profiles in Figure A.5 for a $320mm$ phantom using both $90kVp$ and $140kVp$ tungsten spectra energies e arranged by columns, $3mm$, $6mm$, $12mm$ and $24mm$ collimations c (see Equation 3.2) displayed on each octant, and a $g = 600mm$ FOV (see Equation 3.1). The phantom signal is the sum of the Compton and Rayleigh contributions.

Normalized scatter profiles in Figure A.6 for a $320mm$ phantom using both $90kVp$ and $140kVp$ tungsten spectra energies e arranged by columns, $3mm$, $6mm$, $12mm$ and $24mm$ collimations c (see Equation 3.2) displayed on each octant, and a $g = 600mm$ FOV (see Equation 3.1). The phantom signal is the sum of the Compton and Rayleigh contributions.

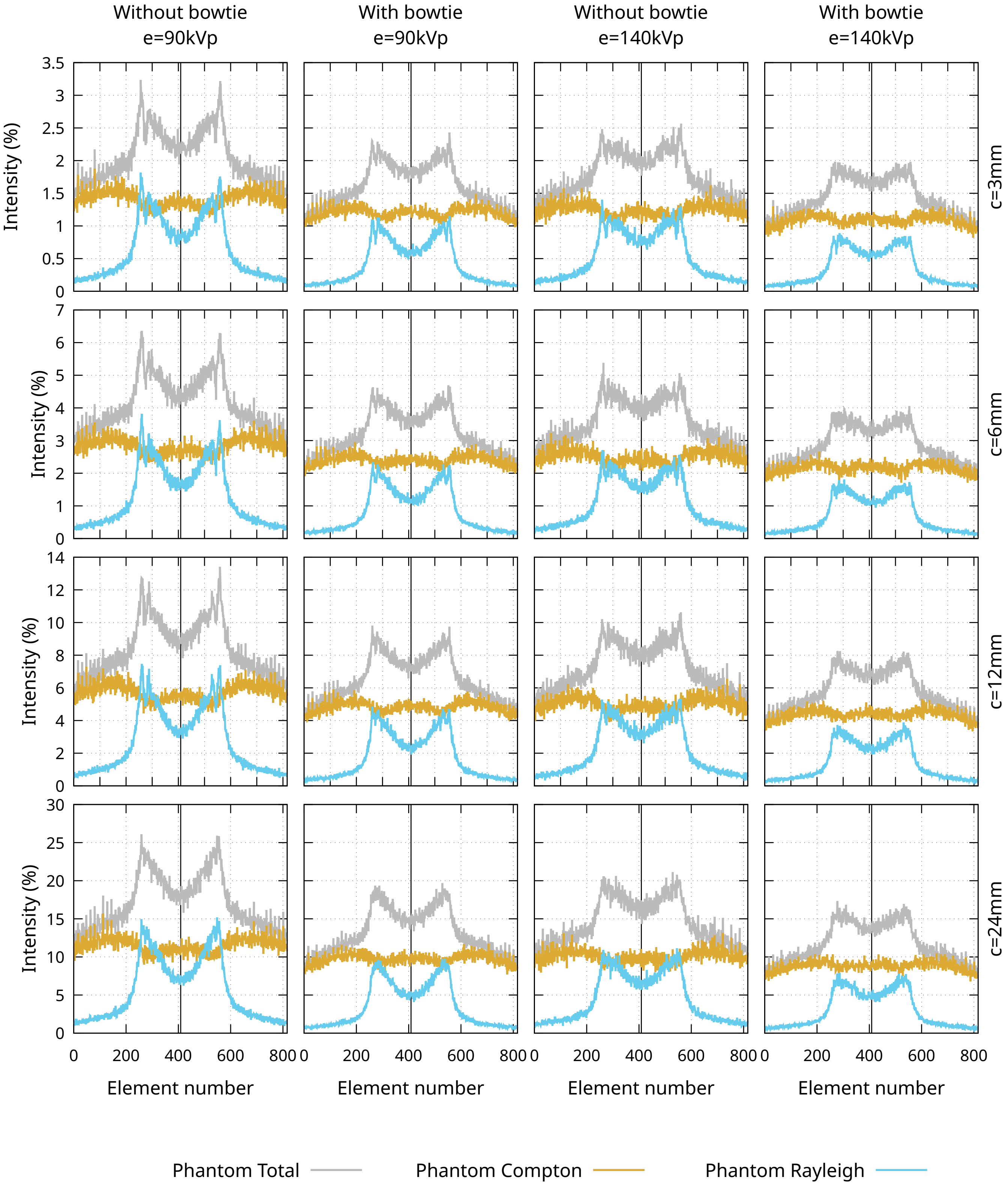

FIGURE A.1: Phantom scatter profiles of a 215.4mm diameter phantom without septa.

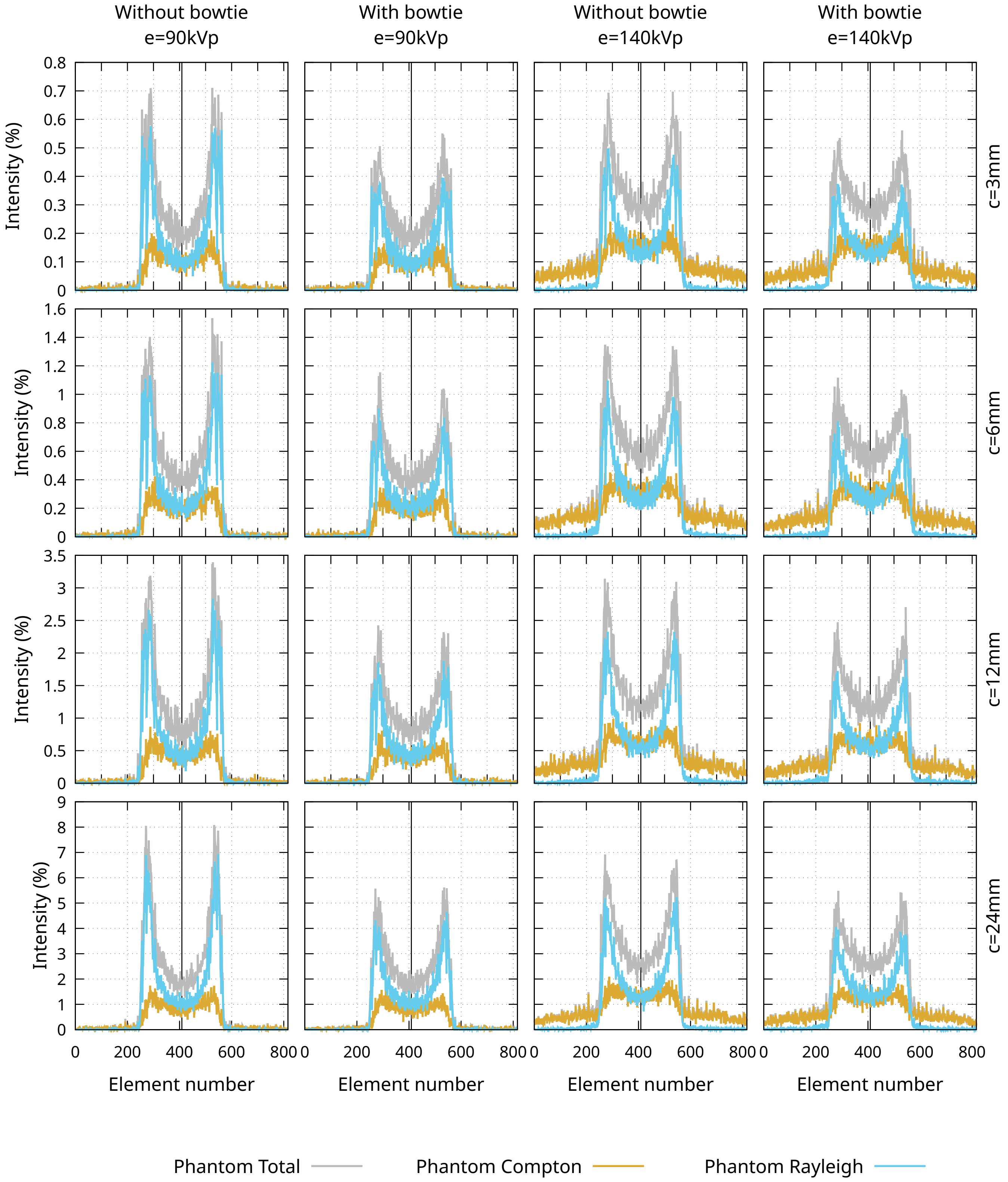

FIGURE A.2: Phantom scatter profiles of a 215.4mm diameter phantom with septa.

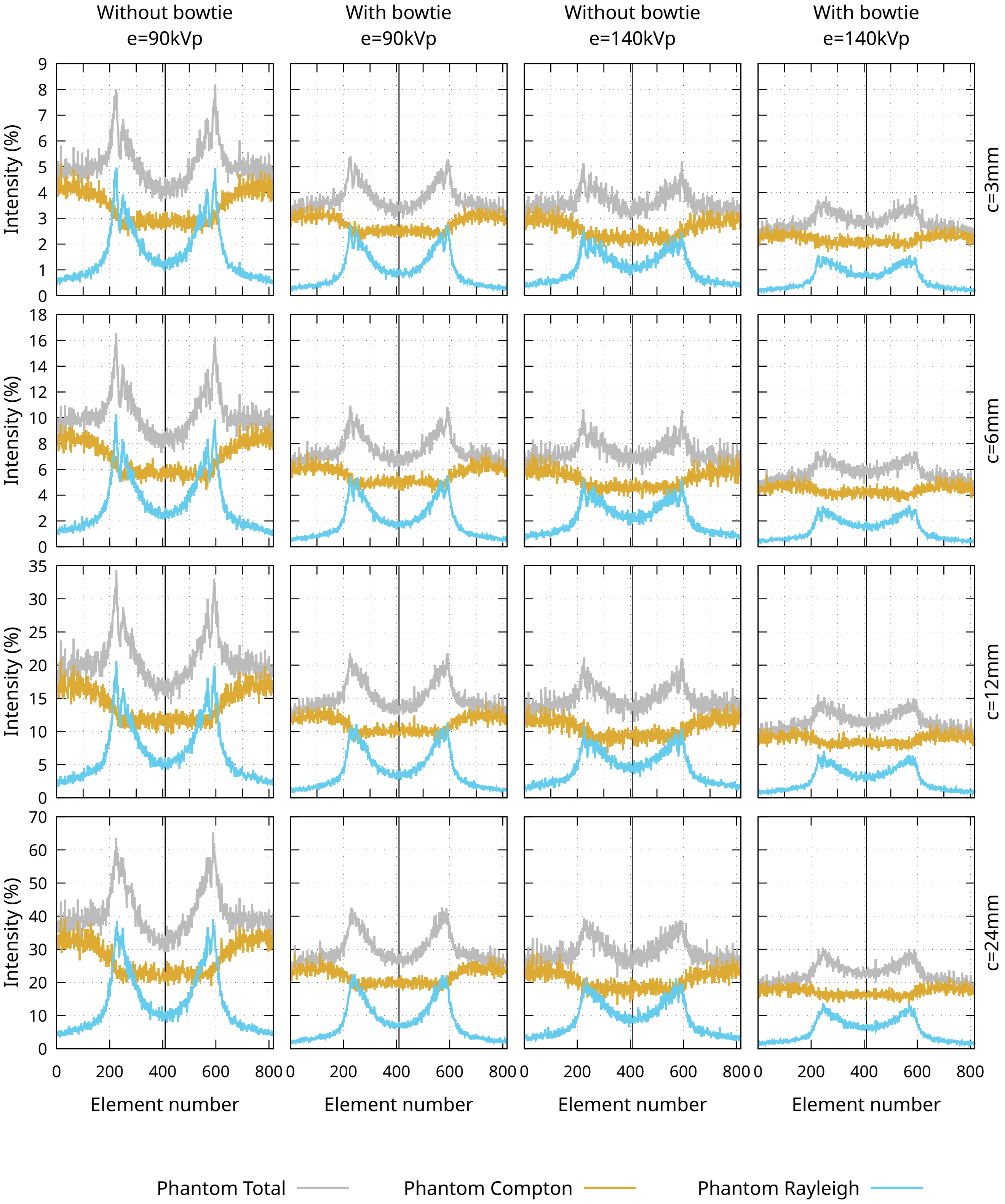

FIGURE A.3: Phantom scatter profiles of a 270mm diameter phantom without septa.

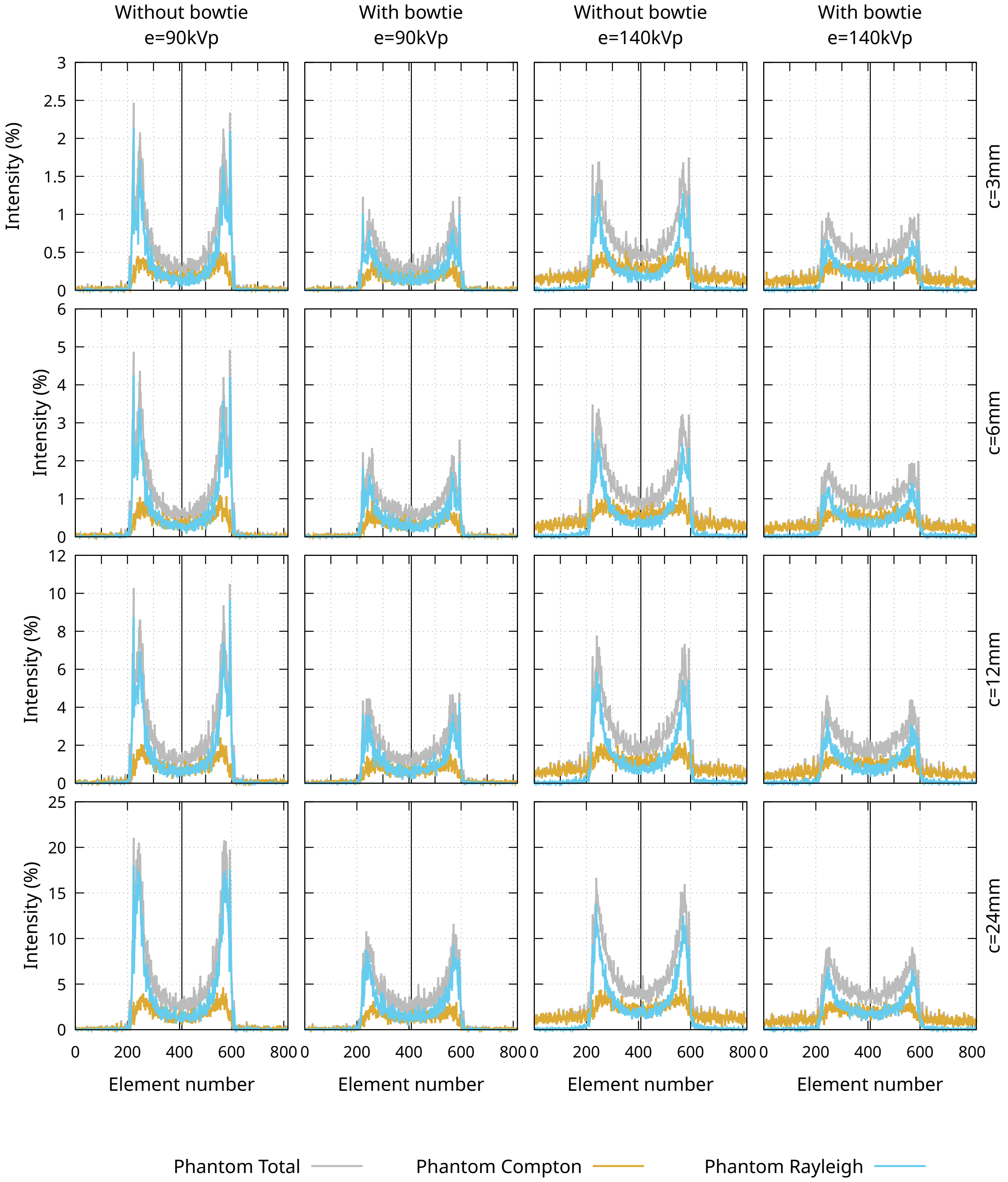

FIGURE A.4: Phantom scatter profiles of a 270mm diameter phantom with septa.

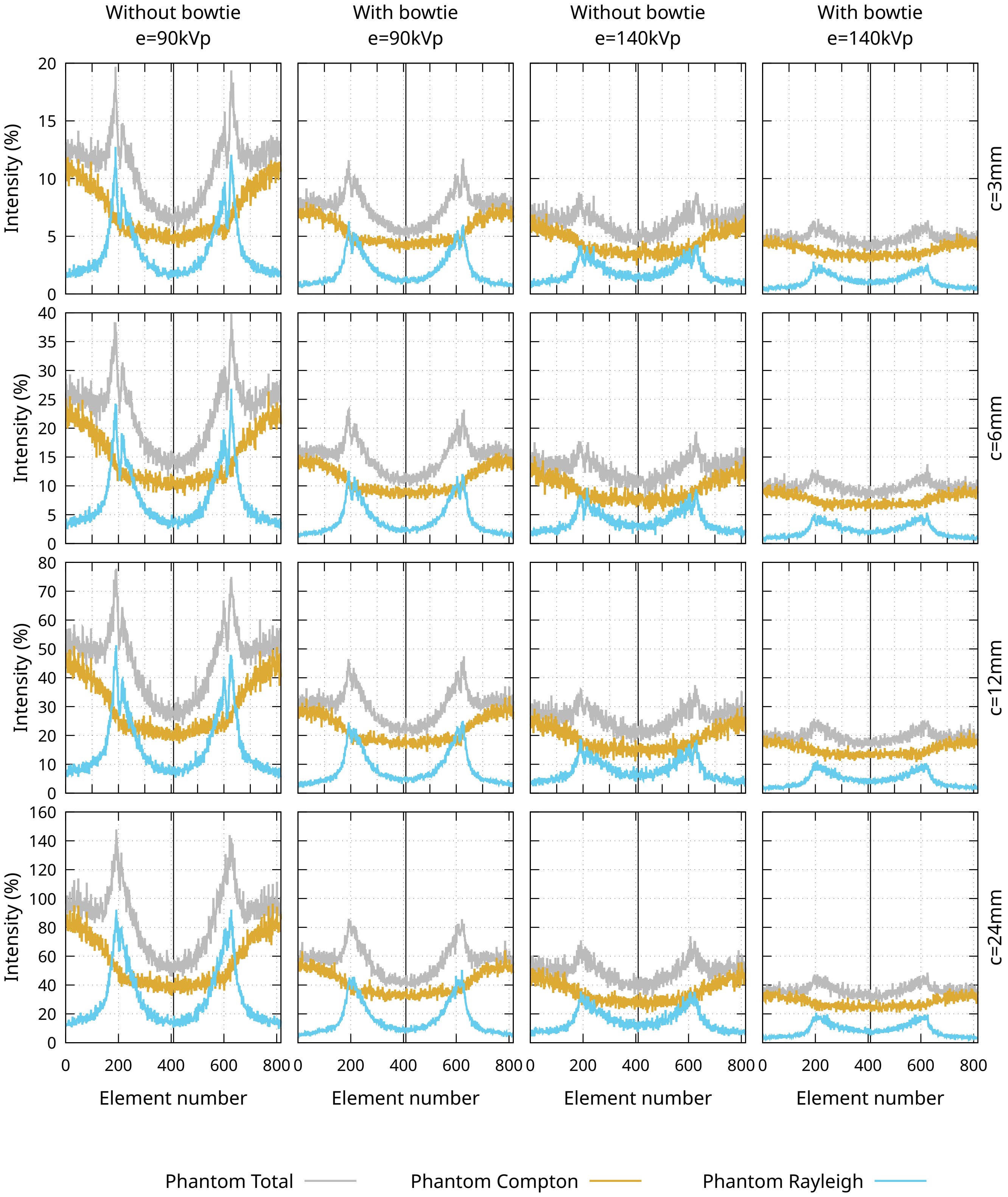

FIGURE A.5: Phantom scatter profiles of a 320mm diameter phantom without septa.

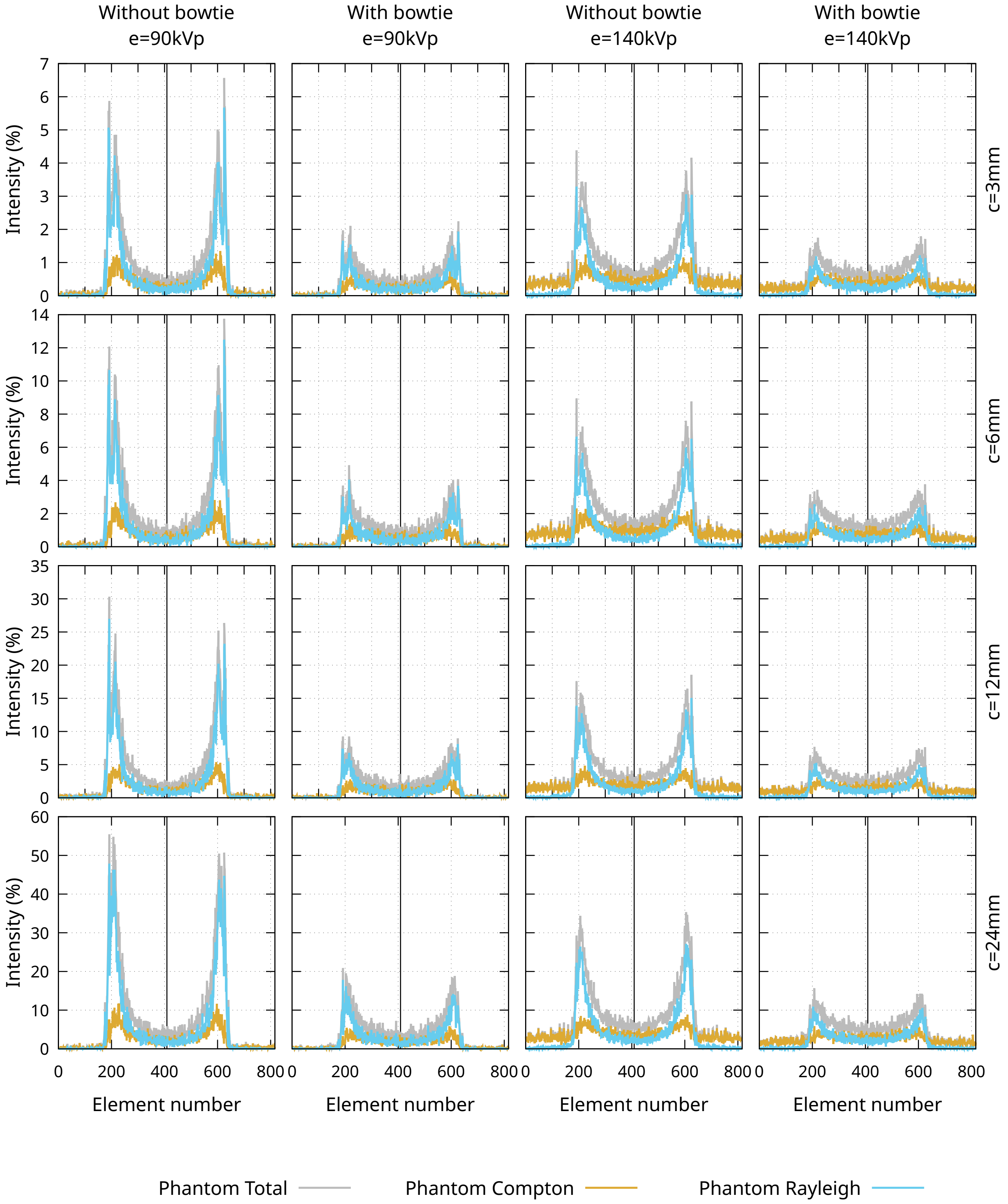

FIGURE A.6: Phantom scatter profiles of a 320mm diameter phantom with septa.

Appendix B

Scatter-to-primary Ratios

B.1 Scatter-to-primary ratios

The normalization used for the SPR is explained in Equation B.1.

$$SPR_i = 100 * \frac{S_i}{P_i + P_i'} \tag{B.1}$$

Where:

- SPR_i: Is the SPR in element i.
- S_i: Is the phantom signal in an element i.
- P_i: Is the primary signal in element i.
- P_i': Is the bowtie signal in element i.

Scatter-to-primary ratios in Figure A.1 for a 215.4mm phantom with both 90kVp and 140kVp tungsten spectra energies e arranged by columns, 3mm, 6mm, 12mm and 24mm collimations c (see Equation 3.2) displayed on each octant, and a $g = 600mm$ FOV (see Equation 3.1). The phantom signal is the sum of the Compton and Rayleigh contributions.

Scatter-to-primary ratios in Figure A.2 for a 215.4mm phantom using both 90kVp and 140kVp tungsten spectra energies e arranged by columns, 3mm, 6mm, 12mm and 24mm collimations c (see Equation 3.2) displayed on each octant, and a $g = 600mm$ FOV (see Equation 3.1). The phantom signal is the sum of the Compton and Rayleigh contributions.

Scatter-to-primary ratios in Figure A.3 for a 270mm phantom using both 90kVp and 140kVp tungsten spectra energies e arranged by columns, 3mm, 6mm, 12mm and 24mm collimations c (see Equation 3.2) displayed on each octant, and a $g = 600mm$ FOV (see Equation 3.1). The phantom signal is the sum of the Compton and Rayleigh contributions.

Scatter-to-primary ratios in Figure A.4 for a 270mm phantom using both 90kVp and

$140kVp$ tungsten spectra energies e arranged by columns, $3mm$, $6mm$, $12mm$ and $24mm$ collimations c (see Equation 3.2) displayed on each octant, and a $g = 600mm$ FOV (see Equation 3.1). The phantom signal is the sum of the Compton and Rayleigh contributions.

Scatter-to-primary ratios in Figure A.5 for a $320mm$ phantom using both $90kVp$ and $140kVp$ tungsten spectra energies e arranged by columns, $3mm$, $6mm$, $12mm$ and $24mm$ collimations c (see Equation 3.2) displayed on each octant, and a $g = 600mm$ FOV (see Equation 3.1). The phantom signal is the sum of the Compton and Rayleigh contributions.

Scatter-to-primary ratios in Figure A.6 for a $320mm$ phantom using both $90kVp$ and $140kVp$ tungsten spectra energies e arranged by columns, $3mm$, $6mm$, $12mm$ and $24mm$ collimations c (see Equation 3.2) displayed on each octant, and a $g = 600mm$ FOV (see Equation 3.1). The phantom signal is the sum of the Compton and Rayleigh contributions.

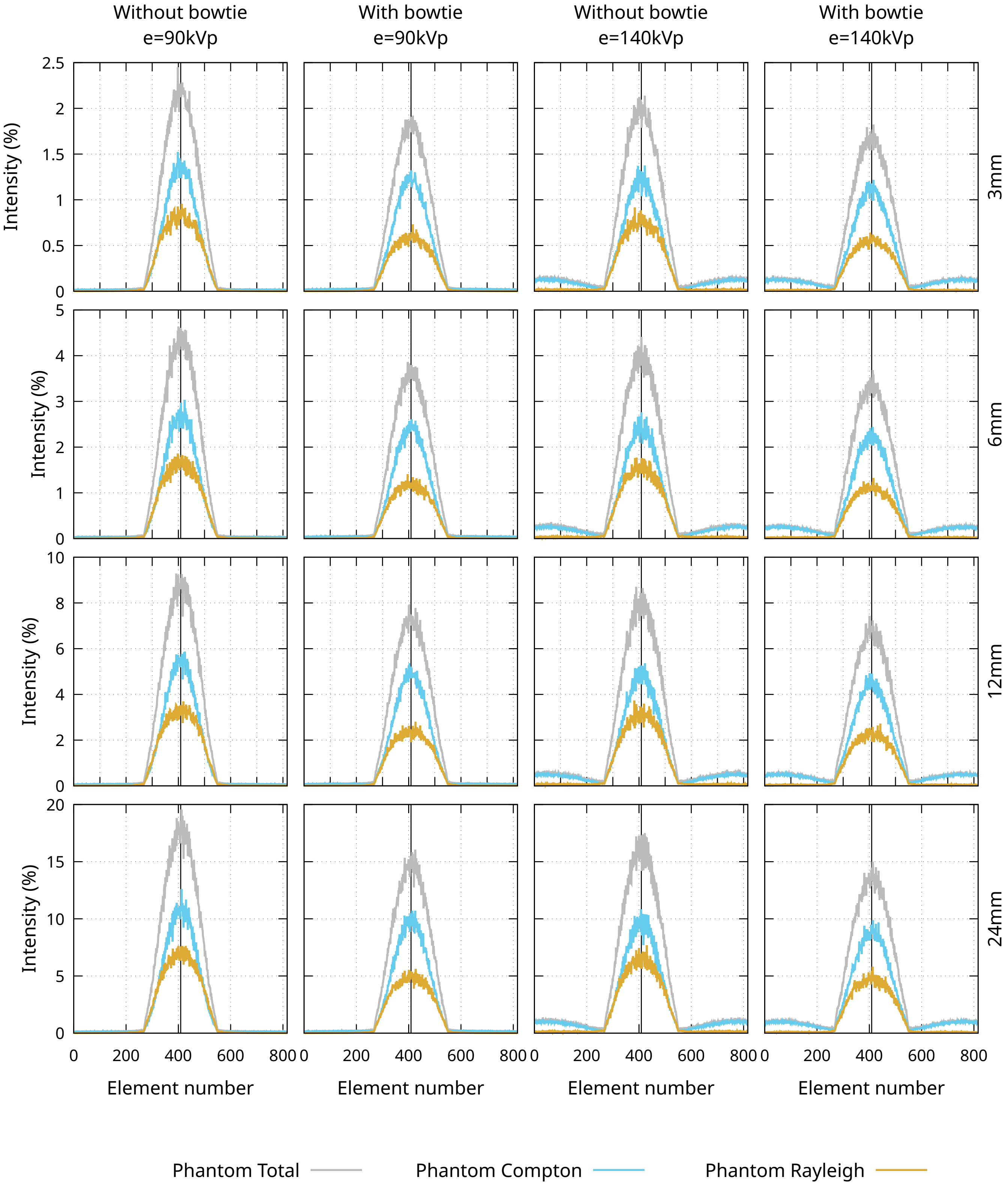

FIGURE B.1: The scatter-to-primary ratio of a 215.4mm diameter phantom without septa.

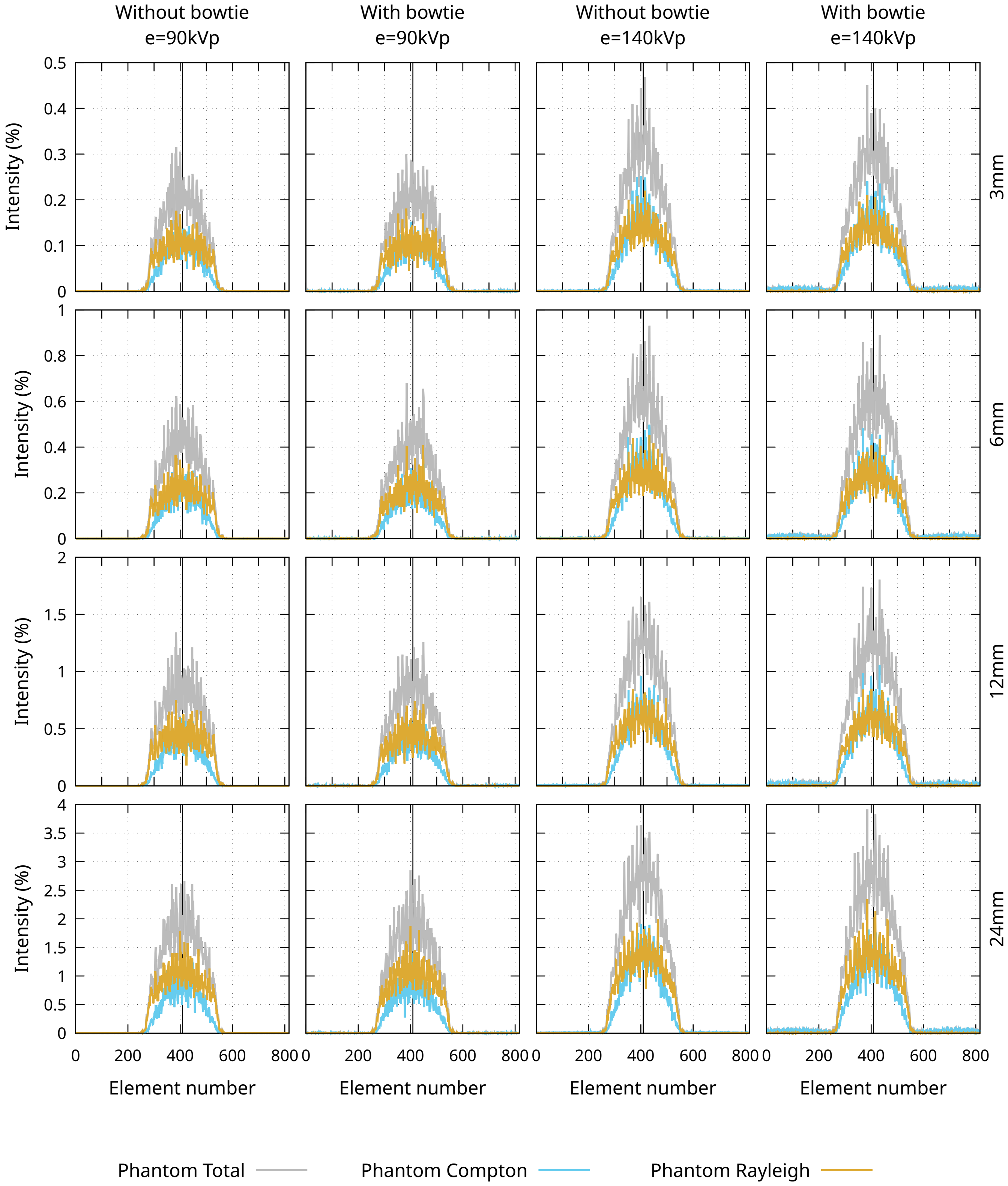

FIGURE B.2: The scatter-to-primary ratio of a 215.4mm diameter phantom with septa.

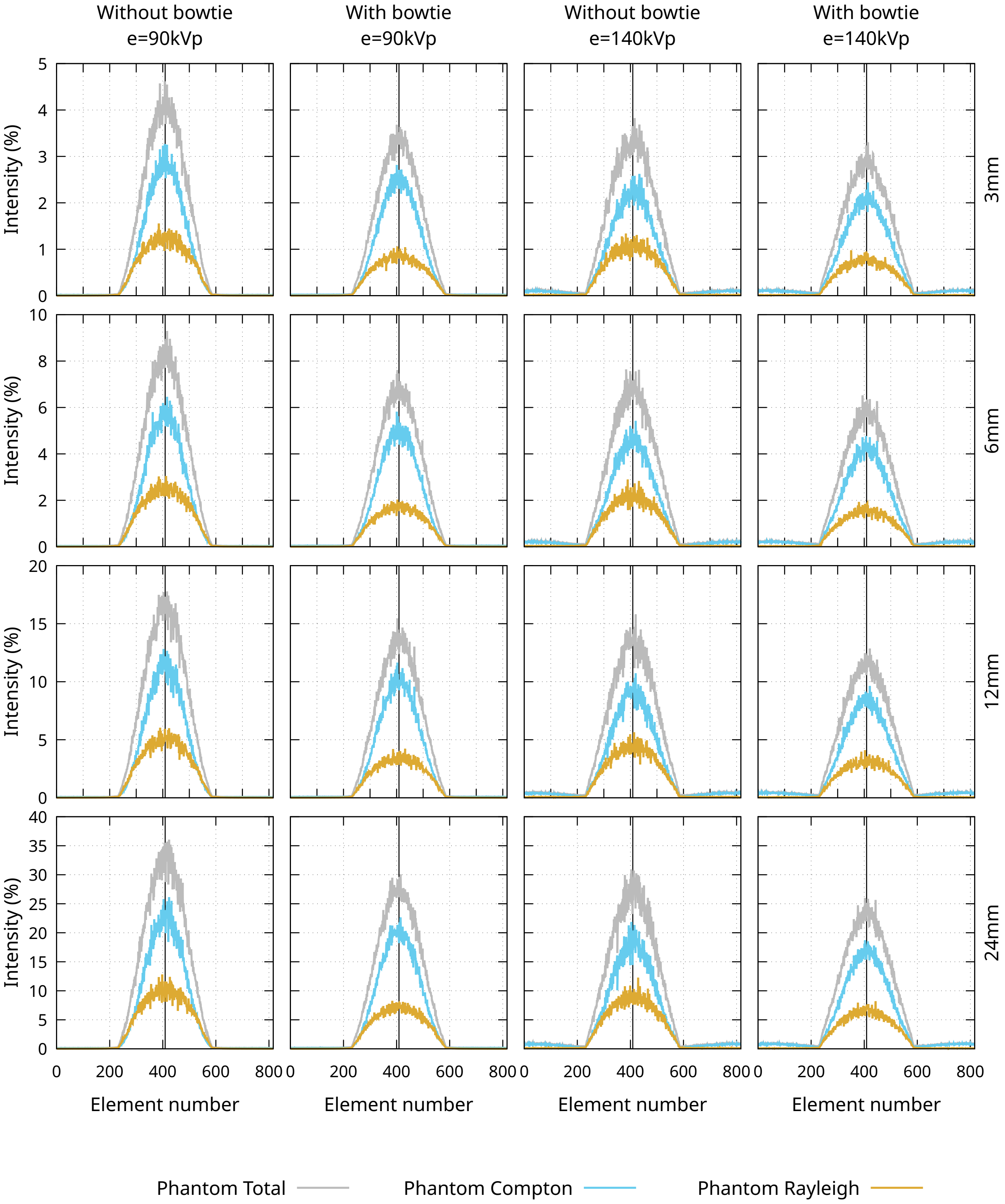

FIGURE B.3: The scatter-to-primary ratio of a 270mm diameter phantom without septa.

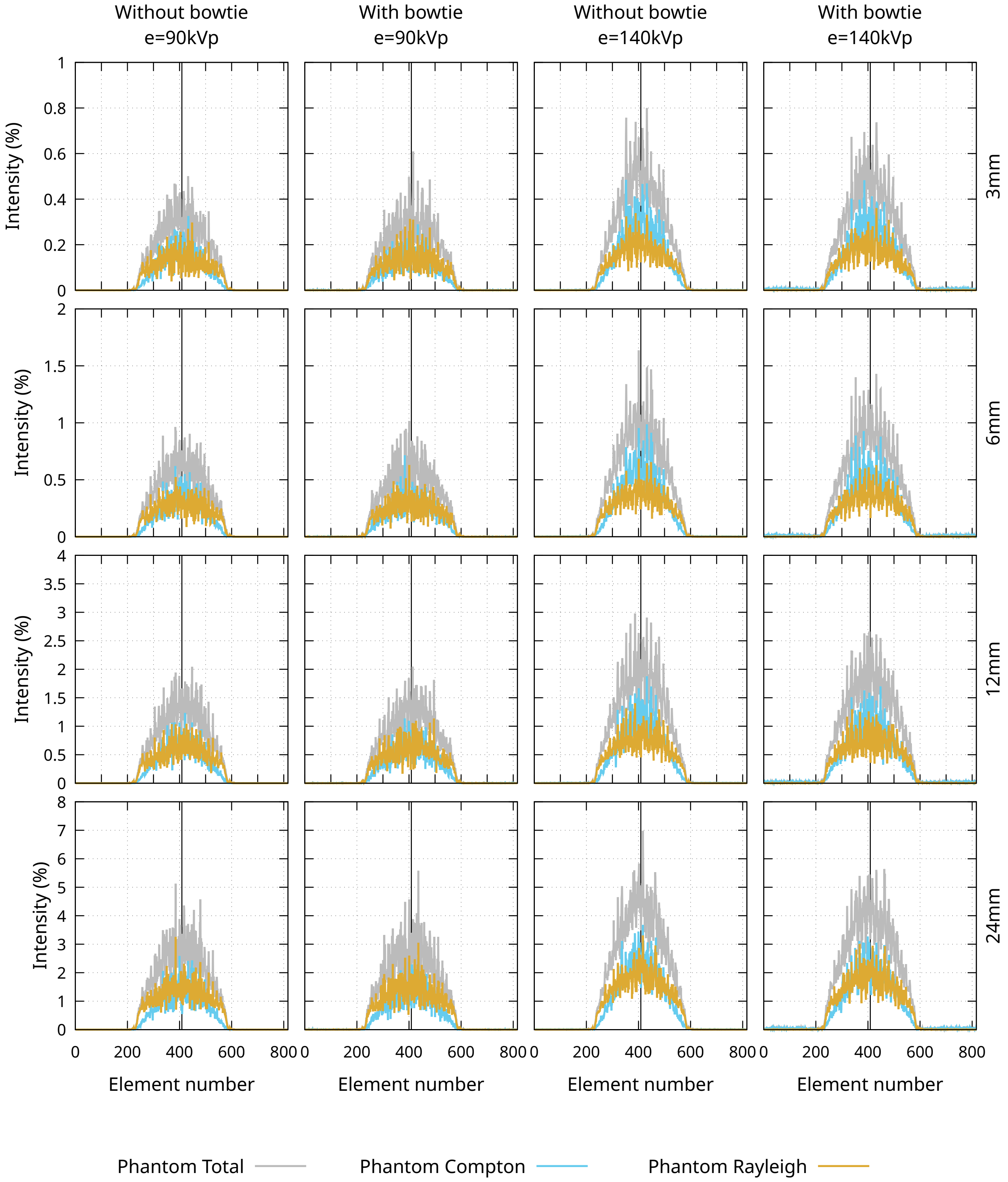

FIGURE B.4: The scatter-to-primary ratio of a 270mm diameter phantom with septa.

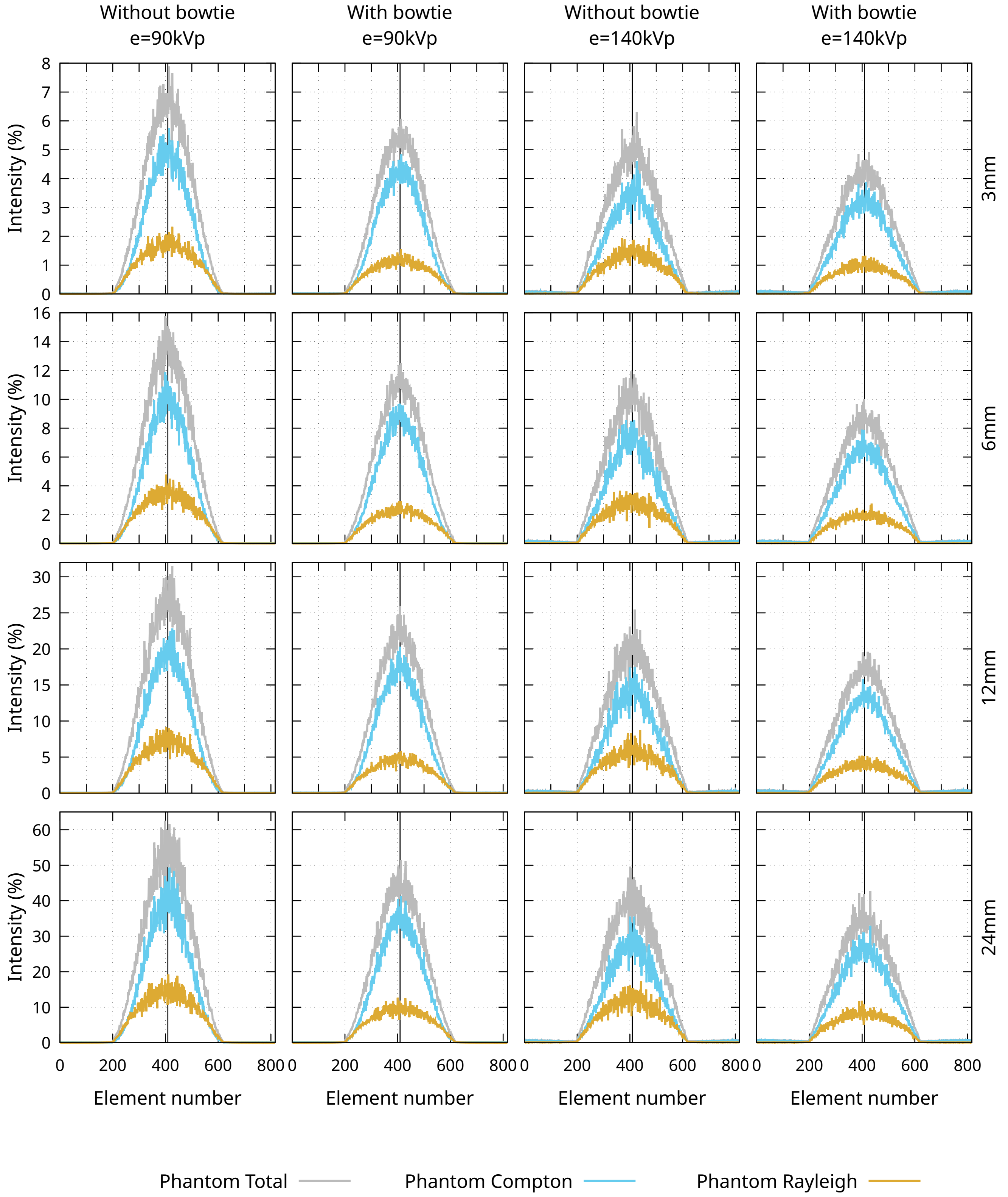

FIGURE B.5: The scatter-to-primary ratio of a 320mm diameter phantom without septa.

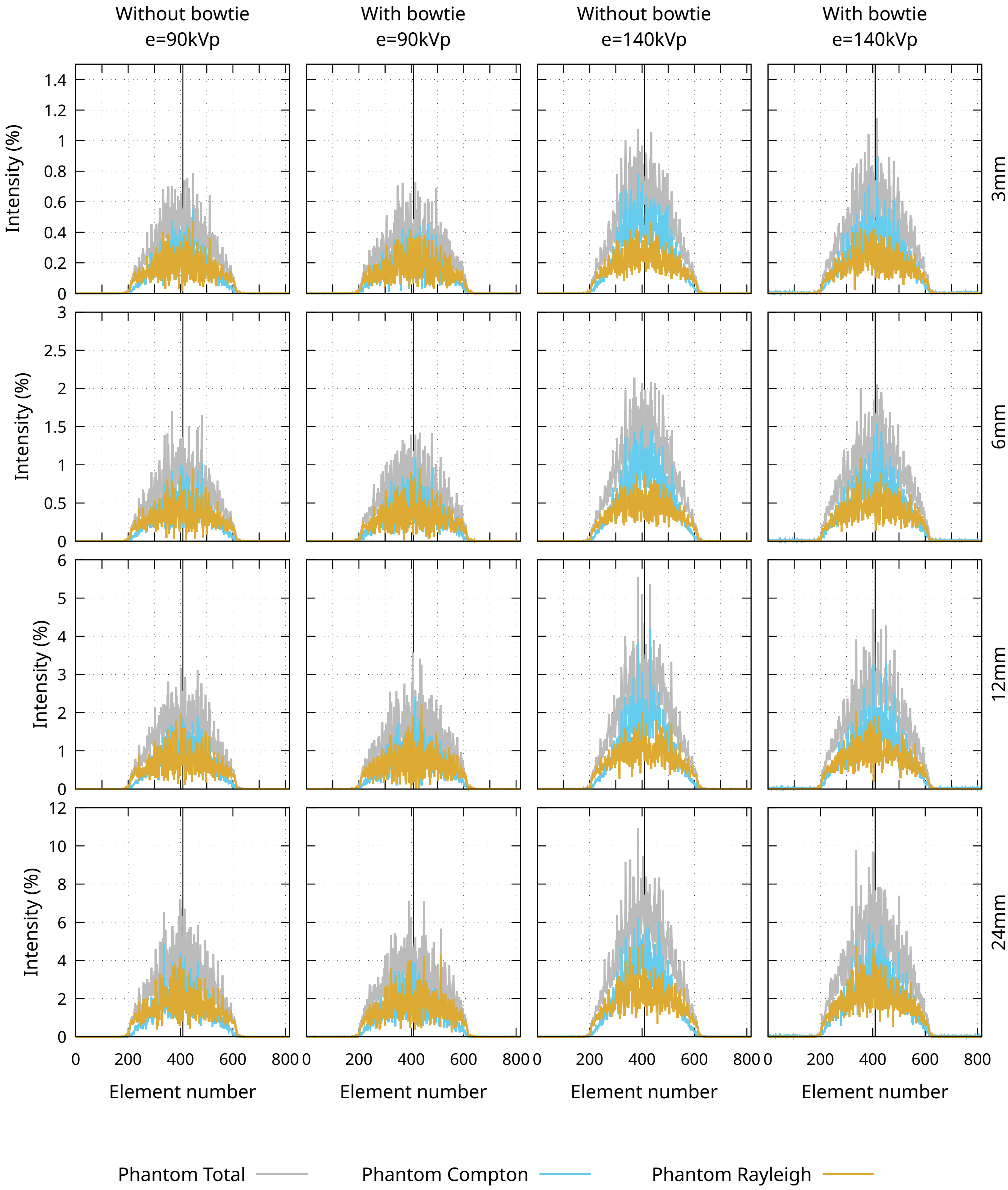

FIGURE B.6: The scatter-to-primary ratio of a 320mm diameter phantom with septa.

Bibliography

Agostinelli, S. et al. (July 2003). "GEANT4 - A simulation toolkit". In: *Nuclear Instruments and Methods in Physics Research, Section A: Accelerators, Spectrometers, Detectors and Associated Equipment* 506 (3), pp. 250–303. ISSN: 01689002. DOI: 10.1016/S0168-9002(03)01368-8.

Akbarzadeh, A. et al. (Mar. 2010). "Measurement of scattered radiation in a volumetric 64-slice CT scanner using three experimental techniques". In: *Physics in Medicine and Biology* 55 (8), pp. 2269–2280. ISSN: 00319155. DOI: 10.1088/0031-9155/55/8/010. URL: https://iopscience.iop.org/article/10.1088/0031-9155/55/8/010https://iopscience.iop.org/article/10.1088/0031-9155/55/8/010/meta.

Arroyo-Portilla, Daniel et al. (June 2021). "Variability of primary and scatter signal in dect: an exploratory study". In: *Revista de Ciencia y Tecnología* 37 (2), pp. 16–22. ISSN: 2215-5708. URL: https://revistas.ucr.ac.cr/index.php/cienciaytecnologia/article/view/55431.

Attix, F.H. (2004). *Introduction To Radiological Physics and Radiation Dosimetry*, p. 607. ISBN: 0-471-01 146-0.

Behling, Rolf and Florian Grüner (Jan. 2018). "Diagnostic X-ray sources—present and future". In: *Nuclear Instruments and Methods in Physics Research Section A: Accelerators, Spectrometers, Detectors and Associated Equipment* 878, pp. 50–57. ISSN: 0168-9002. DOI: 10.1016/J.NIMA.2017.05.034.

Berger, M.J. et al. (2010). "XCOM: Photon Cross Section Database (version 1.5)". In: DOI: 10.18434/T48G6X. URL: http://physics.nist.gov/xcom.

Bernstein, H. et al. (1983). "A detailed experimental and theoretical comparison of the angular and energy dependencies of grid transmission". In: *Medical physics* 10 (2), pp. 218–223. ISSN: 0094-2405. DOI: 10.1118/1.595239. URL: https://pubmed.ncbi.nlm.nih.gov/6865861/.

Chan, Tony F. and John Gregg Lewis (Sept. 1979). "Computing standard deviations". In: *Communications of the ACM* 22 (9), pp. 526–531. ISSN: 15577317. DOI: 10.1145/359146.359152. URL: https://dl.acm.org/doi/10.1145/359146.359152.

Chen, Yaqi et al. (Feb. 2016). "Line Integral Alternating Minimization Algorithm for Dual-Energy X-Ray CT Image Reconstruction". In: *IEEE transactions on medical imaging* 35 (2), pp. 685–698. ISSN: 1558-254X. DOI: 10.1109/TMI.2015.2490658. URL: https://pubmed.ncbi.nlm.nih.gov/26469126/.

Chen, Yu et al. (May 2007). "Comparison of Scatter/Primary Measurements with GATE Simulations for X-Ray Spectra in Cone Beam CT Mammography". In: pp. 3909–3914. DOI: `10.1109/NSSMIC.2006.353843`.

Darmian, A. Najafi et al. (2011). "Characterization of scattered radiation profile in volumetric 64 slice CT scanner: Monte Carlo study using GATE". In: *IEEE Nuclear Science Symposium Conference Record*, pp. 2692–2696. ISSN: 10957863. DOI: `10.1109/NSSMIC.2011.6152951`.

Engel, Klaus J. et al. (Mar. 2008). "Spectral analysis of scattered radiation in CT". In: *https://doi.org/10.1117/12.771063* 6913, pp. 605–615. ISSN: 16057422. DOI: `10.1117/12.771063`. URL: `https://www.spiedigitallibrary.org/conference-proceedings-of-spie/6913/69131R/Spectral-analysis-of-scattered-radiation-in-CT/10.1117/12.771063.fullhttps://www.spiedigitallibrary.org/conference-proceedings-of-spie/6913/69131R/Spectral-analysis-of-scattered-radiation-in-CT/10.1117/12.771063.short`.

Evans, Joshua D. et al. (Sept. 2013). "Experimental implementation of a polyenergetic statistical reconstruction algorithm for a commercial fan-beam CT scanner". In: *Physica Medica* 29 (5), pp. 500–512. ISSN: 1724191X. DOI: `10.1016/j.ejmp.2012.12.005`.

Flohr, Thomas (Mar. 2013). "CT Systems". In: *Current Radiology Reports* 1 (1), pp. 52–63. ISSN: 21674825. DOI: `10.1007/S40134-012-0005-5/FIGURES/14`. URL: `https://link.springer.com/article/10.1007/s40134-012-0005-5`.

Forghani, Reza, Bruno De Man, and Rajiv Gupta (Aug. 2017). "Dual-Energy Computed Tomography: Physical Principles, Approaches to Scanning, Usage, and Implementation: Part 2". In: *Neuroimaging Clinics of North America* 27 (3), pp. 385–400. ISSN: 15579867. DOI: `10.1016/j.nic.2017.03.003`. URL: `https://pubmed.ncbi.nlm.nih.gov/28711200/`.

Hubbell, John H. and Stephen M. Seltzer (2004). *X-Ray Mass Attenuation Coefficients*. DOI: `https://dx.doi.org/10.18434/T4D01F`. URL: `https://www.nist.gov/pml/x-ray-mass-attenuation-coefficients`.

Johns, P. C. and M. Yaffe (1982). "Scattered radiation in fan beam imaging systems". In: *Medical physics* 9 (2), pp. 231–239. ISSN: 0094-2405. DOI: `10.1118/1.595076`. URL: `https://pubmed.ncbi.nlm.nih.gov/7087909/`.

Joseph, Peter M. and Robin D. Spital (1982). "The effects of scatter in x-ray computed tomography". In: *Medical physics* 9 (4), pp. 464–472. ISSN: 0094-2405. DOI: `10.1118/1.595111`. URL: `https://pubmed.ncbi.nlm.nih.gov/7110075/`.

Kyriakou, Yiannis and Willi Kalender (Oct. 2007). "Efficiency of antiscatter grids for flat-detector CT". In: *Physics in medicine and biology* 52 (20), pp. 6275–6293. ISSN: 0031-9155. DOI: `10.1088/0031-9155/52/20/013`. URL: `https://pubmed.ncbi.nlm.nih.gov/17921585/`.

Lazos, Dimitrios and Jeffrey F. Williamson (Oct. 2010). "Monte Carlo evaluation of scatter mitigation strategies in cone-beam CT". In: *Medical Physics* 37 (10), pp. 5456–5470. ISSN: 2473-4209. DOI: 10.1118/1.3488978. URL: https://onlinelibrary.wiley.com/doi/full/10.1118/1.3488978https://onlinelibrary.wiley.com/doi/abs/10.1118/1.3488978https://aapm.onlinelibrary.wiley.com/doi/10.1118/1.3488978.

Leliveld, C. J. et al. (1994). "On the Significance of Scattered Radiation in Industrial X-ray Computerized Tomographic Imaging". In: *IEEE Transactions on Nuclear Science* 41 (1), pp. 290–294. ISSN: 15581578. DOI: 10.1109/23.281512.

Liu, Ruirui et al. (Feb. 2021). "Impact of bowtie filter and detector collimation on multislice CT scatter profiles: A simulation study". In: *Medical Physics* 48 (2), pp. 852–870. ISSN: 0094-2405. DOI: 10.1002/mp.14652. URL: https://onlinelibrary.wiley.com/doi/10.1002/mp.14652.

Mail, N. et al. (Jan. 2009). "The influence of bowtie filtration on cone-beam CT image quality". In: *Medical Physics* 36 (1), pp. 22–32. ISSN: 2473-4209. DOI: 10.1118/1.3017470. URL: https://onlinelibrary.wiley.com/doi/full/10.1118/1.3017470https://onlinelibrary.wiley.com/doi/abs/10.1118/1.3017470https://aapm.onlinelibrary.wiley.com/doi/10.1118/1.3017470.

Malusek, Alexandr, Michael Sandborg, and Gudrun Alm Carlsson (May 2008). "CTmod—A toolkit for Monte Carlo simulation of projections including scatter in computed tomography". In: *Computer Methods and Programs in Biomedicine* 90 (2), pp. 167–178. ISSN: 0169-2607. DOI: 10.1016/J.CMPB.2007.12.005.

Midgley, S. (Sept. 2006). "Angular width of a narrow beam for X-ray linear attenuation coefficient measurements". In: *Radiation Physics and Chemistry* 75 (9), pp. 945–953. ISSN: 0969-806X. DOI: 10.1016/J.RADPHYSCHEM.2006.01.008.

Morin, L. R.M. (1982). "Molecular Form Factors and Photon Coherent Scattering Cross Sections of Water". In: *Journal of Physical and Chemical Reference Data* 11 (4), pp. 1091–1098. ISSN: 15297845. DOI: 10.1063/1.555672.

Mott, J. H.L. and J. M. Daniel (July 2021). "Interactions of Electromagnetic Radiation and Subatomic Particles with Matter – Part 1". In: *Clinical Oncology* 33 (7), pp. 451–454. ISSN: 14332981. DOI: 10.1016/J.CLON.2021.02.004.

O'Sullivan, Joseph A. and Jasenka Benac (Mar. 2007). "Alternating minimization algorithms for transmission tomography". In: *IEEE Transactions on Medical Imaging* 26 (3), pp. 283–297. ISSN: 02780062. DOI: 10.1109/TMI.2006.886806.

O'Sullivan, Joseph A., Donald L. Snyder, and Bruce R. Whiting (2002). "Alternating minimization algorithms for transmission tomography using energy detectors". In: *Conference Record of the Asilomar Conference on Signals, Systems and Computers* 1, pp. 144–147. ISSN: 10586393. DOI: 10.1109/ACSSC.2002.1197165.

Division
Paternò, G. et al. (July 2018). "Geant4 implementation of inter-atomic interference effect in small-angle coherent X-ray scattering for materials of medical interest". In: *Physica Medica* 51, pp. 64–70. ISSN: 1724191X. DOI: `10.1016/j.ejmp.2018.04.395`.

Prakash, Prakhar and John M. Boudry (Mar. 2017). "Comparative study of bowtie and patient scatter in diagnostic CT". In: *https://doi.org/10.1117/12.2253012* 10132, pp. 627–634. ISSN: 16057422. DOI: `10.1117/12.2253012`. URL: `https://www.spiedigitallibrary.org/conference-proceedings-of-spie/10132/1/Comparative-study-of-bowtie-and-patient-scatter-in-diagnostic-CT/10.1117/12.2253012.short`.

Shefer, Efrat et al. (Mar. 2013). "State of the Art of CT Detectors and Sources: A Literature Review". In: *Current Radiology Reports* 1 (1), pp. 76–91. ISSN: 21674825. DOI: `10.1007/s40134-012-0006-4`. URL: `https://link.springer.com/article/10.1007/s40134-012-0006-4`.

Wadeson, Nicola, Edward Morton, and William Lionheart (Mar. 2010). "Scatter in an uncollimated x-ray CT machine based on a Geant4 Monte Carlo simulation". In: *https://doi.org/10.1117/12.843981* 7622, pp. 1090–1097. ISSN: 16057422. DOI: `10.1117/12.843981`. URL: `https://www.spiedigitallibrary.org/conference-proceedings-of-spie/7622/76223E/Scatter-in-an-uncollimated-x-ray-CT-machine-based-on/10.1117/12.843981.full`.

Willemink, Martin J. and Peter B. Noël (May 2019). "The evolution of image reconstruction for CT—from filtered back projection to artificial intelligence". In: *European Radiology* 29 (5), pp. 2185–2195. ISSN: 14321084. DOI: `10.1007/s00330-018-5810-7`. URL: `https://pubmed.ncbi.nlm.nih.gov/30377791/`.

Williamson, Jeffrey F. et al. (2002). "Prospects for quantitative computed tomography imaging in the presence of foreign metal bodies using statistical image reconstruction". In: *Medical physics* 29 (10), pp. 2404–2418. ISSN: 0094-2405. DOI: `10.1118/1.1509443`. URL: `https://pubmed.ncbi.nlm.nih.gov/12408315/`.